UNIVERSIDADE DE SÃO PAULO
INSTITUTO DE FÍSICA DE SÃO CARLOS

João Augusto Sobral da Silva

Investigating spin liquids via projected wavefunctions

São Carlos

2022

João Augusto Sobral da Silva

Investigating spin liquids via projected wavefunctions

Dissertation presented to the Graduate Program in Physics at Instituto de Física de São Carlos, Universidade de São Paulo, to obtain the degree of Master of Science.

Concentration area: Basic Physics

Advisor: Prof. Dr. Eric de Castro e Andrade

Corrected version
(Original version available on the Program Unit)

São Carlos
2022

I AUTHORIZE THE REPRODUCTION AND DISSEMINATION OF TOTAL OR PARTIAL COPIES OF THIS DOCUMENT, BY CONVENTIONAL OR ELECTRONIC MEDIA FOR STUDY OR RESEARCH PURPOSE, SINCE IT IS REFERENCED.

Silva, João Augusto Sobral da
Investigating spin liquids via projected wave functions / João Augusto Sobral da Silva; advisor Eric de Castro e Andrade - corrected version -- São Carlos 2022.
109 p.

Dissertation (Master's degree - Graduate Program in Theoretical and Experimental Physics) -- Instituto de Física de São Carlos, Universidade de São Paulo - Brasil , 2022.

1. Frustrated magnetism. 2. Quantum spin liquids. 3. Parton construction. 4. Gutzwiller projected wave functions. 5. Variational Monte Carlo. I. Andrade, Eric de Castro e, advisor. II. Title.

“The ability to reduce everything to simple fundamental laws does not imply the ability to start from those laws and reconstruct the universe.”

— Philip W. Anderson, More is Different (Science, 1972).

ACKNOWLEDGEMENTS

This work was financed by the Coordenação de Aperfeiçoamento de Pessoal de Nível Superior – Brasil (CAPES) – Finance Code 001, via Grant No. 88887.474253/2020-00. I am humbly grateful for this opportunity and to each individual of our society who propitiated similar and primordial mechanisms to scientific development.

Formal education is not a certified path to achieve wisdom in life. Notwithstanding, once you have the necessary support to follow it, a plethora of opportunities for self-discovery and edifying interactions with many inspiring minds can be found. I am deeply grateful to have the opportunity to continue developing what I believe to be one valid path, and this would not be possible without the efforts of many inspiring people that I have met, but most importantly, without the sacrifices made by my mother Simone. Consequently, this work and all of my efforts are and will always be an infinitesimal fraction of her unbelievable perseverance and braveness throughout this life. Additionally, in times upon which denialism and ignorance hinder even the possibility of human existence by normalizing abrupt and premeditated destruction of life potential, explicit gratefulness and empathy stand as a moral demonstration of character and as a necessary incentive for the exercise of living. Therefore, I would also like to acknowledge important people who were crucial to my well-being, and consequently, to this work.

- To my advisor Prof. Dr. Eric de Castro e Andrade for this unique opportunity, the instigating physical discussions throughout my master's about strongly correlated systems, for the solicitous comprehension in difficult times, and for the patient and detailed orientation in each step of this dissertation. This also extends to Eric's fantastic demonstration of character in many aspects, including his concern on the future of his students. This experience was fundamental to my professional and personal development.

- To Fabrizio Oliviero and Prof. Rodrigo Pereira for the opportunity to work and discuss on interesting aspects of their previous work regarding chiral spin liquids. To Prof. Eduardo Miranda and Prof. Natanael Costa for accepting our invitation to the thesis defence and for the valuable advices.

- To my undergraduate thesis advisor Prof. Dr. Clovis Achy Soares Maia, who although was not directly involved in this thesis, was responsible for encouraging me to pursue a career in physics, and for writing a significant amount of recommendation letters since my undergraduate studies. Our conversations about the current status of scientific research in physics led me towards condensed matter physics, and his unique way of thinking about physics is one of the most influential professional

aspects of my career. I also want to thank for equal and much important support from my undergraduate research advisor Prof. Dr. Alexandra Mocellin, who was also fundamental for this opportunity and many others.

- To my mother Simone, for its incredible example of resilience, love, and will of power. It is impossible to put into words how I'm grateful for your existence and love, and although I am still stubborn in many aspects, I hope to emanate a fraction of your braveness upon each interaction within this life. Also, to my beautiful sister Luana, my good friend Ricardo and my kind-hearted old man, João Neto. Your support is the foundation and guidance for all of my efforts.

- To Olga, for inspiring me daily and turning the world into pure music and poetry. All the individual and collective growth that we share in these almost five years together is the most valuable gift that life has provided me since I decided to study physics.

- To Olga's family, for all the kind support since our first encounters. Many of our conversations have shaped my understanding about work ethics, living a balanced and meaningful life, and what it means to be a scientist. Thank you for the "sandwich master's" at your house, for all the good laughs, foods, and wines. They were a fundamental part of the success of this work. You are all incredible people. A kind hug to you, Teo, Nina, Princess Leia and Bruce.

- To my second family Iozenita, José Batista, Gabriela, Cleyderman and Cleyverton for being decisive with my progression, providing me financial help, encouragement and support, shelter in troubled times, and for the many happy memories that I hold dear in my heart wherever I go.

- To Dr. Flavia Batistuta for always being a source of stability in my family, and for helping me to recover from difficult and challenging times during the pandemic. This also extends to my dear Denise, whom kindly helped me to understand my inner struggles for more than four years now.

- To Vitor Dantas, for being my role model as a theoretical physicist since my first studies as an undergraduate, for motivating me to pursue a career in condensed matter, and for our beautiful and instigating physical discussions. Your influence over my preparation is simply unmeasurable. Cheers, to here and our future collaborations! Also to Vitor's family, particularly Bené, for the incredible help when moving from BSB to São Carlos - I owe you many lettuce pizzas!

- To all my friends, for their support when facing Covid-19 with my parents in a troubled period: Eduardo, Lizandra, Pedro, Igor, Lettieri, Ranier, Tábata, Miguel, Valeriano, Mariana, Caio, Paulo, Lorena, Lud, Felipe, Vitor Machado and Estevão.

Thank you for all the support and leisure moments. I would also like to thank specifically Miguel, Igor and Pedro for motivating me in difficult times, and for our beautiful and growing friendship.

- To Prof. Luiz Agostinho Ferreira for the amazing lectures and discussions on the rich physics surrounding quantum field theory. To Rodrigo Abreu for some great "non-local" interactions about physics and life. To Prof. Francisco Alcaraz for the opportunity of being his teaching assistant for "Introduction to computational physics" and for the many interesting discussions.
- To Felipe Console and Estevão Chedieck for helping me settle in and showing me the beautiful campus of USP at São Carlos. I am also grateful to Pedro Monteiro Cônsoli for gladly helping me on setting the basics for this LaTeX dissertation, and for giving me valuable information which motivated the decision to study at IFSC.
- To all the administrative staff at IFSC-USP for making the bureaucratic process of a pandemic master's easier. A special thanks go to Ricardo Vital, Silvio César and Neusa.

ABSTRACT

SILVA, J.A.S. **Investigating spin liquids via projected wavefunctions**. 2022. 109p. Dissertation (Master of Science) - Instituto de Física de São Carlos, Universidade de São Paulo, São Carlos, 2022.

Spin liquids are exquisite states of matter which host fractionalized excitations of spin and show no long-range magnetic order even at zero temperature due to quantum fluctuations. They have been extensively studied using fractionalized representations of the spin degrees of freedom in the so-called parton construction in conjunction with the Gutzwiller projection. Using Mean Field Theories (MFT), this constraint can be imposed on average, and numerical techniques, such as the Variational Monte Carlo (VMC) are required to impose the condition exactly at each site. In this framework, the VMC is a powerful tool to indicate which MFT ansatz is favored energetically to represent the spin liquid state based on the variational principle and the specific spin fractionalized representation. We employed this approach to investigate a putative chiral spin liquid state in the Kagome lattice using the Abrikosov representation which can host spinons: neutral spin-1/2 fermionic quasiparticles. This work was performed in the $J_1 - J_d - J_\chi$ Kagome Lattice model, and it was inspired by experimental results from the material $\alpha - \mathrm{Cu_3Zn\,(OH)_6\,Cl_2}$ (kapellasite) - a polymorphous structure of $\mathrm{ZnCu_3(OH)_6Cl_2}$ (herbertsmithite) - with no long-range order down to $T = 20\text{mK}$. Our VMC results favor a gapless chiral spin liquid with staggered flux $\pm\pi/2$ over the triangles and 0 flux on the hexagons in the region with $J_d/|J_\chi| > 0$ for small $|J_1| < 0.1$. We also investigated the stability of this spin-liquid state to ordered phases known to occur in the model. In addition, new non-coplanar ordered phases were encountered via the gradient descent method in the limit of $S \gg 1$ which may be relevant for ordered Kagome materials. By representing the influence of the ordered phases via a fictitious Zeeman field in a spin density wave (SDW) ansatz for the VMC, we have found consistent results with our classical phase diagram, establishing a more realistic region for the spin liquid domain.

Keywords: Frustrated magnetism. Quantum spin liquids. Parton construction. Gutzwiller projected wave functions. Variational Monte Carlo.

RESUMO

SILVA, J.A.S. **Investigando líquidos de spin através de funções de onda projetadas**. 2022. 109p. Dissertação (Mestrado em Ciências) - Instituto de Física de São Carlos, Universidade de São Paulo, São Carlos, 2022.

Líquidos de spin são fases exóticas da matéria que abrigam excitações fracionalizadas de spin, além de não demonstrarem ordenamento magnético de longo alcance mesmo próximo à temperatura zero devido à flutuações quânticas. Essas fases têm sido extensivamente estudadas através de representações fracionalizadas dos graus de liberdade do spin através do formalismo chamado Construção de Partons em conjunção com a projeção de Gutzwiller. Através de Teorias de Campo Médio (MFT), essa condição física só pode ser imposta na média, de forma que técnicas numéricas como o Monte Carlo Variacional (VMC) são necessárias para a imposição do vínculo de forma exata em cada sítio. Nesse contexto, o VMC é uma poderosa ferramenta que permite indicar qual ansatz de campo médio é favorecido energeticamente para representar um estado de líquido de spin, através do princípio variacional junto da representação fracionalizada de spin adotada. Nós desenvolvemos essa tecnologia com o intuito de investigarmos um líquido de spin quiral particular na rede de Kagome utilizando férmions de Abrikosov, que contém os chamados spinons: quasipartículas fermiônicas neutras de spin 1/2. Esse trabalho foi realizado considerando-se o modelo $J_1 - J_d - J_\chi$ na rede de Kagome, e foi motivado por resultados experimentais no material $\alpha - \mathrm{Cu_3Zn\,(OH)_6\,Cl_2}$ (kapellasita) - uma estrutura polimórfica ao mineral $\mathrm{ZnCu_3(OH)_6Cl_2}$ (herbertsmithite) - sem ordenamento magnético de longo alcance até $T = 20\mathrm{mK}$. Nossos resultados de VMC indicam um favorecimento do líquido de spin quiral sem gap com fluxos alternados $\pm\pi/2$ sobre os triângulos e fluxo 0 nos hexágonos, ao longo da região com $J_d/\left|J_\chi\right| > 0$ para $|J_1| < 0.1$. Nós também investigamos a estabilidade desse líquido de spin com respeito a fases magnéticas ordenadas conhecidas na literatura, além de encontrarmos novas fases clássicas não coplanares que possam ser relevante para materiais de Kagome ordenados no limite em que $S \gg 1$. Por fim, representando a possível influência de ordenamento magnético com um campo de Zeeman fictício em um ansatz de onda de densidade de spin (SDW) para o VMC, demarcarmos a região no espaço de acoplamentos para o favorecimento do líquido de spin do ponto de vista de flutuações quânticas.

Palavras-chave: Magnetismo frustrado. Líquidos de spin quânticos. Construção de Partons. Funções de onda projetadas de Gutzwiller. Monte Carlo variacional.

LIST OF FIGURES

Figure 1 – (a) Neutron scattering intensity, $S\,(Q,E)$, on a logarithmic scale (colored region) as a function of wave vectors Q and energy E of kapellasite at a temperature of $T = 0.1K$. (b) Wave vector dependence of the inelastic magnetic scattering. 26

Figure 2 – (a) Spin susceptibility, local and uniform, as a function of temperature. The inset indicates a High-temperature series fit down to $20mK$. (b) Total specific heat per spin C_v measured in zero field and compared with the $J_1 - J_d$ model. 26

Figure 3 – (a) Relevant exchange couplings in the Kapellasite material between Zn (blue) and Cu (yellow) ions considered in the $J_1 - J_d - J_\chi$ Heisenberg model (1.1). (b) Representation of how the Kagome pattern arises in the material Kapellasite. The kagome layers are weakly coupled through Cl-OH hydrogen bonds. 27

Figure 4 – Representation of the Kagome lattice with 3 atoms per unit cell (blue parallelogram). The nearest neighbors are defined as $\delta_i = \frac{\mathbf{a}_i}{2}$ for $i = 1, 2, 3$. 32

Figure 5 – Spin spatial configuration of the cuboc-1 (a) and cuboc-2 (b) phases on the Kagome lattice alongside their correspondent SSSF. 36

Figure 6 – Spin spatial configuration of the AFM coplanar states $\boldsymbol{Q} = 0 \times 0$ (a) and $\boldsymbol{Q} = \sqrt{3} \times \sqrt{3}$ (b) on the Kagome Lattice.[1] 36

Figure 7 – Classical phase diagram for the $J_1 - J_2 - J_d$ - with $J_1 = -1$ (a) and $J_1 - J_2$ (b) Heisenberg models in the Kagome Lattice. Black dashed lines represent first order phase transition boundaries.[2,3] 37

Figure 8 – The SSSF for phases cuboc-2, cuboc-1, FM, $\boldsymbol{Q} = 0 \times 0$ and $\boldsymbol{Q} = 3 \times 3$ are presented, with the BZ (dashed gray lines) and extended BZ (solid black lines). The positions of highly symmetric momentum points Γ, K, M, $\mathrm{K_e}$, $\mathrm{M_e}$, are also presented. The color intensity for each profile is only schematic and, consequently, independent between different phases.[2,3] . 38

Figure 9 – Pictorial representation of the Gutzwiller projector (2.56) excluding states that do not obey the constraint in (2.21). 47

Figure 10 – Dependence of the zth component of spin-spin correlations with the distance between spins. The dashed black curves indicate the expected asymptotic value from equation (2.82). The red dots represent the data obtained for $N = 512$ in the VMC with a GPW ansatz. Errors bars are smaller than the markers. 53

Figure 11 – Monte Carlo evolution of the GSE observable for the GPW as a function of MC steps for different system sizes. The data was obtained by an average of 50 different experiments (random seeds) for each system size. The MC Steps necessary for the convergence of the observable is understood as a thermalization time. 54

Figure 12 – Electronic band structure for the Kagome Lattice with and negative hopping parameters t (a). The Fermi energy level $E_f = 0$ is indicated with the green dashed lines. The corresponding path along high-symmetry lines of the BZ is also presented (b). 56

Figure 13 – Six-site unit-cell configuration for the $\pi-$Flux ansatz for the Heisenberg model on the Kagome lattice. The π flux is imposed on the elementary hexagons and the 0 Flux on triangles. The solid black lines represent $\chi_{ij} = -1$ and the gray lines $\chi_{ij} = 1$. From the doubled unit cell (blue parallelogram) $\mathbf{a}_1 \to 2\mathbf{a}_1$. 57

Figure 14 – Electronic band structure for the U(1)-Dirac state for $J\chi > 0$, $k_x = 0$ and $k_y \in [0, 6]$ in a $N = 50 \times 50 \times 3$ Kagome lattice. The intersection points with the Fermi energy $E_F/J\chi = \sqrt{3} - 1$ are given by $\mathbf{k}_1 = \left(0, \frac{\pi}{\sqrt{3}}\right)$ and $\mathbf{k}_2 = \left(0, \pi\sqrt{3}\right)$. The flat band is doubly degenerate while the remaining four are nondegenerate. 59

Figure 15 – Pictorial representation of gauge fluxes passing through the triangles to reproduce the Ansätze SL-$\left[\frac{\pi}{2}, 0\right]$ and SL-$\left[\pm\frac{\pi}{2}, 0\right]$, respectively.[4,5] (a) For the uniform chiral ansatz SL-$\left[\frac{\pi}{2}, 0\right]$, it is necessary to consider a doubled unit cell. This is done by imposing $\chi_{ij} = (+) - i$ for bonds on (anti)clockwise direction. The signals inside the hexagons illustrate that the overall flux is zero. One can interpret the dashed bonds as defect antiflux tubes passing through the triangles, maintaining the chiral phase invariant while canceling the background flux on the hexagons.[6] (b) The staggered chiral ansatz SL-$\left[\pm\frac{\pi}{2}, 0\right]$ can be implemented by imposing the same convention for χ_{ij}. The arrow directions provide the hopping orientation. 61

Figure 16 – Classical phase diagram for the $J_1 - J_d - J_\chi$ Heisenberg model on the Kagome lattice with $J_\chi = 1.0$ setting the energy scale. We have five classical ordered states: cuboc-2, AFMd, FM , FM-stripe, and FMd. Black dashed lines indicate first-order phase transitions. The solid line between the cuboc-2 and the AFMd phases indicates a continuous transition. A classically disordered region, in red, is present around the point $J_1 = J_d = 0$. Vertical gray lines are related to the minimization examples in Fig. 18. 65

Figure 17 – Classical spin representation for the regime $J_d \gg J_\chi$ in the $J_1 - J_d - J_\chi$ Kagome Lattice model of weakly coupled chains, with the correspondent spin structure factors. In this scenario, AFM (FM) spin chains which are weakly coupled for $J_d > 0$ ($J_d < 0$), can be seen along the diagonal dashed red lines on the hexagons of the Kagome lattice (a) [(b)]. 66

Figure 18 – Energy comparison between FMd, AFMd, FM-stripe, FM, cuboc-2 phases and the result of numerical minimization via the GD method along the values (a) $J_1 = -0.16$, (b) $J_1 = -0.04$ and $J_1 = -0.26$ (c). In the second case, the minimum energy near $J_d/J_\chi \approx 0$ is not equivalent to any ordered phase, and the correspondent SSSF is characterized by a blurred profile. Same color code as used in Fig. 16. 67

Figure 19 – Classically disordered region spin configuration in real space and correspondent SSSF. The state is only one of the many possible states inside the disordered region. 68

Figure 20 – Classical spin configurations (left column) and corresponding SSSF (right column) for the phases in Fig. 16 with $J_\chi = 1.0$. The magnetic unit cell is shown in blue. (a) cuboc-2; (b) AFMd ($J_1 = -0.05$, $J_d = 0.3$); (c) FM; (d) FM-stripe ($J_1 = -0.13$, $J_d = -0.16$); (e) FMd ($J_1 = 0$, $J_d = -0.3$). The color scale on the right is arbitrary. The FM-stripe phase is stabilized in one of three equivalent configurations distinguished by a $2\pi/3$ rotation. 69

Figure 21 – Order parameter squared (normalized with respect to its value in the cuboc-2 state) as a function of J_1, indicating the continuous transition between the cuboc-2 and AFMd phases for $J_\chi = 1$. The red (light-blue) curve shows the normalized Bragg peak intensity at the cuboc-2(1) ordering wave vectors. At the point $J_1 = 0$ an octahedral phase maximizing the staggered chirality emerges. The phase transition to the cuboc-1 is slower and takes place in the vicinity of $J_1 = 1.0$ (not shown). 70

Figure 22 – The spin directions on the magnetic unit cell (a) for the cuboc-2 (b) ($J_1 = -0.4$), octahedral ($J_1 = 0$) (c) and cuboc-1 ($J_1 = 1.0$) (d). An animated gif of the continuous phase transition between cuboc-2 and cuboc-1 phases seen from the perspective of the spins in the magnetic unit cell can be seen in this link. 70

Figure 23 – Order parameter squared (normalized with respect to its value in the FM state) as a function of J_1, indicating the phase transition between the FM, FM-stripe and FMd phases for $J_\chi = 1$ and $J_d = -0.20$ (a), and $J_d = -0.15$ (b). The red (light-blue) [dark] curve shows the normalized Bragg peak intensity at the FMd(FM, $\mathbf{\Gamma}$ momentum point) [FM-stripe] ordering wave vectors. The dashed lines indicate the boundary of phases from Fig. 16. In the second case (b), the FMd phase is close to the disordered region and does not develop pronounced Bragg peaks. . . . 71

Figure 24 – Physical Ansätze describing the CSL with 0 gauge flux over the hexagons and staggered $\pm\pi/2$ flux on the elementary triangles. Cases I, II and III are indicated at subfigures (a) with oriented χ_d (b), and non-oriented $\chi_d \in \mathbb{R}$ (c). Interactions between different sublattices are always oriented with $\chi_1 \in \mathbb{C}$. 74

Figure 25 – Energy spectrum representation for $\kappa_d/\kappa_1 = 1.2$ (left). This form is representative for $0 < \kappa_d < 2\kappa_1$. The density plot of the dispersion for the lower (center) and upper bands (right) is also presented. In the latter, dashed lines indicate the spinon Fermi surface for the middle band (along the $\mathbf{\Gamma} - \boldsymbol{M}$ points in the BZ). 74

Figure 26 – Energy dispersion for the lower and upper bands, along the Γ-K direction, for different values of the ratio κ_d/κ_1. 75

Figure 27 – VMC energy expectation value for the chiral (green), Heisenberg J_1 (black) and J_d (purple) contributions for (a) Case I $(\kappa_d/\kappa_1 < 0)$, II $(\kappa_d/\kappa_1 > 0)$ and (b) III $(\kappa_d/\kappa_1 \in \mathbb{R})$. The orange line is the result for the AFM S=1/2 chain via Bethe's ansatz. These energies were obtained for $L = 12$; Error bars are smaller than the markers. Gray vertical dashed lines indicate the region of stability for Cases I and II established from the MFT analysis. 76

Figure 28 – Ground state energy obtained via VMC for Cases I-III as a function of J_d/J_χ with $J_1 = 0$. Classical energies for phases Cuboc-2, AFMd, FMd and FM are displayed for comparison. 77

Figure 29 – Finite-size scaling for the magnetization with $J_1 = -0.01$ and $J_\chi = 1.0$ as a function of $1/L$. The inset graphic displays the phase transition between the AFMd and the CSL from the perspective of the magnetization in the thermodynamic limit as a function of J_d. The colored region indicates the numerical uncertainty in the phase transition. 78

Figure 30 – Energy as a function of the Zeeman coupling h for different values of J_d. Both the transition from the CSL to the FMd (a), at $J_1 = -0.02$, and to the AFMd (b), at $J_1 = -0.01$, are presented. The magnetization plateaus in the second case are illustrative to the difficulty of selecting the phase transition boundary precisely. Error bars are smaller than the markers, and the shaded region in the inset indicates the numerical uncertainty in the phase transition. 79

Figure 31 – Quantum phase diagram for the $J_1 - J_d - J_\chi$ Kagome Lattice model with S=1/2. The phase transitions were obtained from the VMC comparison with an SDW ansatz. The error bars indicate the numerical limitation of our VMC, which consists on a estimate of the plateaus of magnetization. Same color code used in Figure 16. The FM-stripe phase is indicated in orange. 80

Figure 32 – Virtual exchanges for the clockwise (a) and counterclockwise permutations (b) in the specific spin configuration 001. The final contribution, given by the sum of each term in equation (D.12), can be seen in Table 5. The colors of the spins are arbitrary and serve only to guide the eye. 109

LIST OF TABLES

Table 1 – Some examples of quantum spin liquids with their respective mean field theories, and possible low energy physics and excitations. For more examples see SAVARY *et al*[7] and ZHOU *et al.*[8] 43

Table 2 – Ground state energy for the S=1/2 AFM spin chain using the GPW. The ground state energy was calculated for both non local + local energy terms (NL) and only local terms (L) by exploiting the SU(2) invariance of the model. The data was obtained with $2,0 \times 10^4$ MC sweeps discarded for thermalization, and $1,0 \times 10^5$ MC sweeps for average, divided into 100 bins. Numbers in parenthesis indicate the standard deviation with respect to the last digit. 54

Table 3 – Ground state energy for the Heisenberg AFM model in a Kagome lattice using the GPW for the 0 (a) and π (b) flux Ansätze using PBC. The results for MBC were also consistent with the expected result. The data was obtained with $2,0 \times 10^5$ MC sweeps discarded for thermalization, and $1,0 \times 10^5$ MC sweeps for average, divided into 100 bins. 60

Table 4 – GSE for a GPW representing the chiral spin liquid candidates $SL - \left[\pm\frac{\pi}{2}, 0\right]$ (a) $SL - \left[\frac{\pi}{2}, 0\right]$ (b) using MBC. The data was obtained with $2,0 \times 10^5$ MC sweeps discarded for thermalization, and $2,0 \times 10^5$ MC sweeps for average, divided into 100 bins. 60

Table 5 – Correspondence between the spin configuration and possible virtual exchanges for the chiral interaction (diagrams and analytical form). Labels are related with the spin in our VMC: 0 for ↓ and 1 for ↑. 62

Table 6 – Chirality energy contribution for different lattice sizes, within the GPW representation for the spin liquid candidate $SL - \left[\frac{\pi}{2}, 0\right]$ with uniform $\pi/2$ flux through the triangles and zero background flux on the hexagons. The energy was obtained with $2,0 \times 10^5$ MC sweeps discarded for thermalization, and $2,0 \times 10^5$ MC sweeps for average, divided into 100 bins. 63

Table 7 – Ground state energy for the Haldane-Shastry model using the GPW for different numbers of spins N. The second column represents the exact values from equation (B.2), whereas the third column contains the results obtained within the VMC. 99

LIST OF ABBREVIATIONS AND ACRONYMS

AF	Antiferromagnetic
BZ	Brillouin zone
DMRG	Density matrix renormalization group
FM	Ferromagnetic
VMC	Variational Monte Carlo
QSL	Quantum spin liquid
CSL	Chiral spin liquid
SSSF	Static Spin Structure Factor
GD	Gradient Descent
MC	Monte Carlo
GSE	Ground State Energy
OBC	Open boundary conditions
APBC	Anti-periodic boundary conditions
PBC	Periodic boundary conditions
MBC	Mixed boundary conditions
INS	Inelastic neutron scattering
RIXS	Resonant inelastic x-ray scattering
RVB	Resonating Valence Bond
SDW	Spin density wave

CONTENTS

1 INTRODUCTION . . . 25

2 NUMERICAL AND THEORETICAL METHODOLOGY . . . 31
2.1 Gradient descent and classical phases on the Kagome lattice . . . 31
2.1.1 Static Spin Structure Factor . . . 31
2.1.2 Gradient Descent method . . . 34
2.1.3 Classical Benchmarks: From Néel AFM to noncoplanar phases . . . 35
2.2 Parton Construction and Variational Monte Carlo . . . 37
2.2.1 Fermionic Abrikosov Representation . . . 39
2.2.2 Beyond MFT and Gauge Invariance . . . 43
2.2.3 Metropolis-Hastings Algorithm and Quantum Variational Principle . . . 44
2.2.4 Gutzwiller Projected Wave Functions and Slater Determinant Ansätze . . . 47
2.2.5 SDW wave functions and ordered phases . . . 50
2.3 Numerical Benchmarks for AFM S=1/2 Heisenberg models . . . 52
2.3.0.1 Spin Chain . . . 52
2.3.0.2 Kagome Lattice . . . 55

3 NONCOPLANAR MAGNETIC ORDERS IN THE KAGOME LATTICE 65
3.1 Classical Phase Diagram for the $J_1 - J_d - J_\chi$ Heisenberg model . . . 65
3.2 Discussions . . . 71

4 GAPLESS CHIRAL SPIN LIQUID IN THE KAGOME LATTICE . . 73
4.1 Parton Mean Field Theory . . . 73
4.2 VMC results . . . 75
4.3 Quantum Phase Diagram for the $J_1 - J_d - J_\chi$ Heisenberg model . . 77

5 CONCLUSIONS AND OUTLOOK . . . 81

REFERENCES . . . 83

APPENDIX 95

APPENDIX A – VMC APPENDIX . . . 97
A.1 Matrix Determinant Lemma . . . 97
A.2 Shermann-Morrison Formula . . . 97

APPENDIX B – HALDANE-SHASTRY MODEL . . . 99

APPENDIX C – FERMIONIC MAJORANA REPRESENTATION . 101

APPENDIX D – CHIRAL INTERACTION 107

1 INTRODUCTION

Quantum Spin Liquids (QSL) have been extensively studied since their first conception in 1973 by Philip Anderson in the context of resonating valence bond (RVB) states.[9] These states cannot be described within Landau's classical theory of phases transitions based on symmetry breaking and conventional order parameters.[10] Instead, they are described by a topological order, which is highly related to the ground-state degeneracy and fractional excitations.[11] Quantum fluctuations destroy any long-range magnetic ordering near $T \approx 0K$ in these phases of matter. Additionally, they host unusual fractionalized excitations and present a long-range entanglement between spins. Broadly speaking, QSLs can be divided into gapped, with topological ground state degeneracy and anyonic excitations, and gapless, which are usually described by emergent fermions coupled to gauge fields.[12,13]

These novel phases can be found in lattices prone to geometrical frustration.[14] Specifically, we consider localized spins S=1/2 described by Heisenberg-like models in the context of Mott insulators. These localized spins become frustrated due to unsatisfied exchange interactions. Many experimental results have indicated the characteristic signatures for the apparition of QSLs in certain materials.[7,8] The most paradigmatic example can be found in the Kagome lattice with the mineral Herbertsmithite ($\mathrm{ZnCu_3\,(OH)_6\,Cl_2}$), which is believed to host a gapless U(1) QSL,[4,15,16] described by a Heisenberg model with nearest-neighbor antiferromagnetic (AFM) interactions only. Additionally, the Kapellasite mineral $\alpha - \mathrm{Cu_3Zn\,(OH)_6\,Cl_2}$,[3,17] a polymorphous structure of Herbertsmithite, is another emblematic example. Several experimental results indicate a rich physics describing this material. A continuum of excitations is present on the momentum structure from inelastic neutron scattering (INS) measurements, in contrast with the conventional magnons expected in ordered AFMs [Fig. 1(a)]. This is a signature of spinons, which are elementary spin excitations in QSLs.[15] Additionally, there's a divergence of the local susceptibility for $T \to 0$ as measured by Nuclear Magnetic Resonance (NMR) measurements [Fig. 2 (a)], following a Curie law of $\chi \propto 1/T$. High temperature series expansion to the experimental data of the total specific heat and susceptibility are in good agreement with a $J_1 - J_d$ (Fig. 3) Heisenberg model with $J_1 < 0$ and $J_d > 0$ (Fig. 2). Finally, the static spin structure factor (SSSF) exhibits short-range AFM correlations consistent with the cuboc-2[18] ordered phase [Fig. 1(b)] with a sharp peak located at $Q = 0.5$ Å^{-1}. These results motivated theoretical descriptions based on modified Heisenberg models which favor a gapless QSL close to the cuboc-2 ordered phase.

These experimental investigations are challenging since the presence of impurities or defects in the samples can lead to significant effects which may hinder the study

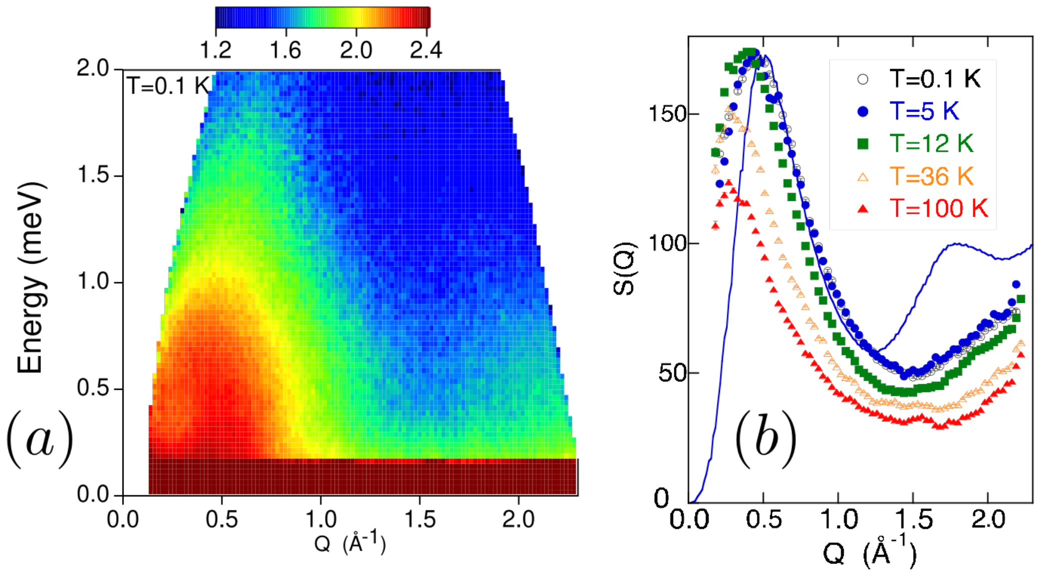

Figure 1 – (a) Neutron scattering intensity, $S(Q, E)$, on a logarithmic scale (colored region) as a function of wave vectors Q and energy E of kapellasite at a temperature of $T = 0.1K$. (b) Wave vector dependence of the inelastic magnetic scattering.
Source: Adapted from FÅK *et al.*[3]

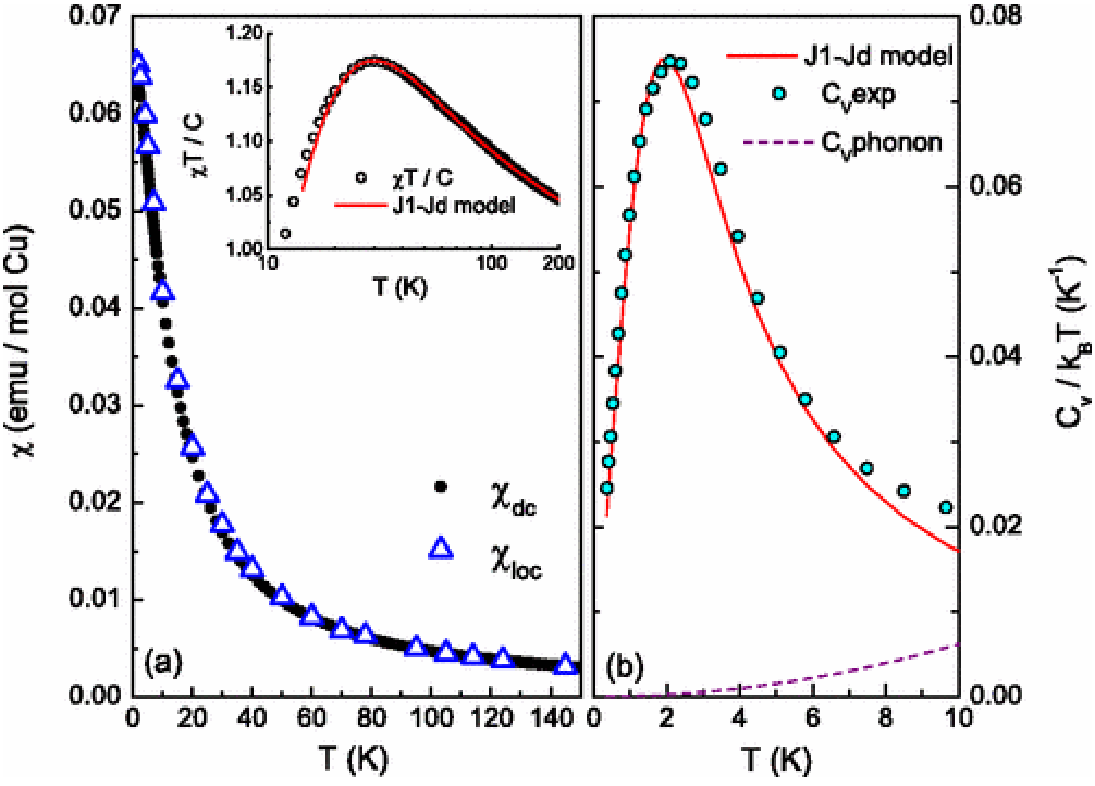

Figure 2 – (a) Spin susceptibility, local and uniform, as a function of temperature. The inset indicates a High-temperature series fit down to $20mK$. (b) Total specific heat per spin C_v measured in zero field and compared with the $J_1 - J_d$ model.
Source: FÅK *et al.*[3]

of the true ground state of materials.[19] It was only recently that in a programmable quantum simulator, a QSL was directly engineered in a controllable environment.[20,21] The implications of these recent studies furnish the possibility of studying more properties of these exotic phases of matter, as well as aspects involving topological qubits, which are expected to be resistant to noise and external interference and, consequently, relevant in the context of fault-tolerant quantum computing.[22]

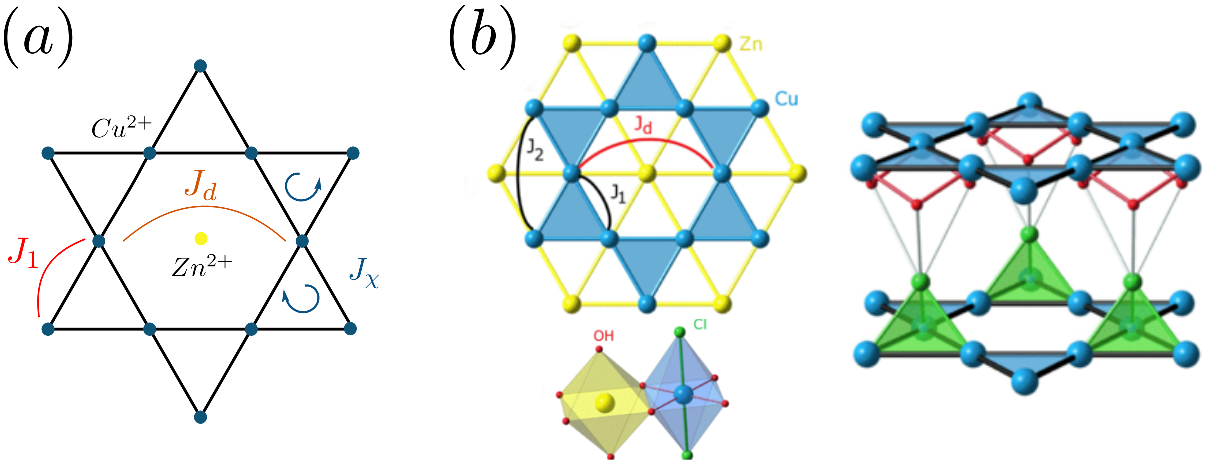

Figure 3 – (a) Relevant exchange couplings in the Kapellasite material between Zn (blue) and Cu (yellow) ions considered in the $J_1 - J_d - J_\chi$ Heisenberg model (1.1). (b) Representation of how the Kagome pattern arises in the material Kapellasite. The kagome layers are weakly coupled through Cl-OH hydrogen bonds.
Source: (a) By the author. (b) KERMARREC *et al.*[17]

In this rich context, it becomes clear the necessity of understanding QSLs fundamentally. One particular interest resides on QSLs with broken time-reversal symmetry, dubbed as chiral spin liquids (CSL).[23–25] One of the most prominent examples is the Kalmeyer-Laughlin state,[26] which can be described by mapping the bosonic spin excitations to fermions coupled to a Chern-Simons gauge field.[27,28] The result is a gapped topological phase with anyonic excitations. The Kalmeyer-Laughlin state can be stabilized as the ground state of spin-1/2 models containing chiral three-spin interactions that drive a uniform scalar spin chirality.[29–34] Physically, the three-spin interactions arise in Mott insulators with a magnetic flux through triangular plaquettes, and their ratio to exchange interactions can be enhanced in the vicinity of the Mott transition.[27,35] Moreover, the regime of strong three-spin interactions could be reached by Floquet engineering with circularly polarized light,[36–38] or artificially building lattices using Majorana-Cooper pair boxes.[39]

Contrastingly, three-spin interactions that induce staggered scalar spin chirality on the kagome lattice favor gapless spin liquids with spinon Fermi surfaces.[?,41,42] Unlike the Kalmeyer-Laughlin state, such gapless CSLs do not harbor anyons, but they represent striking examples of non-Fermi liquids with fractionalized excitations.[42] The standard analytical approach to these phases resorts to fermionic partons with a mean-field approximation for the U(1) gauge field. While spinon Fermi surface states have been argued to be stable against gauge fluctuations in two spatial dimensions,[43] the subject is still under debate.[7] In the case of chiral spin liquids, the lack of time-reversal symmetry provides additional protection against density-wave and pairing instabilities.[44,45] In particular, the stability of the gapless chiral spin liquid with staggered spin chiralities on the kagome lattice can be rationalized in terms of the absence of backscattering in a picture of chiral one-dimensional modes.[41,42]

CSLs can also arise from spontaneous breaking of time-reversal symmetry, as observed numerically in extended Heisenberg models[46–50] and also in the triangular lattice Hubbard model.[51] As previously explained, a gapless CSL was proposed for the material Kapellasite,[3,17,52] described by an extended Heisenberg model in which the dominant antiferromagnetic exchange coupling J_d is present across the hexagons of the kagome lattice. The established model for Kapellasite also includes nearest- and next-nearest-neighbor ferromagnetic couplings J_1 and J_2.[53] The phase diagram[3,19,52] contains non-coplanar ordered states known as cuboc-1 and cuboc-2,[2,18] and a CSL might be expected to arise from the quantum melting of the magnetic order while preserving a chirality pattern that breaks reflection and time-reversal symmetries. However, density-matrix renormalization group (DMRG) simulations suggest that the intermediate phase between cuboc-1 and cuboc-2 phases in the $J_1 - J_2 - J_d$ model is a valence bond crystal rather than a CSL.[54]

In this dissertation, we study the general description of QSLs based on parton constructions in conjunction with Gutzwiller projected wave functions (GPW) within a Variational Monte Carlo (VMC). As a particular case of study we consider the localized spins $S = 1/2$ at the sites i, j of the Kagome lattice which interacts via exchange J_{ij} in the Heisenberg Model

$$\begin{aligned} H = J_1 \sum_{\langle i,j\rangle} \mathbf{S}\left(\mathbf{r}_i\right) \cdot \mathbf{S}\left(\mathbf{r}_j\right) + J_d \sum_{ij\in\hexagon} \mathbf{S}\left(\mathbf{r}_i\right) \cdot \mathbf{S}\left(\mathbf{r}_j\right) + \\ + J_\chi \sum_{ijk\in\triangle} \mathbf{S}\left(\mathbf{r}_i\right) \cdot \left[\mathbf{S}\left(\mathbf{r}_j\right) \times \mathbf{S}\left(\mathbf{r}_k\right)\right] - J_\chi \sum_{ijk\in\triangledown} \mathbf{S}\left(\mathbf{r}_i\right) \cdot \left[\mathbf{S}\left(\mathbf{r}_j\right) \times \mathbf{S}\left(\mathbf{r}_k\right)\right], \end{aligned} \tag{1.1}$$

with couplings $J_\chi > 0$, $J_1 < 0$ and $J_d > 0$ inspired by the rich physics surrounding the Kapellasite mineral. In the limit of dominant staggered chirality J_χ this model describes a CSL,[29,41] whereas for $J_d \gg J_\chi$ the model describes weakly coupled AFM chains along the diagonals of the hexagons on the Kagome lattice. For simplicity, we neglect the next-nearest-neighbor interaction J_2, which is negligible for Kapellasite.[19] The main motivation is that the interactions are dominated between in-plane Cu ions, and, consequently, an effective theoretical model in two dimensions can be proposed, as the Kagome layers become weakly coupled [Fig. (1.1)] in the Kapellasite. Additionally, we also investigate how ordered phases of matter can be understood from the perspective of the static spin structure factor (SSSF) and the gradient descent method (GD). Specifically, we investigate the classical phase diagram for the model (3).

This dissertation is then organized as follows:

- In Chapter 2 we present the methodology implemented in this dissertation, by explaining the gradient descent method and how magnetically ordered phases can be found by using this technique in the limit of classical spins $S \gg 1$. Subsequently, we investigate how the Variational Monte Carlo (VMC), based on the conjunction of the quantum variational principle and Markov Chain Metropolis-Hastings Monte Carlo, can be used to probe QSLs in the regime of quantum spins $S \ll 1$. To bridge both limits we also present how a spin density wave (SDW) class of Ansätze can be used to investigate the transition between ordered and disordered phases in the presence of quantum fluctuations.

- In Chapter 3 we present our results concerning the classical phase diagram for the $J_1 - J_d - J_\chi$ modified Heisenberg model (1.1). We report on new phases FM-chiral, FM-stripe, and AFM-stripe which arise due to the introduction of the staggered chiral interaction in the modified Heisenberg model. Specifically, by constructing the classical phase diagram of the model, we have found evidence of an extended classically disordered region for small J_1 and J_d coupling. In addition, we have also found numerical evidence for a second-order phase transition between the cuboc-1 and cuboc-2 phases previously reported for the Kagome lattice, with an octahedral phase occupying the line $J_1 = 0$ where the staggered chirality is maximized. These new classical phases may be interesting for materials similar to the Kapellasite mineral.

- Chapter 4 is devoted to discussions regarding the quantum phase diagram for the $J_1 - J_d - J_\chi$ modified Heisenberg model (1.1). We present the recently developed mean-field theory for chiral spin liquids (CSL) in the Kagome lattice,[12] and investigate them within the VMC. As we shall see, our results indicate a considerable region where the CSL is favored, in agreement with the results of Chapter 3. In addition, we investigate the transition between the ordered and disordered phases via the SDW Ansätze, obtaining a smaller, but still a considerable region where the CSL is energetically favorable in the quantum phase diagram.

- Finally, in Chapter 5 we summarize our results and discuss how further improvements to our methodology could be addressed in future work.

2 NUMERICAL AND THEORETICAL METHODOLOGY

In this chapter, we lay the foundations for our theoretical and numerical methodology to explore ordered and disordered states. We begin by considering the importance of the static spin structure factor (SSSF) for detecting magnetically ordered phases and how they are considered in conjunction with a gradient descent (GD) algorithm to characterize classical phase diagrams. From an initial benchmark, we review previous results in the literature about possible ordered phases known to occur in modified Heisenberg models on the Kagome Lattice and show how they can be compared within our algorithm from the ground state energy (GSE) observable's perspective. This development is essential for our independent studies in Chapter 3.

Following this classical treatment, we consider how quantum spin liquids can be studied using the formalism of parton construction, and how to go beyond the mean-field treatment by implementing a Variational Monte Carlo with physically motivated projected wave functions. Likewise, we present important numerical benchmarks on Section 2.3 that elucidate essential aspects of the Variational Monte Carlo algorithm as well as physical intuition necessary for Chapter 4.

2.1 Gradient descent and classical phases on the Kagome lattice

2.1.1 Static Spin Structure Factor

The magnetic order or disorder of a specific material can be probed through inelastic neutron scattering experiments.[55] The particles called neutrons have a small magnetic moment, i.e., an intrinsic magnetic dipole moment μ_N, which corresponds to approximately 0.1% of the electron's magnetic dipole moment. This is sufficiently low to characterize neutron diffraction in a material as a weakly interacting probe. The neutron beam deviated by a local field produced by the spins in a real material can then furnish experimental results to investigate both electron spin fluctuations and ordered magnetic structures in condensed matter physics.[56–58]

In order to quantify the phase transition between ordered and disordered states, we need a specific order parameter - understood within Landau's theory of phase transitions.[59] The first step for defining this observable is calculating the Fourier Transform of a generic spin configuration $\boldsymbol{S_r}$ via

$$\boldsymbol{S_k} = \frac{1}{\sqrt{N}} \sum_{\boldsymbol{r}} e^{-i\boldsymbol{r}\cdot\boldsymbol{k}} \boldsymbol{S_r}, \tag{2.1}$$

where N is the number of spins (or sites) in the lattice, with L representing the linear size of the system. Since our main interest in this dissertation is based on studying ordered and disordered phases on the Kagome Lattice, we also define it as containing three sublattices labeled by the letters A, B and C that are accessible by the position vectors

$$\begin{cases} \boldsymbol{r_A} = n_1\boldsymbol{a}_1 + n_2\boldsymbol{a}_2 \\ \boldsymbol{r_B} = \left(n_1 + \frac{1}{2}\right)\boldsymbol{a}_1 + n_2\boldsymbol{a}_2 \\ \boldsymbol{r_C} = n_1\boldsymbol{a}_1 + \left(n_2 + \frac{1}{2}\right)\boldsymbol{a}_2 \end{cases}, \tag{2.2}$$

with $n_1, n_2 = 1, \ldots, L$, and reciprocal $\boldsymbol{b_i}$ and primitive $\boldsymbol{a_i}$ lattice vectors given by

$$\begin{cases} \boldsymbol{b}_1 = \frac{2\pi}{a}\left(1, -\frac{\sqrt{3}}{3}\right) \\ \boldsymbol{b}_2 = \frac{2\pi}{a}\left(0, 2\frac{\sqrt{3}}{3}\right) \end{cases}, \tag{2.3}$$

and

$$\begin{cases} \boldsymbol{a}_1 = a\left(1, 0\right) \\ \boldsymbol{a}_2 = \frac{a}{2}\left(1, \sqrt{3}\right) \end{cases}, \tag{2.4}$$

with a representing the lattice spacing. The nearest-neighbor vectors are defined in Figure 4. The momentum $\boldsymbol{k}$ values are obtained through the relation

$$\boldsymbol{k} = \frac{m_1}{L}\boldsymbol{b}_1 + \frac{m_2}{L}\boldsymbol{b}_2 = \frac{2\pi}{La}\left[m_1\hat{\mathbf{x}} + \frac{\sqrt{3}}{3}\left(2m_2 - m_1\right)\hat{\mathbf{y}}\right], \tag{2.5}$$

with $m_1, m_2 = 0, \ldots, L-1$. The correspondent equation (2.1) for a particular configuration on the Kagome Lattice is then defined as

$$\boldsymbol{S_k} = \frac{1}{\sqrt{N}}\sum_{\boldsymbol{r}_A} e^{-i\boldsymbol{r}_A\cdot\boldsymbol{k}}\boldsymbol{S}_{\boldsymbol{r}_A} + \frac{1}{\sqrt{N}}\sum_{\boldsymbol{r}_B} e^{-i\boldsymbol{r}_B\cdot\boldsymbol{k}}\boldsymbol{S}_{\boldsymbol{r}_B} + \frac{1}{\sqrt{N}}\sum_{\boldsymbol{r}_C} e^{-i\boldsymbol{r}_C\cdot\boldsymbol{k}}\boldsymbol{S}_{\boldsymbol{r}_C}. \tag{2.6}$$

From the lattice definition (2.2) and the relation $\boldsymbol{a}_i \cdot \boldsymbol{b}_j = 2\pi\delta_{ij}$ between reciprocal and

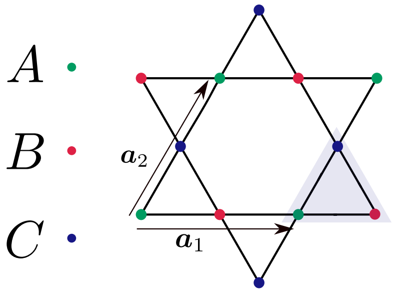

Figure 4 – Representation of the Kagome lattice with 3 atoms per unit cell (blue parallelogram). The nearest neighbors are defined as $\delta_i = \frac{\mathbf{a}_i}{2}$ for $i = 1, 2, 3$.
Source: By the author.

primitive lattice vectors,[60] equation (2.6) can be rewritten as

$$\boldsymbol{S_k} = \boldsymbol{S}^{A}_{m_1,m_2} + e^{-i\theta_B(m_1,m_2)}\boldsymbol{S}^{B}_{m_1,m_2} + e^{-i\theta_C(m1,m2)}\boldsymbol{S}^{C}_{m_1,m_2} \tag{2.7}$$

with the *phase factors*

$$\theta_B\left(m_1, m_2\right) = \pi m_1/La, \quad \theta_C\left(m_1, m_2\right) = \pi m_2/La \tag{2.8}$$

and

$$\boldsymbol{S}^{A(B,C)}_{m_1,m_2} = \frac{1}{\sqrt{N}} \sum_{n_1,n_2} e^{-2\pi i(m_1 n_1+m_2 n_2)/La} \boldsymbol{S}_{\boldsymbol{r}_{A(B,C)}}, \tag{2.9}$$

such that the *static spin structure factor* (SSSF) observable can finally be defined as

$$\mathcal{S}\left(m_1, m_2\right) = \boldsymbol{S}_{\boldsymbol{k}} \cdot \boldsymbol{S}_{-\boldsymbol{k}} = \left|\boldsymbol{S}_{\boldsymbol{k}}\right|^2 . \tag{2.10}$$

A minimal example can be analytically calculated for the ferromagnetic (FM) phase on the Kagome lattice. Following the condition

$$\boldsymbol{S}_{\boldsymbol{r}_A} = \boldsymbol{S}_{\boldsymbol{r}_B} = \boldsymbol{S}_{\boldsymbol{r}_C} \tag{2.11}$$

the Fourier transform (2.7) of the spin configuration for the FM phase becomes

$$\boldsymbol{S}_k = S\sqrt{L^2}\delta_{\boldsymbol{k},\boldsymbol{G}}\left(1 + e^{-i\pi m_1/La} + e^{-i\pi m_2/La}\right) \tag{2.12}$$

with $\boldsymbol{G}$ representing a reciprocal lattice vector. The SSSF (2.10) can then be obtained as

$$\mathcal{S}\left(\boldsymbol{k}\right) = \left|\boldsymbol{S}_{\boldsymbol{k}}\right|^2 = NS^2\delta_{\boldsymbol{k},\boldsymbol{G}}\left\{1 + \frac{2}{3}\left[\cos\left(k_0 m_1\right) + \cos\left(k_0 m_2\right) + \cos\left(k_0\left(m_1 - m_2\right)\right)\right]\right\}, \tag{2.13}$$

with $k_0 = \frac{\pi}{La}$. This result states that for reciprocal lattice points $\boldsymbol{k} = \boldsymbol{G} \neq \boldsymbol{\Gamma} = (0,0)$ in the reciprocal lattice, the SSSF is suppressed by a ratio of approximately $1/9$.[18] The momentum points upon which the SSSF acquires a considerable magnitude are known as *Bragg Peaks* in the momentum space. Correspondingly, they mark the position of the ordering wave vector $\boldsymbol{Q}$.[18,61] The numerical implementation of the SSSF can be seen in Algorithm 1).

Algorithm 1 Static Spin Structure Factor

---

1. Start with an initial spin configuration $\boldsymbol{S}_{\boldsymbol{r}}$ as input.
2. Define the correspondent geometrical lattice.
3. Calculate the phase factors (2.8) and the correspondent representation of the input configuration in momentum space (2.7) via a discrete Fourier Transform.
4. Calculate the correspondent SSSF via expression (2.10).

From these considerations, the SSSF (2.10) can then be understood as an order parameter when analyzing transitions between ordered and disordered phases in the classical regime. Once a minimum energy state - characterized by a spin configuration $\boldsymbol{S}_{\boldsymbol{r}}$ - is found numerically, it can be used as an input to the numerical implementation of the SSSF at Algorithm 1. The correspondent structure of the Bragg Peaks on the momentum space can then be compared to known ordered phases in the literature. If the weight of $S\left(\boldsymbol{k}\right)$ is spread over the Brillouin Zone (BZ) contour, we understand it as a *disordered phase*. Consequently, this result can be is a powerful indicator of the presence of quantum spin liquids,[62] as we will see through this dissertation.

2.1.2 Gradient Descent method

For a characterization of classical phase diagrams, the numerical implementation of the SSSF can be used in conjunction with the steepest descent or gradient descent (GD) method.[63] The GD method is an interesting alternative to the Luttinger-Tisza method[64–67] in the scenario where interactions of three or more spins are considered - chiral interactions on the elementary triangles of the Kagome lattice, for example. The main idea of this algorithm in the present context is to represent the part of the Hamiltonian that does not depend on $\boldsymbol{S}_i$ as a local field $\boldsymbol{h}_i$ which influences the system to stabilize in a particular configuration that minimizes the ground state energy. As an illustrative example, we may consider the $J_1 - J_d - J_\chi$ Kagome Lattice model (1.1),

$$\mathcal{H}_{GD} = \sum_i \boldsymbol{S}_i \cdot \boldsymbol{h}_i, \tag{2.14}$$

with the local fields determined by

$$\boldsymbol{h}_i = J_1 \sum_j \boldsymbol{S}_j + J_d \sum_{j \in \hexagon} \boldsymbol{S}_j + J_\chi \sum_{j,k \in \triangle\triangledown} \left(\boldsymbol{S}_j \times \boldsymbol{S}_k\right). \tag{2.15}$$

It's clear from the functional form (2.14) and from

$$\nabla_i \mathcal{H}_{GD} = \frac{\partial \mathcal{H}_{GD}}{\partial S_i^x}\hat{x} + \frac{\partial \mathcal{H}_{GD}}{\partial S_i^y}\hat{y} + \frac{\partial \mathcal{H}_{GD}}{\partial S_i^z}\hat{z} = \boldsymbol{h}_i \tag{2.16}$$

that any configuration upon which $-\nabla_i \mathcal{H}_{GD}\left(\boldsymbol{S}_i\right) \parallel \boldsymbol{h}_i$ will decrease the ground state energy of the system. Therefore, an algorithm can be constructed by following the opposite path of the gradient on the energy surface (following the gradient leads to a maximum). This local minimization method is known as *gradient descent*, or steepest descent. Since this is a local optimization algorithm, different random configurations are needed to confirm that the algorithm is not trapped in a local minimum. The correspondent structure of the GD method can be seen at Algorithm 2.

The parameter $\gamma \in [0, 1]$ is labeled as step size *, and it's a numerical correction that improves the numerical convergence. Small γ means that the algorithm will need more steps to converge to the configuration of minimum energy. When $\gamma = 1$, the spins are aligned with the local fields. For all investigations in this dissertation, we use $\gamma = 0.7$.

The main idea on obtaining classical phase diagrams is then to directly minimize the energy of the system - which in this dissertation will always be described by a modified Heisenberg model -, and compare the final configuration with relevant ordered phases known in the literature for the specific lattice considered. This comparison can be done between analytical (or numerical) ground state energies and the correspondent minimum

---

* Also known as learning step in the context of machine learning.[63]

Algorithm 2 Gradient Descent method

```
1. Start with an initial (often random) spin configuration $\boldsymbol{S}_i^0$.
2. Flip the $\boldsymbol{S}_i$ spin in the direction of the local downhill of the gradient $-\nabla_i \mathcal{H}(\boldsymbol{S}_i)$ via
       $\boldsymbol{S}_{i+1} = (1-\gamma)\,\boldsymbol{S}_i - \gamma \nabla_i \mathcal{H}(\boldsymbol{S}_i)\,,$
   where $\gamma \in [0,1]$.
3. Normalize the new spins such that $|\boldsymbol{S}_{i+1}| = S$.
4. Sweep over the lattice flipping all spins repeating step 3 for all spins.
5. Repeat the process as many times as needed or until a tolerance limit is reached,
   which occurs when the overall change in the spin configuration after the $m$-th
   interaction is smaller than a tolerance $\varepsilon = 10^{-10}$.
```

energy found by the GD method, alongside the characterization of the SSSF profile for the configuration. In the following discussions, we are going to consider relevant benchmarks within this context to evidence the reliability of our implementation.

2.1.3 Classical Benchmarks: From Néel AFM to noncoplanar phases

It is now known by distinct theoretical and numerical approaches that there is a rich classical phase diagram for the $S = 1/2$ kagome antiferromagnet (KAFM) model if further neighbor interactions are taken into account in Heisenberg-like models.[2,19] Considering first-neighbor interactions $J_1 > 0$ (AFM) is a paradigmatic example for a QSL, for example,[8] which will be explored in Subsection 2.3.0.2. In contrast, if $J_1 < 0$ (FM) interactions are considered, additional couplings are necessary for stabilizing a QSL (as we will see in Chapter 4).[13,41] These new interactions may also select magnetically ordered states which are energetically competitive in a certain region of the phase space of coupling parameters from the effective model. One way of classifying and finding these phases is by selecting spin spatial configurations which respect all lattice and spin symmetries of a given lattice in a group-theoretical approach.[18,61] Furthermore, the energy of these states can be compared variationally to discover at least one exact lower energy bound in the case where the classical spin configuration is not the true ground state of the model. This formalism is quite useful when one has information about the magnetic correlations of a magnetic compound through experimental data from neutron scattering patterns on the reciprocal lattice, i.e., via the previously mentioned SSSF. If this pattern is reproduced in an experimental setup, one can have additional information about how the couplings from the effective model hosting the ordered phase interact to generate the classical phases. In this context, we represent the spins as classical vectors and introduce local angles

$\phi \in [0, 2\pi]$ and $\theta \in [0, \pi]$ as

$$\boldsymbol{S}_i = S\left(\cos\phi_i \sin\theta_i, \sin\phi_i \sin\theta_i, \cos\theta_i\right). \tag{2.17}$$

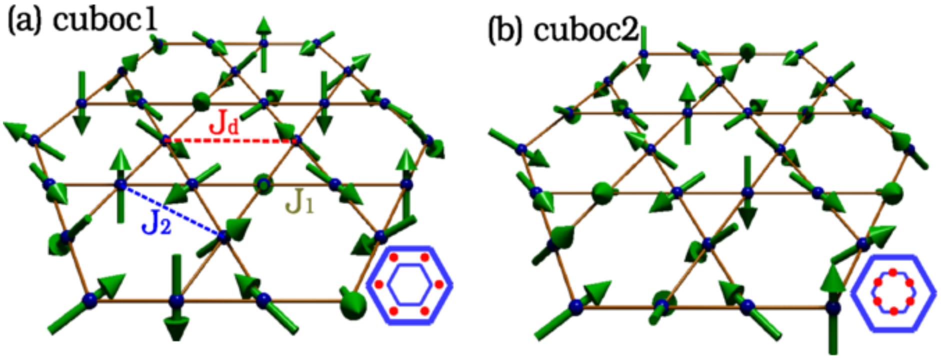

Figure 5 – Spin spatial configuration of the cuboc-1 (a) and cuboc-2 (b) phases on the Kagome lattice alongside their correspondent SSSF.
Source: GONG *et al.*[54]

To investigate these states and benchmark our numerical implementations of the SSSF and GD method, we begin by considering the $J_1 - J_2$ Heisenberg model

$$H = J_1 \sum_{\langle i,j \rangle} \mathbf{S}\left(\mathbf{r}_i\right) \cdot \mathbf{S}\left(\mathbf{r}_j\right) + J_2 \sum_{\langle\langle i,j \rangle\rangle} \mathbf{S}\left(\mathbf{r}_i\right) \cdot \mathbf{S}\left(\mathbf{r}_j\right), \tag{2.18}$$

upon which we expect a phase transition from the cuboc-2 to the ferromagnetic phase when varying the J_2 interaction, for example. The *cuboc phases* (Fig. 5) display long-range magnetic order in a disposition of 12 noncoplanar sublattices pointing to the vertices of a polyhedron called cuboctahedron. The difference between the cuboc-2 and cuboc-1 phases is that the first has all six spins from the hexagon in the same plane while having an angle of $\pi/3$ between nearest neighbors - contributing to a non-zero expectation value of the chirality order parameter -, whereas in the latter there is no chirality on the elementary triangles of the Kagome lattice. The cuboc-2 phase has also been investigated in both classical and quantum limits; spin wave calculations have demonstrated that this phase

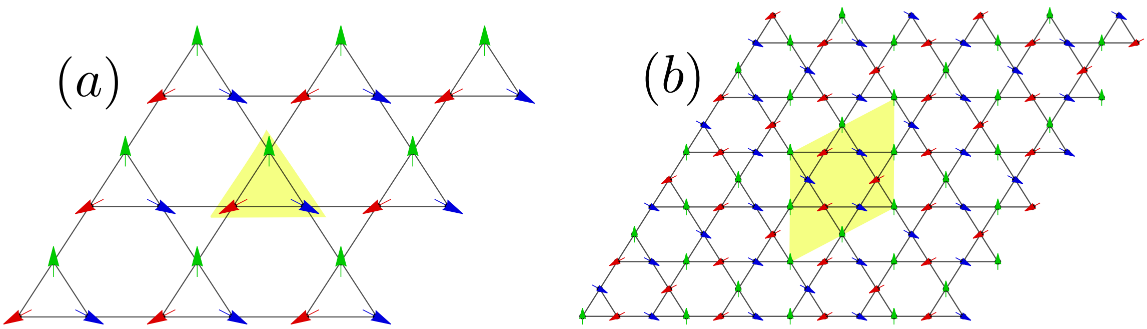

Figure 6 – Spin spatial configuration of the AFM coplanar states $\boldsymbol{Q} = 0 \times 0$ (a) and $\boldsymbol{Q} = \sqrt{3} \times \sqrt{3}$ (b) on the Kagome Lattice.[1]
Source: By the author.

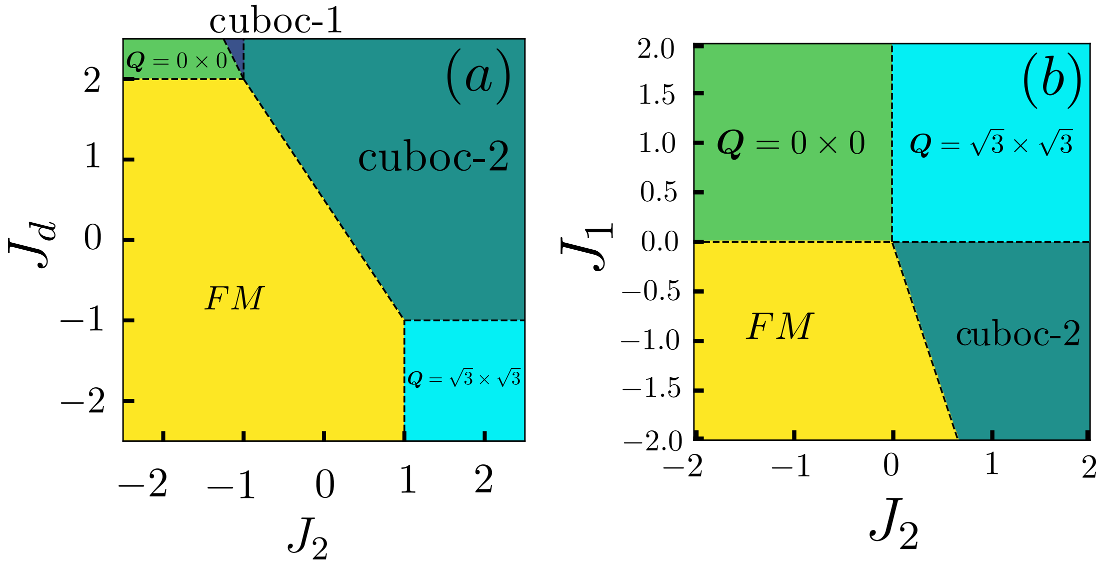

Figure 7 – Classical phase diagram for the $J_1 - J_2 - J_d$ - with $J_1 = -1$ (a) and $J_1 - J_2$ (b) Heisenberg models in the Kagome Lattice. Black dashed lines represent first order phase transition boundaries.[2,3]
Source: By the author.

is stable in the AFM $J_1 - J_2$ model even in the presence of quantum fluctuations: we understand it as being the classical cuboc-2 state renormalized by quantum fluctuations.[2] In addition, there's a possible transition from the previously mentioned phases to Neél AFM coplanar phases $\boldsymbol{Q} = 0 \times 0$ and $\boldsymbol{Q} = \sqrt{3} \times \sqrt{3}$ (Figure 5), which are favored for $J_2 < 0$ and $J_2 > 0$, respectively. Their nomenclature are related to the corresponding ordering wave vector $\boldsymbol{Q}$. For the former, the traditional unit cell containing three sites is sufficient to describe the periodicity of the ordered phase, whereas for the latter the unit cell must be increased. Physically the diffracted neutron beams interfere destructively within the unit cell such that sharp peaks in the Brillouin Zone (BZ) appear only at the edges of the 1st BZ for the phase $\boldsymbol{Q} = 0 \times 0$ (Fig. 8).[2,68]

With the addition of the J_d interactions (on the diagonals of the elementary hexagons on the Kagome lattice) in the Heisenberg Model (2.18), i.e., $H_d = J_d \sum_{ij \in \hexagon} \mathbf{S}(\mathbf{r}_i) \cdot \mathbf{S}(\mathbf{r}_j)$ the phase diagram becomes even richer, with the aforementioned phases and a new paramagnetic (disordered) region established for intermediate J_d in the quantum regime - between the FM and cuboc-2 phases - indicating a susceptible region for the quantum spin liquid.[19] From density functional theory (DFT) results[19,52,53] the Kapellasite material is described by the couplings $(J_1, J_2, J_d) = (-12.5, -0.55, 16.1)\,K$, for example. The classical phase diagram is also well described within our numerical investigations (Fig. 5).

2.2 Parton Construction and Variational Monte Carlo

From the different ways of expressing spin operators as bosonic or fermionic degrees of freedom, the physical picture for a particular representation is motivated by the low-

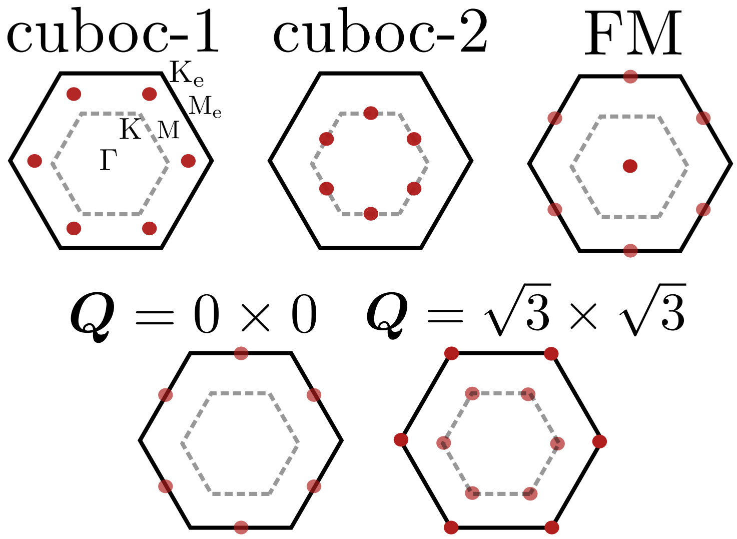
cuboc-1
cuboc-2
FM
K$_e$
M$_e$
K
M
Γ
$\boldsymbol{Q} = 0 \times 0$
$\boldsymbol{Q} = \sqrt{3} \times \sqrt{3}$

Figure 8 – The SSSF for phases cuboc-2, cuboc-1, FM, $\boldsymbol{Q} = 0 \times 0$ and $\boldsymbol{Q} = 3 \times 3$ are presented, with the BZ (dashed gray lines) and extended BZ (solid black lines). The positions of highly symmetric momentum points Γ, K, M, K$_e$, M$_e$, are also presented. The color intensity for each profile is only schematic and, consequently, independent between different phases. [2,3]
Source: By the author.

energy theory describing the considered material. For QSLs the *Parton Construction* is an interesting representation that contains the fractionalized excitations, and the absence of ordinary magnetic order.[7] This representation surpasses the bad quantum number definition $\langle S \rangle$, which is zero for these disordered states, allowing a well-defined mean-field theory development.[11] Additionally, even free electrons in this formalism do not obey the bipartite entropy entanglement area law of $S \propto L$ in two dimensions, where L is the length of the system. Instead, the entropy scales with $S \propto L \log L$, indicating the presence of a massive entanglement between the spins in this representation.[7,69–71]

In this section, we investigate the quantum limit of Heisenberg-like models with S=1/2. The parton construction contrasts with the usual spin-wave treatment in this context.[72,73] The low-energy spectrum is dominated by delocalized spin bosonic excitations called *magnons*. This formalism describes well the Néel ordering in the AFM Heisenberg model in square lattices, for example, with a staggered magnetization $m_s \approx 0.303$ close to the exact numerical result $m_s \approx 0.307$,[74] as well as good estimates to the ground state energy. The agreement for m_s in the square lattice to the classical result 1/2 can be traced back to a small number of bosons in the energy spectrum. Additionally, the results in one-dimensional AFM chains indicate a logarithmic divergence of m_s, indicating that quantum fluctuations melt the magnetic order in this system. As we shall see in Subsection 2.3.0.1, the Parton construction can effectively describe this disordered ground state when the Gutzwiller projected wave functions are considered within the VMC. Subsequently, we present how these ideas can be implemented numerically within the VMC and explore more examples of QSLs in the context of the Kagome lattice.

2.2.1 Fermionic Abrikosov Representation

We begin our studies by first decomposing the Heisenberg Hamiltonian in components as a function of spin ladder operators,[75] $S_i^+ = \left(S_i^+ + S_i^-\right)/2$ and $S_i^- = \left(S_i^+ - S_i^-\right)/2i$, as

$$\mathcal{H} = \frac{1}{2}\sum_{i,j} J_{ij}\left[S_i^z S_j^z + \frac{1}{2}\left(S_i^+ S_j^- + S_i^- S_j^+\right)\right], \tag{2.19}$$

with the usual spin commutation relations

$$\left[\hat{S}_m^i, \hat{S}_n^j\right] = i\delta_{mn}\epsilon^{ijk}\hat{S}_n^k, \quad \left[\hat{S}_i^+, \hat{S}_j^-\right] = 2\delta_{ij}S_i^z \quad \text{and} \quad \left[\hat{S}_i^z, \hat{S}_j^\pm\right] = \pm\delta_{ij}\hat{S}_i^\pm. \tag{2.20}$$

δ_{ij} being the usual Kronecker delta and ϵ^{ijk} the Levi-Civita symbol. The Abrikosov fermionic representation for the spin 1/2 operators is given by[7,8]

$$\boldsymbol{S} = \frac{1}{2}\sum_{\alpha,\beta} f_{i,\alpha}^\dagger \boldsymbol{\sigma}_{\boldsymbol{\alpha},\boldsymbol{\beta}} f_{i,\beta} \quad \text{with} \quad n_i = f_{i\uparrow}^\dagger f_{i\uparrow} + f_{i\downarrow}^\dagger f_{i\downarrow} = 1, \tag{2.21}$$

and $\boldsymbol{\sigma} = (\sigma_x, \sigma_y, \sigma_z)$ a vector with the Pauli matrices. After the mapping (2.23) for spins, the constraint relation is necessary in order for the model to depict the correct physical Hilbert space. This is a general remark when translating physical degrees of freedom into different representations. For the Abrikosov formalism, we restrict our configuration space to the one with only one fermion per site via $n_i = 1$, which is usually imposed globally via a Lagrange multiplier in the physical Hamiltonian. The necessity of this condition can be further reinforced if one notes that by using the mapping (2.23) and the anti-commutation relations (2.24), the quantity

$$\boldsymbol{S}_i^2 = \frac{3}{4}n_i\left(2 - n_i\right) \tag{2.22}$$

only matches $\boldsymbol{S}_i^2 = S\left(S+1\right) = 3/4$ if the constraint in (2.21) is obeyed.[*]

The Abrikosov representation translates the spin ladder operators as

$$\hat{S}_i^+ = f_{i\uparrow}^\dagger f_{i\downarrow}, \quad \hat{S}_i^- = f_{i\downarrow}^\dagger f_{i\uparrow,} \quad \text{and} \quad \hat{S}_i^z = \frac{1}{2}\left(n_{i\uparrow} - n_{i\downarrow}\right), \tag{2.23}$$

where $f_{i\tau}^\dagger$ $(f_{i\tau})$ represents a fermionic creation (destruction) operator of a chargeless fermion with spin τ (spinon). Additionally, $n_{i\tau} = f_{i\tau}^\dagger f_{i\tau}$ is the usual occupation number for a spin flavor τ on the site i. Spinons arise as a natural description of QSLs excitations of spin in this formalism[†]. These spinons can also be seen as a product of the decay of magnons, a process that is experimentally characterized by a blurry in the SSSF. The spin liquid's low-energy properties are then faithfully represented by these objects, and they can be experimentally detected from thermodynamic and spectroscopic quantities. These operators obey the usual anti-commutation relations

---

[*] A similar Parton construction (2.21) in terms of *Schwinger bosons* can also be explored with $f_{i\sigma}\left(f_{i\sigma}^\dagger\right) \to b_{i\sigma}\left(b_{i\sigma}^\dagger\right)$ representing bosonic operators. In this case, the physical constraint (2.21) is replaced by the condition $n_i = \sum_\alpha b_{i\alpha}^\dagger b_{i\alpha} = 2S$[7,76,77] with S representing the spin value as usual.

[†] Quasiparticles are an essential ingredient for our description of emergent phenomena by representing collective interactions in a solid.[78] In this case, if we consider the electron as a bound state of charge, spin and orbital degrees of freedom, the spinon description captures the essential characteristic of spin excitations at low temperature ($T \lesssim J$).[79]

$$\left\{f_{i\sigma}, f^{\dagger}_{j\tau}\right\} = \delta_{ij}\delta_{\tau\sigma}, \quad \{f_{i\sigma}, f_{j\tau}\} = 0 \quad \text{and} \quad \left\{f^{\dagger}_{i\sigma}, f^{\dagger}_{j\tau}\right\} = 0, \tag{2.24}$$

and, consequently, the spin commutation relations (2.20) as shown below.

Proof. We consider the commutation relation $\left[\hat{S}^{+}_{i}, \hat{S}^{-}_{j}\right] = 2\delta_{ij}S^{z}_{i}$ and make extensive use of the relations (2.24):

$$-\hat{S}^{-}_{j}\hat{S}^{+}_{i} = -f^{\dagger}_{j\downarrow}f_{j\uparrow}f^{\dagger}_{i\uparrow}f_{i\downarrow} = f^{\dagger}_{j\downarrow}f^{\dagger}_{i\uparrow}f_{j\uparrow}f_{i\downarrow} - \delta_{ij}f^{\dagger}_{j\downarrow}f_{i\downarrow} = f^{\dagger}_{i\uparrow}f^{\dagger}_{j\downarrow}f_{i\downarrow}f_{j\uparrow} - \delta_{ij}f^{\dagger}_{j\downarrow}f_{i\downarrow} =$$

$$= 2\delta_{ij}\frac{1}{2}\left(f^{\dagger}_{j\uparrow}f_{i\uparrow} - f^{\dagger}_{j\downarrow}f_{i\downarrow}\right) - f^{\dagger}_{i\uparrow}f_{i\downarrow}f^{\dagger}_{j\downarrow}f_{j\uparrow} = 2\delta_{ij}S^{z}_{i} - \hat{S}^{+}_{i}\hat{S}^{-}_{j}. \tag{2.25}$$

Analogously, we have

$$-\hat{S}^{+}_{j}\hat{S}^{z}_{i} = -\frac{1}{2}f^{\dagger}_{j\uparrow}f_{j\downarrow}n_{i\uparrow} + \frac{1}{2}f^{\dagger}_{j\uparrow}f_{j\downarrow}n_{i\downarrow} = \tag{2.26}$$

$$= \frac{1}{2}\left(\delta_{ij}f^{\dagger}_{i\uparrow}f_{j\downarrow} - f^{\dagger}_{i\uparrow}f_{i\uparrow}f^{\dagger}_{j\uparrow}f_{j\downarrow\uparrow}\right) + \frac{1}{2}\left(\delta_{ij}f^{\dagger}_{i\uparrow}f_{j\downarrow} - f^{\dagger}_{i\downarrow}f_{i\downarrow}f^{\dagger}_{j\uparrow}f_{j\downarrow\uparrow}\right) = \tag{2.27}$$

$$= \frac{1}{2}\left(\delta_{ij}f^{\dagger}_{i\uparrow}f_{j\downarrow} + \delta_{ij}f^{\dagger}_{i\uparrow}f_{j\downarrow}\right) - \frac{1}{2}\left(f^{\dagger}_{i\downarrow}f_{i\downarrow}f^{\dagger}_{j\uparrow}f_{j\downarrow\uparrow} + f^{\dagger}_{i\uparrow}f_{i\uparrow}f^{\dagger}_{j\uparrow}f_{j\downarrow\uparrow}\right) = +\delta_{ij}\hat{S}^{+}_{i} - \hat{S}^{z}_{i}\hat{S}^{+}_{j}. \tag{2.28}$$

The remaining commutation relations at (2.20) then follow. ■

The Hamiltonian (2.19) can then be rewritten via the Abrikosov representation and the constraint relation as

$$\mathcal{H} = \frac{1}{2}\sum_{ij} J_{ij}\left[\frac{1}{2}\left(f^{\dagger}_{i\uparrow}f_{i\downarrow}f^{\dagger}_{j\downarrow}f_{j\uparrow} + h.c.\right) + \frac{1}{4}\left(n_{i\uparrow} - n_{i\downarrow}\right)\left(n_{j\uparrow} - n_{j\downarrow}\right)\right] =$$

$$= \frac{1}{2}\sum_{ij} J_{ij}\left\{\frac{1}{2}\left(f^{\dagger}_{i\uparrow}f_{i\downarrow}f^{\dagger}_{j\downarrow}f_{j\uparrow} + f^{\dagger}_{i\downarrow}f_{i\uparrow}f^{\dagger}_{j\uparrow}f_{j\downarrow}\right) + \left[\frac{1}{4} - \frac{1}{2}\left(f^{\dagger}_{i\uparrow}f_{i\uparrow} + f^{\dagger}_{j\uparrow}f_{j\uparrow}\right) + n_{i\uparrow}n_{j\uparrow}\right]\right\}. \tag{2.29}$$

To be able to gain an insight into the ground state energy and spin correlations analytically, we can implement a Mean Field Theory (MFT) approximation. We replace the constraint (2.21) with the half-filling condition on average $\langle GS\left|n_{i\uparrow} + n_{i\downarrow}\right| GS\rangle = \langle n_{i\uparrow} + n_{i\downarrow}\rangle \approx 1$, and introduce the decoupling operator

$$\chi_{ij} = f^{\dagger}_{i\uparrow}f_{j\uparrow} + f^{\dagger}_{i\downarrow}f_{j\downarrow} \tag{2.30}$$

such that

$$\mathcal{H} = \frac{1}{2}\sum_{ij} J_{ij}\left[\frac{1}{4} - \frac{1}{2}\chi^{\dagger}_{ij}\chi_{ij}\right], \tag{2.31}$$

as proven below.

Proof. This step can be understood if we consider the following calculations

$$\begin{aligned}\frac{1}{4}-\frac{1}{2}\chi_{ij}^{\dagger}\chi_{ij} &= \frac{1}{4}-\frac{1}{2}\left[1+\left(-n_{j\downarrow}n_{i\downarrow}-n_{j\uparrow}n_{i\uparrow}\right)-\left(f_{i\downarrow}^{\dagger}f_{i\uparrow}f_{j\uparrow}^{\dagger}f_{j\downarrow}\right)-\left(f_{i\uparrow}^{\dagger}f_{i\downarrow}f_{j\downarrow}^{\dagger}f_{j\uparrow}\right)\right]= \\ &= \frac{1}{4}-\frac{1}{2}\left[1+\left[-1-n_{i\uparrow}n_{j\uparrow}+\left(n_{j\uparrow}+n_{j\uparrow}\right)\right]-\left(f_{i\downarrow}^{\dagger}f_{i\uparrow}f_{j\uparrow}^{\dagger}f_{j\downarrow}\right)-\left(f_{i\uparrow}^{\dagger}f_{i\downarrow}f_{j\downarrow}^{\dagger}f_{j\uparrow}\right)\right].\end{aligned}$$

■

We proceed the MFT treatment with the approximation that quadratic fluctuations $(A-\langle A\rangle)(B-\langle B\rangle)$ are negligible in the form $AB=(A-\langle A\rangle)(B-\langle B\rangle)+A\langle B\rangle+\langle B\rangle A-\langle A\rangle\langle B\rangle$ for any product of two 2-body operators, if deviations of the mean values are small. Applying this for the decoupling operator at equation (2.31)

$$\begin{aligned}\mathcal{H} &= -\frac{1}{4}\sum_{ij}J_{ij}\chi_{ij}^{\dagger}\chi_{ij}+\frac{zNJ}{8}\approx-\frac{1}{4}\sum_{ij}J_{ij}\left[\chi_{ij}\left\langle\chi_{ij}\right\rangle^{*}+\chi_{ij}^{\dagger}\left\langle\chi_{ij}\right\rangle-\left|\left\langle\chi_{ij}\right\rangle\right|^{2}\right]+\frac{zNJ}{8}= \\ &= -\frac{1}{4}\sum_{ij,\sigma}J_{ij}\left[\left\langle\chi_{ij}\right\rangle^{*}f_{i\sigma}^{\dagger}f_{j\sigma}+h.c.\right]+\frac{1}{4}\sum_{ij}J_{ij}\left|\left\langle\chi_{ij}\right\rangle\right|^{2}+\frac{zNJ}{8}, \qquad (2.32)\end{aligned}$$

where z is coordination number, or number of nearest neighbors. If we impose a real and uniform order parameter [*] $\langle\chi_{ij}\rangle^{*}=\langle\chi_{ij}\rangle=\chi$, the Hamiltonian can naturally be rewritten in a diagonal form as

$$\mathcal{H}=-\frac{1}{4}\sum_{ij,\sigma}J_{ij}\chi\left[f_{i\sigma}^{\dagger}f_{j\sigma}+h.c.\right]+\frac{zNJ\chi^{2}}{4}+\frac{zNJ}{8}. \qquad (2.33)$$

By taking advantage of the translational invariance of the physical system, we can further represent diagonalize it, via the Fourier transform of the spinon operators

$$f_{i\sigma}=\frac{1}{\sqrt{N}}\sum_{\boldsymbol{k}}e^{i\boldsymbol{k}\cdot\boldsymbol{R}_{i}}f_{\boldsymbol{k}\sigma},\ \frac{1}{N}\sum_{j}e^{i\boldsymbol{R}_{j}\cdot(\boldsymbol{k}-\boldsymbol{k}')}=\delta_{\boldsymbol{k},\boldsymbol{k}'}. \qquad (2.34)$$

Example: AFM Heisenberg model in 1D

For one-dimensional systems and next-neighbor interactions only, as a first estimate for the ground state energy, we may consider the S=1/2 antiferromagnetic (AFM) spin chain described by the Heisenberg model. Experimental results from inelastic neutron scattering (INS) and resonant inelastic x-ray scattering (RIXS)[80,81] confirmed that materials in this context like Sr_2CuO_3 and Yb_2Pt_2Pb, for example, display a continuum energy spectrum of spinons with long-range magnetic order suppressed by quantum fluctuations near $T\approx 0$.

From equation (2.33) with $a=1$ and $z=2$, the diagonal Hamiltonian is given by

$$\mathcal{H}=-\frac{1}{4}\sum_{\boldsymbol{k},\sigma}\varepsilon\left(\boldsymbol{k}\right)f_{\boldsymbol{k}\sigma}^{\dagger}f_{\boldsymbol{k}\sigma}+\frac{zNJ\chi^{2}}{4}+\frac{zNJ}{8}, \qquad (2.35)$$

---

[*] This particular choice is useful for a common metal, but an additional phase could be necessary with the consideration of an applied magnetic field, for example.

with a dispersion relation given by $\varepsilon(\boldsymbol{k}) = -2J\chi\cos ka$, where a is the lattice spacing. In this case,

$$\epsilon_0(\chi) = \frac{E_0}{NJ}(\chi) = -\frac{\chi}{2\pi}\int_{-\pi/2}^{\pi/2} dk\cos k + \frac{1}{2}\chi^2 + \frac{1}{4} = -\frac{\chi}{\pi} + \frac{\chi^2}{2} + \frac{1}{4} \tag{2.36}$$

and the corresponding value of χ can be found by a direct minimization $\frac{d\epsilon_0}{d\chi} = 0 \therefore \chi = 1/\pi$, which gives $\epsilon_0(1/\pi) = 0.19934$. This is a high estimation since the real ground state energy, is given by $E_0/N = 1/4 - \ln 2 = -0.44315$.[78,82,83] The spin-wave approach to this problem gives a much better result of $E_0/N = -0.4315$,[84,85] for example. The distinctiveness between the results for this observable can be understood from the approximation of the MFT at zeroth order since the physical constraint (2.21) is imposed only as an average. As we will see in Section 2.3, when considering this condition exactly within the Variational Monte Carlo (VMC), the energy observable can be much closer to the exact result.

The spin-spin correlations can also be estimated, since we can relate the spin operators with the density one by the Abrikosov representation for S^z via the equation (2.23) and the use of the half-filling condition $\langle n_{i\uparrow} + n_{i\downarrow}\rangle = 1$:

$$\begin{aligned}\langle S_0^z S_i^z\rangle &= \langle (n_{0\uparrow} - n_{0\downarrow})(n_{i\uparrow} - n_{i\downarrow})\rangle = 4\left\langle f_{0\uparrow}^\dagger f_{0\uparrow} f_{i\uparrow}^\dagger f_{i\uparrow} - \frac{1}{2}\left(f_{0\uparrow}^\dagger f_{0\uparrow} + f_{i\uparrow}^\dagger f_{i\uparrow}\right) + \frac{1}{4}\right\rangle = \\ &= 4\left\langle f_{0\uparrow}^\dagger f_{0\uparrow} f_{i\uparrow}^\dagger f_{i\uparrow}\right\rangle - \frac{1}{4}.\end{aligned} \tag{2.37}$$

This can be further represented in momentum space, by using the same steps from (2.33) to (2.35) as

$$\langle S_0^z S_r^z\rangle = \frac{4}{N^2}\sum_{k_1,k_2,k_3,k_4}\left\langle f_{k_1\uparrow}^\dagger f_{k_2\uparrow} f_{k_3\uparrow}^\dagger f_{k_4\uparrow}\right\rangle\left(e^{ir(k_4-k_3)} - 1\right). \tag{2.38}$$

Here, we have two contributions that are not eliminated from the orthonormality of states: i) Both orbitals are occupied: $k_1 = k_2$ and $k_3 = k_4$; ii) One orbital is occupied ($k_1 = k_4$) and the other one is empty ($k_2 = k_3$). The first one cancels the factor 1, and the second, written in terms of the occupation number of orbitals $n(k_1)$ and $[1 - n(k_2)]$ (empty orbital), transforms the expression as

$$\langle S_0^z S_r^z\rangle = \frac{4}{N^2}\frac{N^2}{(2\pi)^2}\int_{-\pi}^{\pi} dk_1\int_{-\pi}^{\pi} dk_2 n(k_1)[1 - n(k_2)]\, e^{ir(k_1-k_2)} =$$

$$= \frac{1}{\pi}\int_{-\pi}^{0} e^{irk_1}\delta(r-0)\, dk_1 + \frac{1}{\pi^2}\int_{-\pi}^{0} dk_1 e^{irk_1}\int_0^{\pi} dk_2 e^{-irk_2} = \delta_{0,r} + \left[\frac{1}{i\pi r}\left(1 - (-1)^r\right)\right]^2$$

$$\therefore \langle S_0^z S_r^z\rangle = \delta_{0,r} - \frac{2}{\pi^2 r^2}\left(1 - (-1)^r\right). \tag{2.39}$$

From the first to the second line we used the fact that the dispersion relation is particle-hole symmetric.[86] From the exact result for the $S = 1/2$ AFM spin chain,[82]

$$C(r) = \langle \boldsymbol{S}_i \cdot \boldsymbol{S}_{i+r}\rangle \sim \frac{(-1)^r}{r}, \tag{2.40}$$

we see that although the correlation decays algebraically (with $1/r^2$) at equation (2.39) for the Abrikosov representation, it does so with the wrong exponent. By adopting the Gutzwiller Projected wave functions this observable can also be also be improved from the perspective of the VMC.

2.2.2 Beyond MFT and Gauge Invariance

One possibility of going beyond the mean field solutions is by including phase fluctuations $a_{i,j}$[11] around the mean field ansatz $\bar{\chi}_{ij}$ as $\chi_{i,j} \to \bar{\chi}_{i,j} e^{-ia_{i,j}}$[*]. The new Hamiltonian will then invariant under the gauge transformations

$$f_{i,\sigma} \to e^{i\theta_i} f_{i,\sigma} \quad a_{i,j} \to a_{i,j} + \theta_i - \theta_j. \tag{2.41}$$

Therefore, from first-order mean-field theory, the fermionic spinons quasiparticles interact via an emergent gauge boson residing on the bonds (i,j) of a lattice. The particular structure of the gauge fields is entirely dependent on the mean-field ansatz theory (Table 1). The gauge fields are described by a U(1) lattice theory if $\theta \in \mathcal{R}$, and represent the degrees of freedom described by $a_{i,j}$.[87,88] Additionally, if $\theta = \{0, \pi\}$ we have a Z_2 gauge theory with parity symmetry. Since these symmetries are unphysical and arise due to the Parton representation (2.21) of spins, the gauge invariance is also referred to as gauge redundancy.[8]

Table 1 – Some examples of quantum spin liquids with their respective mean field theories, and possible low energy physics and excitations. For more examples see SAVARY *et al*[7] and ZHOU *et al.*[8]

	Mean Field Theory	Low energy & excitations
Superconductor	$\mathcal{H}_{MFT} = \sum_{ij} \left(f_i^\dagger f_j + \Delta_{ij} f_i^\dagger f_j^\dagger + \text{h.c.} \right)$	Topological QSL. Z_2 QSL Anyons, RVB
Semiconductor	$\mathcal{H}_{MFT} = \sum_i \varepsilon_i f_i^\dagger f_i +$ $+ \sum_{ij} \left(t_{ij} e^{ia_{ij}} f_i^\dagger f_j + \text{h.c.} \right)$	U(1) QSL Gapless photons
Semi-metal	$\mathcal{H}_{MFT} = \sum_{ij} \left(\tilde{t}_{ij} f_i^\dagger f_j + \text{h.c.} \right)$	U(1) QSL. Algebraic QSLs Dirac Fermions
Metal	$\mathcal{H}_{MFT} = \sum_{ij} \left(t_{ij} f_i^\dagger f_j + \text{h.c.} \right)$	U(1) QSL. Spinon Fermi Surface

Source: Adapted from SAVARY *et al.*[7]

How legitimate is this scenario? Is the Parton construction a reliable theoretical approach to described quantum spin liquids? We have seen that from zeroth order mean field theory the ground state energy is not well described within the context of the Heisenberg model, for example. One necessary extension is imposing the constraint in (2.21) exactly at each site and projecting the initial mean field wave functions onto the physical spin Hilbert space. This crucial step will still have remnants of the gauge invariance generated by the Parton construction. The new and physical trial wave functions

---

[*] Amplitude fluctuations of mean field parameters are discarded since a finite energy gap makes these fluctuations negligible for the physics describing the low-energy regime.

$$\Psi^{(\chi_{ij})}\left(\{\sigma_i\}\right) = \langle 0| \prod_i f_{i\sigma_i} \left|\Psi^{(\chi_{ij})}_{MFT}\right\rangle \tag{2.42}$$

generated by the Ansätze χ_{ij} and $\tilde{\chi}_{ij}$ connect by a gauge transformation

$$\tilde{\chi}_{ij} = \bar{\chi}_{i,j} e^{-ia_{i,j}} = e^{i\theta_i}\chi_{ij}e^{-i\theta_j} \tag{2.43}$$

will generate the same projected spin state[11]

$$\Psi^{(\tilde{\chi}_{ij})}\left(\{\sigma_i\}\right) = e^{i\sum_i \theta_i}\Psi^{(\chi_{ij})}\left(\{\sigma_i\}\right) \tag{2.44}$$

The gauge invariance, therefore, furnishes different labels, which are characterized by gauge fluxes, to describe *the same* physical state[*]. Consequently, at Section 2.3 we'll consider mean field Ansätze distinguished by gauge fluxes, and how a variational Monte Carlo is capable of selecting the most representative for the physical spin liquid state by comparing their respective ground state energies.

In an alternative scenario, more unbiased variational wave functions can be proposed via tensor and neural-network quantum states[90,91] - although to some extent they can still be related to Parton constructions.[92–94] Notwithstanding, projected wave functions within the variational Monte Carlo perspective continue to be suitable and relevant descriptions for QSLs, resonating valence bond (RVB) states, and even magnetic ordered phases. Additionally, their direct relation to the Parton constructions favors the interpretation of the physical theory describing these different states. A particular example of success within this context is the exactly solvable model of a Kitaev QSL which is represented by Majorana fermions.[95]

2.2.3 Metropolis-Hastings Algorithm and Quantum Variational Principle

The Variational Monte Carlo technique is a conjunction of the Quantum Variational principle and Monte Carlo methods to study mainly many-body correlated wave functions.[96,97] It is particularly interesting for extracting physical information such as the GSE, spin-spin correlations, and more recently, even low-energy dynamical features of spin-1/2 models such as the dynamical structure factor from a parton's perspective.[98,99]

---

[*] This scenario can be directly connected to the idea of including magnetic fields in lattice models via the *Peierls substitution*[89] and one may find the description of gauge fluxes as magnetic fluxes on the elementary plaquettes.

Exact solutions to quantum many-body problems are given by the resolution of the eigenvalue problem of the time-independent Schrödinger equation $H\left|\Psi\right\rangle = E\left|\Psi\right\rangle$. This task is practically unfeasible due to the exponential growth of the physical Hilbert space for the degrees of freedom of a particular system. An alternative approach is to consider relevant physical properties and symmetries that represent a class of trial wave functions (Ansätze) $\{\left|\Psi_{A_1}\right\rangle, \left|\Psi_{A_2}\right\rangle, \dots \left|\Psi_{A_n}\right\rangle\}$ and select the one with the lowest energy value correspondent to the ground state of the system. In the study of QSLs, for example, we will study wave functions constructed upon the Parton Construction Ansätze. This approach is validated by the quantum variational principle (or Rayleigh-Ritz method)[75] which can be formulated by expanding the trial wave functions on the basis of eigenstates $\left|\Psi_n\right\rangle$, while observing that its energy E_A must always be greater (or equal if the trial wave function is an exact eigenstate of H) than the ground state energy E_0:

$$E_A = \sum_n E_n \frac{\left|\left\langle \Psi_n | \Psi_A \right\rangle\right|^2}{\left\langle \Psi_A | \Psi_A \right\rangle} = E_0 + \sum_{n \neq 0} \left(E_n - E_0\right) \frac{\left|\left\langle \Psi_n | \Psi_A \right\rangle\right|^2}{\left\langle \Psi_A | \Psi_A \right\rangle} \geq E_0. \tag{2.45}$$

The definition of E_A can be obtained by considering a residual state $\left|\Phi_R\right\rangle = \left(H - E_A\right)\left|\Psi_A\right\rangle$, whose norm is different than zero if the trial wave function is not an exact eigenstate of H. By minimizing the norm with respect to E_A, the distance from the trial wave function $\left|\Psi_A\right\rangle$ to an exact eigenstate of H is reduced and we find from

$$\frac{\partial \left\langle \Phi_R | \Phi_R \right\rangle}{\partial E_A} = \frac{\partial}{\partial E_A} \Big(\left\langle \Psi_A | H^2 | \Psi_A \right\rangle - 2E_A \left\langle \Psi_A | H | \Psi_A \right\rangle + E_A^2 \left\langle \Psi_A | \Psi_A \right\rangle \Big) = 0 \tag{2.46}$$

that

$$E_A = \frac{\left\langle \Psi_A \left| H \right| \Psi_A \right\rangle}{\left\langle \Psi_A | \Psi_A \right\rangle}. \tag{2.47}$$

Obtaining a numerical evaluation of (2.47) is often challenging since for a generic operator $\mathcal{O}$ we need to evaluate it with respect to all possible configurations $\left|\alpha\right\rangle$ and $\left|\beta\right\rangle$ spanning the physical Hilbert space. In this context the expected value of this operators should be understood as

$$\left\langle \mathcal{O} \right\rangle = \frac{\left\langle \psi \left| \mathcal{O} \right| \psi \right\rangle}{\left\langle \psi | \psi \right\rangle} = \sum_{\alpha\beta} \left\langle \alpha \left| \mathcal{O} \right| \beta \right\rangle \frac{\left\langle \psi | \alpha \right\rangle \left\langle \beta | \psi \right\rangle}{\left\langle \psi | \psi \right\rangle}. \tag{2.48}$$

For a feasible computational calculation, we first rely on physical considerations based on the specific considered model, which drastically reduce the space the possible configurations is. If we are treating a Hubbard model at large U with half-filling condition, for example, we must assure that the hoppings of electrons obey the Pauli's Exclusion Principle.[100] Additionally, we can reinterpret equation (2.48) in

$$\left\langle \mathcal{O} \right\rangle = \sum_\alpha \left(\sum_\beta \left\langle \alpha \left| \mathcal{O} \right| \beta \right\rangle \frac{\left\langle \beta | \psi \right\rangle}{\left\langle \alpha | \psi \right\rangle} \right) \frac{\left|\left\langle \alpha | \psi \right\rangle\right|^2}{\left\langle \psi | \psi \right\rangle} = \sum_\alpha f\left(\alpha\right) p\left(\alpha\right), \tag{2.49}$$

as a statistical average of a local operator

$$f\left(\alpha\right) = \left(\sum_\beta \left\langle \alpha \left| \mathcal{O} \right| \beta \right\rangle \frac{\left\langle \beta | \psi \right\rangle}{\left\langle \alpha | \psi \right\rangle} \right) \tag{2.50}$$

over the probability distribution

$$p\left(\alpha\right)=\frac{\left|\langle\alpha|\psi\rangle\right|^{2}}{\langle\psi|\psi\rangle}\geq 0\quad\text{which obeys}\quad\sum_{\alpha}p\left(\alpha\right)=1. \tag{2.51}$$

These physical configurations are then generated via a MC Sampling,[101] upon which a MC weighting factor from going to a configuration α to another α' is given by the Metropolis-Hastings Algorithm[102, 103]

$$T\left(\alpha\rightarrow\alpha'\right)=\min\left[1,\frac{p\left(\alpha'\right)}{p\left(\alpha\right)}\right]=\begin{cases}\frac{p(\alpha')}{p(\alpha)} & ,\ \frac{p(\alpha')}{p(\alpha)}<1\\ 1 & ,\ \frac{p(\alpha')}{p(\alpha)}>1\end{cases}, \tag{2.52}$$

i.e., the new configuration is accepted in the second case if it is probabilistic more favorable - the energy of the new configuration is smaller. If this is not the case, the new configuration can still be accepted, and detailed balance is respected.[101]

We also note the convenience of this expression since the norm factors $\langle\psi|\psi\rangle$, which are computationally demanding - of order $\mathcal{O}\left(N^{3}\right)$ -, are canceled identically. The idea is then to have a random walk over all states in the configuration space of the physical model, where each state α has a statistical weight $p\left(\alpha\right)$ associated. This process generates a Markov Chain[101] of configurations which tends to an equilibrium statistical distribution after a sufficient time (known as *thermalization time*). Therefore, at each MC step we generate a new configuration of the system in order to form a sample $\{\alpha_1,\alpha_2,\ldots,\alpha_{N_{MC}}\}$ of configurations for N_{MC} steps. The expected value for an operator is then given by

$$\langle\mathcal{O}\rangle=\frac{1}{N_{MC}}\sum_{i=1}^{N_{MC}}f\left(\alpha_{i}\right). \tag{2.53}$$

Since the number of accessible states is not infinite in a practical situation, after the system has reached the equilibrium we can divide the MC steps into different bins N_b and calculate an average for each one of them. The estimator of the operator $\langle\mathcal{O}\rangle$ will then by given by

$$\langle\mathcal{O}\rangle=\frac{1}{N_{b}}\sum_{l=1}^{N_{b}}\langle\mathcal{O}\rangle_{l}, \tag{2.54}$$

with a statistical error determined by the standard deviation formula

$$\delta\mathcal{O}=\sqrt{\frac{1}{N_{b}-1}\sum_{l=1}^{N_{b}}\left(\langle\mathcal{O}\rangle-\langle\mathcal{O}\rangle_{l}\right)^{2}}. \tag{2.55}$$

As final remarks, we reinforce the result (2.47) to observe that the variational calculations are made based on an energy minimization procedure. In this manner, other observables obtained via this method may be less precise. Additionally, if one considers an exact eigenstate as a trial wave function, the variance related to the GSE observable at equation (2.54) will be close to zero, as we shall see on Appendix B when considering

Gutzwiller Projected wave functions for the Haldane-Shastry model, for example. Finally, we have not addressed the dependence of the trial wave functions on explicit variational parameters. Intuitively, these can be evaluated and determined on a classical parameter minimization problem - this approach is adopted in Chapter 4, for example. More importantly, this can be done automatically in the VMC algorithm by using the Stochastic Reconfiguration technique,[104,105] which is an important aspect that will be investigated in future work.

2.2.4 Gutzwiller Projected Wave Functions and Slater Determinant Ansätze

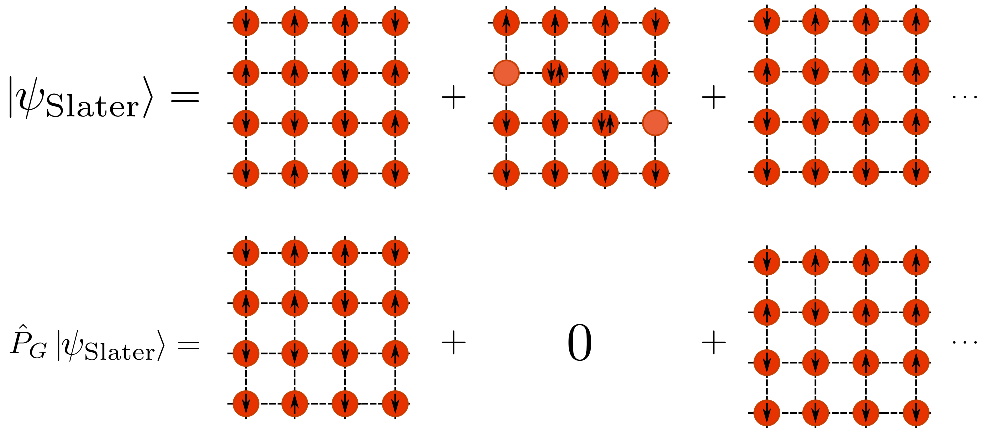
$|\psi_{\text{Slater}}\rangle =$
+
+
...
$\hat{P}_G\,|\psi_{\text{Slater}}\rangle =$
+
0
+
...

Figure 9 – Pictorial representation of the Gutzwiller projector (2.56) excluding states that do not obey the constraint in (2.21).
Source: By the author.

How do we effectively describe the trial wave functions? We are interested in answering this question in the context of strongly-correlated systems, and more specifically, for QSLs. We can get a first insight by using MFTs based on the Parton construction and later on imposing a physical condition over the states with the Gutzwiller projection operator[100,106] $\hat{P}_G$,

$$|\psi_T\rangle = \hat{\mathcal{P}}_G\,|\psi_{MFT}\rangle = \prod_i \left(n_{i\uparrow} - n_{i\downarrow}\right)^2 |\psi_{MFT}\rangle\,, \tag{2.56}$$

which in this case eliminates states from the enlarged Hilbert space that do not obey the no-double occupancy physical constraint (2.21)[*]. This projection is imposed exactly in the VMC by constructing the initial configuration with equal number of spins up and down. Our VMC dynamics exchanges opposite spins at arbitrary sites thus preserving the state with $n_i = 1$. In this context, the Variational Monte Carlo in conjunction with projected wave functions can describe physically motivated Ansätze for spin liquid states, valence bond solids, and even magnetic ordered phases (Subsection 2.2.5).

---

[*] Additionally, the enlargement of the Hilbert space brings gauge freedom for describing the variational states that represent spin liquids, as explained in Section 2.2.2 - see Fig. 9. A complete classification of all possible Ansätze describing QSLs which respects lattice symmetries (and additional symmetries present in the considered model - such as SU(2), for example) can be found within the Projective Symmetry Group (PSG)[11,25,107] approach.

A first numerical implementation of fermionic wave functions can be built from a filled Fermi sea with N spinons distributed equally in both spin flavors as

$$|\psi\rangle = \prod_{\sigma=\uparrow\downarrow} \prod_{k=1}^{N/2} f_{\boldsymbol{k}\sigma}^{\dagger} |0\rangle \, . \tag{2.57}$$

Since the spin number is conserved, this can be rewritten in real space as a product of Slater determinants of size $N/2 \times N/2$ as

$$\begin{gathered} \psi_{\boldsymbol{k}_1,\dots,\boldsymbol{k}_L}\left(\boldsymbol{x}_1,\dots,\boldsymbol{x}_L\right) = \det\psi\left(\boldsymbol{k},\boldsymbol{r}\right) = \det \mathbb{A}_{\alpha,\uparrow} \det \mathbb{A}_{\alpha,\downarrow} = \\ = \begin{vmatrix} \exp(i\boldsymbol{k}_1\boldsymbol{r}_{1,\uparrow}) & \dots & \exp\left(i\boldsymbol{k}_1\boldsymbol{r}_{\frac{N}{2},\uparrow}\right) \\ \vdots & \ddots & \vdots \\ \exp\left(i\boldsymbol{k}_{\frac{N}{2}}\boldsymbol{r}_{1,\uparrow}\right) & \dots & \exp\left(i\boldsymbol{k}_{\frac{N}{2}}\boldsymbol{r}_{\frac{N}{2},\uparrow}\right) \end{vmatrix} \begin{vmatrix} \exp(i\boldsymbol{k}_1\boldsymbol{r}_{1,\downarrow}) & \dots & \exp\left(i\boldsymbol{k}_1\boldsymbol{r}_{\frac{N}{2},\downarrow}\right) \\ \vdots & \ddots & \vdots \\ \exp\left(i\boldsymbol{k}_{\frac{N}{2}}\boldsymbol{r}_{1,\downarrow}\right) & \dots & \exp\left(i\boldsymbol{k}_{\frac{N}{2}}\boldsymbol{r}_{\frac{N}{2},\downarrow}\right) \end{vmatrix}, \end{gathered} \tag{2.58}$$

with each element of the matrix being analytically represented in a free-fermion form $\psi_\sigma\left(k_i, r_j\right) = \exp ik_i r_{j\sigma}$ for a spinon with spin σ, j-th position and i-th wavevector. We consider periodic, antiperiodic, or mixed boundary conditions for the mean-field theory. The latter, for example, have been shown to improve numerical convergence in previous studies.[5, 108, 109]

Different configurations α and β differ essentially by the interchange of two spinons with different σ, such that $\mathbb{A}_\alpha \neq \mathbb{A}_\beta$ by one column in our convention. This is essentially how the MC updates are performed in the numerical implementation. We then randomly place each spinon's spin flavor on $N/2$ sites of our lattice. The Monte Carlo moves consist of exchanging a random pair of sites containing distinct spin flavors. Exchanges with sites far away are also permitted - even though they would not be accessed directly via the Hamiltonian - to improve the sampling over the space of configurations. Therefore, the MC updates are implemented in the matrix of configurations via a transformation $\mathbb{A} \to \mathbb{A} + \boldsymbol{u}\boldsymbol{v}^T$, where:

- If $\boldsymbol{u} = \boldsymbol{e}_i \Rightarrow \mathbb{A} \to \mathbb{A} + \boldsymbol{e}_i\boldsymbol{v}^T$ (we add the components of $\boldsymbol{v}$ to the ith row);
- If $\boldsymbol{v} = \boldsymbol{e}_j \Rightarrow \mathbb{A} \to \mathbb{A} + \boldsymbol{u}\boldsymbol{e}_j$ (we add the components of $\boldsymbol{v}$ to the jth column);
- If $\boldsymbol{u} = \boldsymbol{e}_i$ and $\boldsymbol{v} = \boldsymbol{e}_j \Rightarrow \mathbb{A} \to \mathbb{A} + \boldsymbol{e}_i\boldsymbol{e}_j$ (we only add a term to the a_{ij} element of $\mathbb{A}$),

with $\boldsymbol{u} = \begin{pmatrix} u_1 \\ \vdots \\ u_n \end{pmatrix}$ and $\boldsymbol{v}^T = \begin{pmatrix} v_1 & \dots & v_n \end{pmatrix}$.

If we know the square matrix of configurations $\mathbb{A}$ and its inverse $\mathbb{A}^{-1}$, after the transformation described above, we can implement the Sherman-Morrison formula and the Matrix determinant Lemma to calculate

$$\left(\mathbb{A}+\boldsymbol{u}\boldsymbol{v}^{T}\right)^{-1}=\mathbb{B}^{-1}=\mathbb{A}^{-1}-\frac{\mathbb{A}^{-1}\boldsymbol{u}\boldsymbol{v}^{T}\mathbb{A}^{-1}}{1+\boldsymbol{v}^{T}\mathbb{A}^{-1}\boldsymbol{v}} \tag{2.59}$$

and the determinant

$$\det\left(\mathbb{A}+\boldsymbol{u}\boldsymbol{v}^{T}\right)=\det\mathbb{B}=\left(1+\boldsymbol{v}^{T}\mathbb{A}^{-1}\boldsymbol{u}\right)\det\mathbb{A} \tag{2.60}$$

more efficiently. The Sherman-Morrison formula demands operations of $\mathcal{O}\left(N^{2}\right)$ instead of calculating the determinant directly wich is of order $\mathcal{O}\left(N^{3}\right)$,[110] for example. The correspondent proofs for the Formula and Lemma can be found in the Appendix A.

Algorithm 3 Variational Monte Carlo

---

1. Start with a random configuration in $\mathbb{A}_{\alpha}$, with $n_{\uparrow}=n_{\downarrow}$ in random positions. Store both inverse matrices and save a backup of each initial configuration.

2. Select a new configuration by randomly exchanging the position of two opposite spins. If the new spin is in the k-th column

   $$\det\mathbb{A}_{\beta}=\left(1+e_{k}^{T}\mathbb{A}_{\alpha}^{-1}u_{k}\right)\det\mathbb{A}_{\alpha} \tag{2.61}$$

   and

   $$\mathbb{A}_{\beta}^{-1}=\mathbb{A}_{\alpha}^{-1}-\frac{\mathbb{A}_{\alpha}^{-1}u_{k}e_{k}^{T}\mathbb{A}_{\alpha}^{-1}}{1+e_{k}^{T}\mathbb{A}_{\alpha}^{-1}u_{k}}, \tag{2.62}$$

   with $u_{i}=\left[\mathbb{A}_{\beta}\right]_{ik}-\left[\mathbb{A}_{\alpha}\right]_{ik}$.

3. Accept or reject the new configuration by the Metropolis rule

   $$T\left(\alpha\rightarrow\beta\right)=\min\left[1,\frac{p\left(\beta\right)}{p\left(\alpha\right)}\right]=\begin{cases}\frac{p(\beta)}{p(\alpha)} & ,\ \frac{p(\beta)}{p(\alpha)}<1\\ 1 & ,\ \frac{p(\beta)}{p(\alpha)}\geq 1\end{cases}. \tag{2.63}$$

   where $\frac{p(\beta)}{p(\alpha)}=\frac{|\langle\beta|\psi\rangle|^{2}}{|\langle\alpha|\psi\rangle|^{2}}=\left|\frac{\det\mathbb{A}_{\beta}}{\det\mathbb{A}_{\alpha}}\right|^{2}=\left(1+u_{k}\mathbb{A}_{\alpha}^{-1}e_{k}^{T}\right)\left(1+u_{k}\mathbb{A}_{\alpha}^{-1}e_{k}^{T}\right)^{*}$. This equation only states a minimization of energy. To properly introduce a Metropolis Algorithm one should sort a random number $r\in[0,1]$: if $r<p\left(\beta\right)/p\left(\alpha\right)$ the new configuration can still be accepted. Otherwise, if $r\geq p\left(\beta\right)/p\left(\alpha\right)$, the old configuration is maintained.

4. Go back to step 2 and repeat the algorithm for the desired MC sweeps (one MC sweep is equivalent to N spin exchange attempts).

The pseudo-code for the first implementation of the VMC at Algorithm 3 describes the procedure to reach the equilibration time once the MC steps are completed. After equilibration, measurements of physical observables can be taken. Our interest will be mainly on the GSE of the system and the spin-spin correlations. We must be cautious with the order of operators since the configuration matrices are divided in a product of two submatrices for each spin. At equation (2.29), we consider then $f^\dagger_{i\uparrow}f_{i\downarrow}f^\dagger_{j\downarrow}f_{j\uparrow} = -f^\dagger_{i\uparrow}f_{j\uparrow}f^\dagger_{j\downarrow}f_{i\downarrow}$, for example. From equation (2.57) this means that we first fill $N/2$ states with spin up and then complete the remaining with down spins. The non-local contribution to the GSE comes from x-y components of S,

$$\langle \mathcal{H}_{NL} \rangle = \sum_\beta \langle \alpha \,|\mathcal{H}_{NL}|\, \beta\rangle \frac{\langle \beta|\psi\rangle}{\langle \alpha|\psi\rangle} = -\frac{1}{2}\sum_i\sum_\beta \frac{\det \mathbb{A}^{(i)}_\beta}{\det \mathbb{A}^{(i)}_\alpha}, \tag{2.64}$$

where

$$\mathcal{H}_{NL} = -\frac{1}{4}\sum_{<i,j>} J_{i,j}\left(f^\dagger_{i\uparrow}f_{j\uparrow}f^\dagger_{j\downarrow}f_{i\downarrow} + h.c.\right) \tag{2.65}$$

and $|\beta\rangle$ and $|\alpha\rangle = c^\dagger_{\boldsymbol{r}_1\uparrow}c^\dagger_{\boldsymbol{r}_2\uparrow}\dots c^\dagger_{\boldsymbol{r}_{N/2}\uparrow}c^\dagger_{\boldsymbol{r}_1\downarrow}c^\dagger_{\boldsymbol{r}_2\downarrow}\dots c^\dagger_{\boldsymbol{r}_{N/2}\downarrow}|0\rangle$ differ by the exchange $|\uparrow,\boldsymbol{r}_i\rangle \to |\downarrow,\boldsymbol{r}_j\rangle$ with j a next neighbor with opposite spin. Additionally, the local contributions for the GSE and spin-spin correlations comes both from the z-component of the Hamiltonian as

$$E_L = \frac{1}{4}\sum_{<i,j>}\left(n_{i\uparrow} - n_{i\downarrow}\right)\left(n_{j\uparrow} - n_{j\downarrow}\right), \tag{2.66}$$

and

$$\langle S^z_0 S^z_i\rangle = \langle\left(n_{0\uparrow} - n_{0\downarrow}\right)\left(n_{i\uparrow} - n_{i\downarrow}\right)\rangle = \frac{1}{4}\left(2n_{0\uparrow} - 1\right)\left(2n_{i\uparrow} - 1\right). \tag{2.67}$$

Another important benchmark for SU(2) symmetric models is to calculate the GSE from local contributions by observing that each statistical mean for x, y and z components contributes as

$$E = \frac{3}{4}\sum_{i,j}\left(2n_{i\uparrow} - 1\right)\left(2n_{j\uparrow} - 1\right). \tag{2.68}$$

This is not true if SU(2) is a broken symmetry at the ground state, as in the Ansätze based on SDW wave functions (Subsection 2.2.5), for example. It is also clear that this result is only exact at $N \to \infty$, therefore, numerical error increases as the system sizes are decreased.

2.2.5 SDW wave functions and ordered phases

It is possible to extend our projected wave functions to include a class of Ansätze responsible for allowing the investigation of the stability of QSLs towards ordered phases. This is achieved by constructing the Ansätze with the Hamiltonian

$$\mathcal{H}_{MFT} = \sum_{(i,j),\alpha} \chi_{ij} f^\dagger_{i\alpha} f_{j\alpha} + h\sum_i \boldsymbol{m}_i \cdot \boldsymbol{S}_i, \tag{2.69}$$

which includes the previously explored hoppings between Abrikosov fermions and an additional Zeeman field responsible for the investigation of the stability of the QSLs towards ordered phases.[111] The class of variational Ansätze generated in this formalism will enable us to consider the influence of the ordered phases on the CSL with the inclusion of quantum fluctuations in Chapter 4. The spatial periodicity of the magnetic field is fixed by $\boldsymbol{m}_i$, which may consist as a numerical output from classical minimization or direct parameterization of classical ordered phases. Additionally, the amplitude of the magnetic field is controlled by the parameter h.

The variational states are then obtained from a numerical diagonalization of the $2N \times 2N$ matrix for systems of size N. This procedure is done by first representing the diagonalized Hamiltonian (2.69) with the introduction of a unitary vector $|\boldsymbol{m}_i| = 1$, given by

$$\boldsymbol{h}_i = h\boldsymbol{m}_i = h\left(\frac{{m_i}^+ + {m^-}_i}{2}, \frac{{m_i}^+ - {m^-}_i}{2i}, m_i^z\right) \tag{2.70}$$

and the ladder operators

$$\begin{cases} m_i^+ \equiv m_i^x + im_i^y \\ m_i^- \equiv m_i^x - im_i^y \end{cases} \tag{2.71}$$

as

$$\begin{aligned} \mathcal{H}_{MFT} = -\frac{h}{2}\sum_i m_i^z \left(f_{i\uparrow}^\dagger f_{i\uparrow} - f_{i\downarrow}^\dagger f_{i\downarrow}\right) - \sum_{ij,\sigma} \chi_{ij} f_{i\sigma}^\dagger f_{j\sigma} + \\ -\frac{h}{2}\sum_i m_i^+ f_{i\downarrow}^\dagger f_{i\uparrow} + \frac{h}{2}\sum_i m_i^+ f_{i\downarrow}^\dagger f_{i\uparrow}. \end{aligned} \tag{2.72}$$

This can be further represented in a block diagonal form as

$$\mathcal{H}_{MFT} = \sum_{\boldsymbol{k}} \psi_{\boldsymbol{k}}^\dagger \mathbb{H} \psi_{\boldsymbol{k}} \tag{2.73}$$

with

$$\mathbb{H} = \begin{pmatrix} \mathbb{A}_{\uparrow\uparrow} & \mathbb{C}_{\uparrow\downarrow} \\ \mathbb{D}_{\downarrow\uparrow} & \mathbb{B}_{\downarrow\downarrow} \end{pmatrix},$$

$$\mathbb{A}_{\uparrow\uparrow} = \begin{pmatrix} -\frac{hm_i^z}{2} & -\chi_{12} & \cdots & \chi_{1N} \\ -\chi_{12}^* & -\frac{hm_2^z}{2} & \cdots & \vdots \\ \vdots & \vdots & \ddots & \vdots \\ -\chi_{1N}^* & \cdots & \cdots & -\frac{hm_N^z}{2} \end{pmatrix}, \qquad \mathbb{B}_{\downarrow\downarrow} = \begin{pmatrix} \frac{hm_i^z}{2} & -\chi_{12} & \cdots & \chi_{1N} \\ -\chi_{12}^* & \frac{hm_2^z}{2} & \cdots & \vdots \\ \vdots & \vdots & \ddots & \vdots \\ -\chi_{1N}^* & \cdots & \cdots & \frac{hm_N^z}{2} \end{pmatrix},$$

$$\mathbb{C}_{\uparrow\downarrow} = \begin{pmatrix} -\frac{hm_i^-}{2} & 0 & \cdots & 0 \\ 0 & -\frac{hm_2^-}{2} & \cdots & \vdots \\ \vdots & \vdots & \ddots & \vdots \\ 0 & \cdots & \cdots & -\frac{hm_N^-}{2} \end{pmatrix}, \text{ and } \quad \mathbb{D}_{\downarrow\uparrow} = \begin{pmatrix} -\frac{hm_i^+}{2} & 0 & \cdots & 0 \\ 0 & -\frac{hm_2^+}{2} & \cdots & \vdots \\ \vdots & \vdots & \ddots & \vdots \\ 0 & \cdots & \cdots & -\frac{hm_N^+}{2} \end{pmatrix}. \tag{2.74}$$

Because spin is no longer a good quantum number, after numerically diagonalizing $\mathbb{H}_{2N\times 2N}$, the eigenvectors chosen for the physical Ansätze will be given by the N eigenvectors with smallest eigenvalues from the spinor

$$\psi^\dagger = \begin{pmatrix} f_{1\uparrow}^\dagger & f_{2\uparrow}^\dagger & \ldots & f_{N\uparrow}^\dagger & f_{1\downarrow}^\dagger & f_{2\downarrow}^\dagger & \ldots & f_{N\downarrow}^\dagger \end{pmatrix}. \tag{2.75}$$

The numerical diagonalization can also be interpreted as the application of a unitary transformation U on the self-adjoint Hamiltonian H_{MFT},

$$\mathcal{H}_{SDW} = \Psi^{\dagger}\mathbb{W}\Psi \tag{2.76}$$

where

$$\mathbb{W} = \mathbb{U}^{\dagger}\mathbb{H}\mathbb{U}; \quad \mathbb{U}\mathbb{U}^{\dagger} = \mathbb{U}^{\dagger}\mathbb{U} = 1; \quad \Psi^{\dagger} = \psi^{\dagger}\mathbb{U}. \tag{2.77}$$

This unitary matrix is now doubled in size in comparison with our previous Ansätze used in the Subsection 2.2.4, and from its initial form

$$\mathbb{U}_{2N\times 2N} = \begin{pmatrix} \langle \boldsymbol{r}_1|\phi_1\rangle & \dots & \langle \boldsymbol{r}_1|\phi_{2N}\rangle \\ \vdots & \ddots & \vdots \\ \langle \boldsymbol{r}_{2N}|\phi_1\rangle & \dots & \langle \boldsymbol{r}_{2N}|\phi_{2N}\rangle \end{pmatrix} \tag{2.78}$$

the first N eigenfunctions can be chosen and subsequently divided in equal amounts of spin up and down in our final eigenfunction matrix. Subsequently, the Slater determinant ansatz for both fermionic spin flavors is given by

$$\Phi\left[\{\boldsymbol{r}_{j\alpha}\}\right] = \begin{vmatrix} \langle \boldsymbol{r}_{1\uparrow}|\phi_1\rangle & \dots & \langle \boldsymbol{r}_{1\uparrow}|\phi_N\rangle \\ \vdots & \ddots & \vdots \\ \langle \boldsymbol{r}_{\frac{N}{2}\uparrow}|\phi_N\rangle & \dots & \langle \boldsymbol{r}_{\frac{N}{2}\uparrow}|\phi_N\rangle \\ \langle \boldsymbol{r}_{1\downarrow}|\phi_1\rangle & \dots & \langle \boldsymbol{r}_{1\downarrow}|\phi_N\rangle \\ \vdots & \ddots & \vdots \\ \langle \boldsymbol{r}_{\frac{N}{2}\downarrow}|\phi_1\rangle & \dots & \langle \boldsymbol{r}_{\frac{N}{2}\downarrow}|\phi_N\rangle \end{vmatrix}. \tag{2.79}$$

Here, ϕ_j are the eigenstates of $\mathcal{H}_{MF}$ and they are projected at the spinon positions. Consequently, the usual hopping term of $f^{\dagger}_{i\sigma}f_{j\sigma}$ needs two row exchanges from the eigenfunction main matrix $\mathbb{W}$ to the original complete eigenfunction matrix $\mathbb{U}$, in order to preserve the conditions of equal number of spinons with spin up and down, and one spinon per site. The probability of each exchange in MC steps is then proportional to the weight

$$p_{\{\boldsymbol{r}_{j\alpha}\}} \propto \left|\Phi\left[\{\boldsymbol{r}_{j\alpha}\}\right]\right|^2 \tag{2.80}$$

of the wavefunction described by equation (2.79). Finally, the ground state wave function Ansätze are then given by the physical states

$$|\Psi_{phys}\rangle = \hat{\mathcal{P}}_G \sum_{i=1}^{N} \psi_i^{\dagger}|0\rangle = \hat{\mathcal{P}}_G |\Psi_{MFT}\rangle, \tag{2.81}$$

with $\hat{P}_g = \prod_i \left(n_{i\uparrow} - n_{i\downarrow}\right)^2$ being the usual Gutzwiller projection.

2.3 Numerical Benchmarks for AFM S=1/2 Heisenberg models

2.3.0.1 Spin Chain

We begin our numerical studies by considering the one-dimensional AFM S=1/2 spin chain described by the Heisenberg Hamiltonian. We employ the Variational Monte

Carlo in conjunction with the Parton Construction described in the previous Sections with a Gutzwiller Projected trial wave function (GPW). The exact result for the ground state energy $E_{exact}/(JN) = -0.443147$ is remarkably close to the one found for the GPW, $E_{GPW}/(JN) = -0.442118$, in the literature.[100] From Table 2, the energies found by the VMC code clearly converge to $E/(JN) \approx -0.4421$ as the number of spins N is increased, indicating that the main structure of the algorithm is reliable. The exact z component of

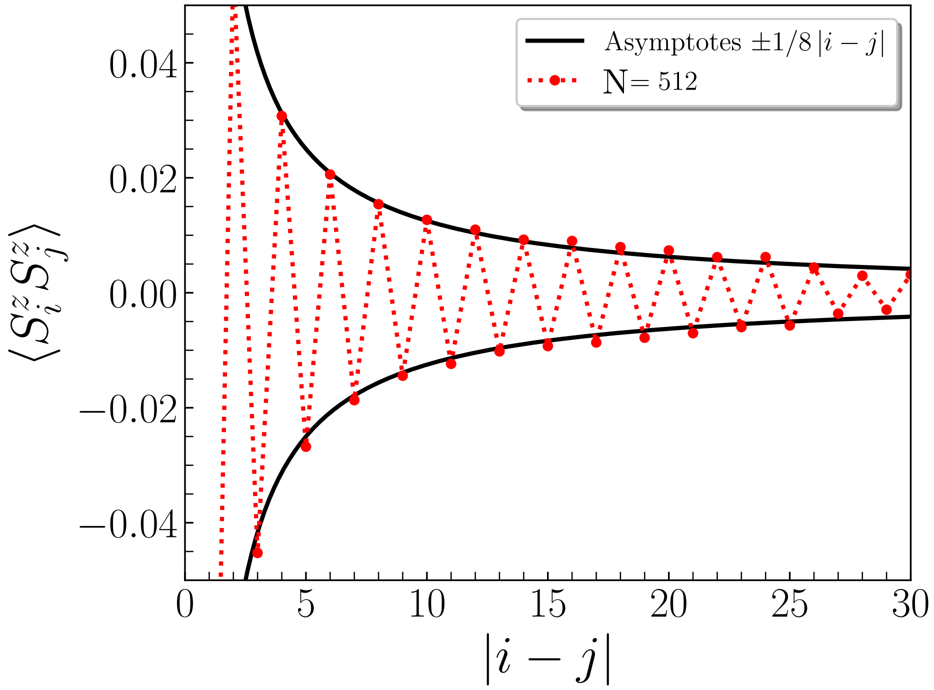

Figure 10 – Dependence of the zth component of spin-spin correlations with the distance between spins. The dashed black curves indicate the expected asymptotic value from equation (2.82). The red dots represent the data obtained for $N = 512$ in the VMC with a GPW ansatz. Errors bars are smaller than the markers.

Source: By the author.

the spin-spin correlations for the GPW decays algebraically as the asymptotic expression (2.40) for the Heisenberg model, is given by,[112]

$$\left\langle S_0^z S_j^z \right\rangle = \frac{\left\langle \psi_{GPW} \left| S_0^z S_j^z \right| \psi_{GPW} \right\rangle}{\langle \psi_{GPW} | \psi_{GPW} \rangle} = \frac{\mathrm{Si}\,(\pi j)}{4\pi} \frac{(-1)^j}{j}, \quad j > 0, \tag{2.82}$$

where $\mathrm{Si}\,(x) = \int_0^x dy \frac{\sin y}{y}$; the asymptotic expression of this expression for $n \gg 1$ is given by $\left\langle S_0^z S_j^z \right\rangle \simeq \left[\frac{(-1)^j}{8j}\right]$. It is important to remark that the exponent is now corrected in contrast with (2.39). A comparison with this exact result was done for different numbers of spins and the results for $N = 512$ are shown at Figure 10. Since the Variational Monte Carlo is based on a minimization of the GSE, the spin-spin correlations may take more time to converge accurately.

Table 2 – Ground state energy for the S=1/2 AFM spin chain using the GPW. The ground state energy was calculated for both non local + local energy terms (NL) and only local terms (L) by exploiting the SU(2) invariance of the model. The data was obtained with $2,0 \times 10^4$ MC sweeps discarded for thermalization, and $1,0 \times 10^5$ MC sweeps for average, divided into 100 bins. Numbers in parenthesis indicate the standard deviation with respect to the last digit.

N	E/JN $_{(NL)}$	E/JN $_{(L)}$
32	−0.44303 (5)	−0.4435 (4)
64	−0.44232 (5)	−0.4418 (4)
96	−0.44219 (5)	−0.4423 (3)
128	−0.44213 (5)	−0.4419 (3)
256	−0.44212 (5)	−0.4405 (3)
512	−0.44211 (4)	−0.4410 (3)

Source: By the author.

It is important to remark that more precise results for the observables can be achieved by increasing the number of spins, as well as the quantity of measurements averaged after complete thermalization in the Monte Carlo algorithm. This can be understood from Figure 11 since the data fluctuations diminish with an increasing chain length, whereas a single spin flip can be a considerable modification for the GSE for smaller lengths. In this context, the thermalization time also increases with the system size.

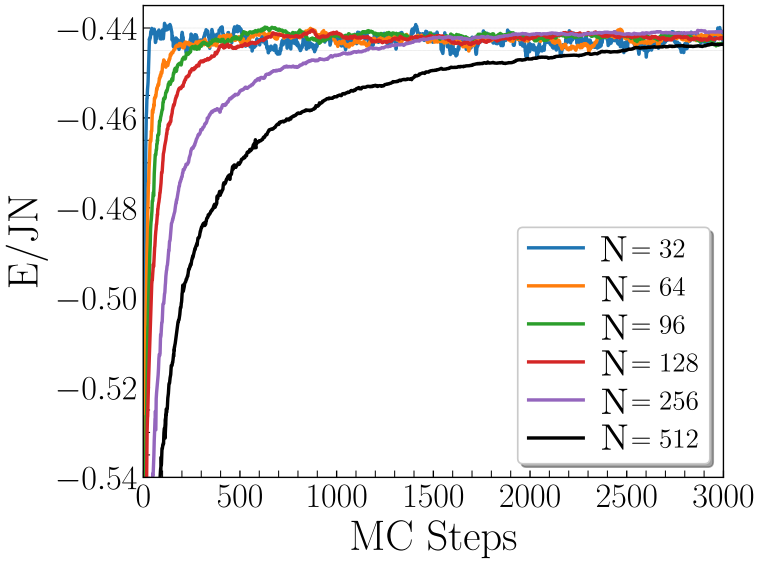

Figure 11 – Monte Carlo evolution of the GSE observable for the GPW as a function of MC steps for different system sizes. The data was obtained by an average of 50 different experiments (random seeds) for each system size. The MC Steps necessary for the convergence of the observable is understood as a thermalization time.

Source: By the author.

2.3.0.2 Kagome Lattice

The Kagome lattice presents itself as a paradigmatic case where frustrated magnetism can arise due to the corner-sharing triangles.[8,113] Novel phases appear due to this geometrical frustration, and we shall explore how some of them in this Subsection. Specifically, we study the $S = 1/2$ AFM Heisenberg model with next-neighbor couplings. There is good evidence that the ground state is described by a U(1) QSL.[4,8,16] The following results and discussions will be essential to the study of the CSL in Chapter 4.

- Tight-Binding Solution

A good starting point is solving the tight binding problem on the Kagome lattice, since the technical procedure is analogous for the MFT of the 0-Flux state spin liquid candidate. The position of each atom in the lattice is determined from equations (2.2), and the momentum vectors in the reciprocal lattice can be defined from equation (2.6). For this configuration, we employ a tight binding model with electron hoppings between first-neighbors such that there is only one orbital on each site via the Hamiltonian

$$\mathcal{H} = t \sum_{\langle i,j \rangle} \left\{ A_i^\dagger B_j + A_i^\dagger C_j + B_i^\dagger C_j + h.c. \right\}, \tag{2.83}$$

where $A_i^\dagger$ (A_i) represents a fermionic creation (destruction) operator of an electron in site i of the sublattice A (see Figure 4). The same reasoning applies to the operators $B_i^\dagger$ (B_i) and $C_i^\dagger$ (C_i) for electrons in the sublattices B and C. This can be further rewritten with the first-neighbor lattice vectors as

$$\begin{aligned} \mathcal{H} = t \sum_{\mathbf{r}_i} \Big\{ \Big(A_{\mathbf{r}_i}^\dagger B_{\mathbf{r}_i+\boldsymbol{\delta}_1} + A_{\mathbf{r}_i}^\dagger B_{\mathbf{r}_i-\boldsymbol{\delta}_1} \Big) + \Big(A_{\mathbf{r}_i}^\dagger C_{\mathbf{r}_i+\boldsymbol{\delta}_2} + \\ + A_{\mathbf{r}_i}^\dagger C_{\mathbf{r}_i-\boldsymbol{\delta}_2} \Big) + \Big(B_{\mathbf{r}_i}^\dagger C_{\mathbf{r}_i+\boldsymbol{\delta}_3} + B_{\mathbf{r}_i}^\dagger C_{\mathbf{r}_i-\boldsymbol{\delta}_3} \Big) + \text{h.c.} \Big\}. \end{aligned} \tag{2.84}$$

Due to Bloch's theorem, we can represent this Hamiltonian in the reciprocal space with the Fourier transforms of the physical operators such that

$$\begin{aligned} \mathcal{H} = t \sum_{\mathbf{k},\mathbf{k}'} \left(\frac{1}{N_s} \sum_j \exp i \left(\mathbf{k}' - \mathbf{k} \right) \cdot \mathbf{r}_j \right) \Big\{ \Big(A_{\mathbf{k}}^\dagger B_{\mathbf{k}'} + B_{\mathbf{k}}^\dagger A_{\mathbf{k}'} \Big) 2\cos\left(\mathbf{k} \cdot \boldsymbol{\delta}_1\right) + \\ + \Big(C_{\mathbf{k}}^\dagger A_{\mathbf{k}'} + A_{\mathbf{k}}^\dagger C_{\mathbf{k}'} \Big) 2\cos\left(\mathbf{k} \cdot \boldsymbol{\delta}_2\right) + \Big(B_{\mathbf{k}}^\dagger C_{\mathbf{k}'} + C_{\mathbf{k}}^\dagger B_{\mathbf{k}'} \Big) 2\cos\left(\mathbf{k} \cdot \boldsymbol{\delta}_3\right) \Big\}. \end{aligned} \tag{2.85}$$

The Hamiltonian can then be cast into a matrix form as

$$\mathcal{H} = t \sum_{\mathbf{k}} \begin{pmatrix} A_{\mathbf{k}}^\dagger & B_{\mathbf{k}}^\dagger & C_{\mathbf{k}}^\dagger \end{pmatrix} \begin{pmatrix} 0 & 2\cos(\kappa_1) & 2\cos(\kappa_2) \\ 2\cos(\kappa_1) & 0 & 2\cos(\kappa_3) \\ 2\cos(\kappa_2) & 2\cos(\kappa_3) & 0 \end{pmatrix} \begin{pmatrix} A_{\mathbf{k}} \\ B_{\mathbf{k}} \\ C_{\mathbf{k}} \end{pmatrix} = \sum_{\mathbf{k}} \psi_{\mathbf{k}}^\dagger \mathbb{H} \psi_{\mathbf{k}}, \tag{2.86}$$

where $\kappa_j = \mathbf{k} \cdot \boldsymbol{\delta}_j$ for $j = 1, 2, 3$, and the characteristic polynomial $\det(\lambda \mathbb{I} - \mathbb{H}) = \lambda^3 - 2t_1t_2t_3 - \left(t_1^2 + t_2^2 + t_3^2\right)\lambda$ is determined with $t_j = 2t\cos\kappa_j$. Using $\Lambda(\mathbf{k}) = \cos \mathbf{k} \cdot \mathbf{a}_1 +$

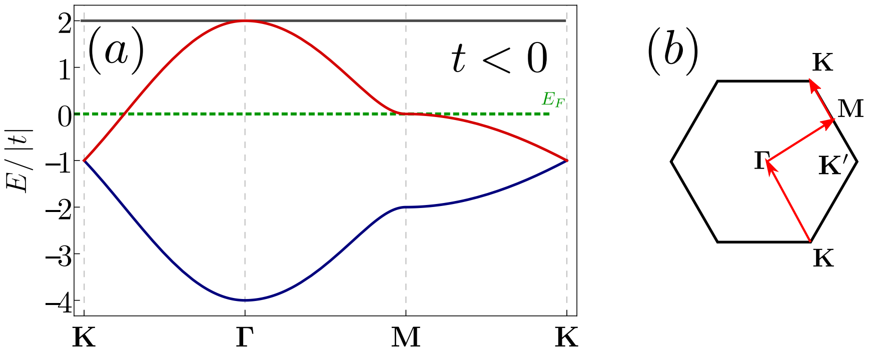

Figure 12 – Electronic band structure for the Kagome Lattice with and negative hopping parameters t (a). The Fermi energy level $E_f = 0$ is indicated with the green dashed lines. The corresponding path along high-symmetry lines of the BZ is also presented (b).
Source: By the author.

$\cos \mathbf{k}\cdot\mathbf{a}_2 + \cos \mathbf{k}\cdot\mathbf{a}_3$ and the relations

$$\begin{cases} \prod_{i=1}^{3} t_i = 2t^3\left(1+\Lambda\left(\mathbf{k}\right)\right) \\ \sum_{i=1}^{3} t_i^2 = 2t^2\left(3+\Lambda\left(\mathbf{k}\right)\right) \end{cases}, \tag{2.87}$$

the characteristic polynomial can be cast into a more convenient form of $P\left(\lambda\right) = \left(\lambda+2t\right)\left[\left(\lambda-t\right)^2 - t^2\left(3+2\Lambda\left(\mathbf{k}\right)\right)\right]$. Consequently, the energy spectrum can be finally obtained as being composed by two dispersive bands and one special flat band

$$\begin{cases} E_{\pm}\left(\mathbf{k}\right) = t\left(1 \pm \sqrt{3+2\Lambda\left(\mathbf{k}\right)}\right) \\ E_{\text{flat}} = -2t \end{cases}. \tag{2.88}$$

The dependence of the energy spectrum on special points of the reciprocal lattice can be seen at Figure 12, where the Dirac nodes are evident at points K and K'. The flat band at $E=-2t$ - responsible for a massive degeneracy on the energy spectrum - is unstable with respect to longer range hoppings.[113] Nevertheless, this massive degeneracy is still representative to the difficult task of finding the true ground state in effective models for this geometrical configuration,[8] and some reminiscences may be present on MFTs for QSLs as we shall see in the following discussion.

- 0−Flux ansatz

As in the Square Lattice MFT solution for QSLs, the $0-$ Flux state is related to the Tight-binding Solution as well on the Kagome Lattice. Following the equation (2.32) and the correspondence of $t \to -J\chi$, the energy spectrum can be determined naturally from (2.88) as

$$\begin{cases} E^0_{\pm}\left(\mathbf{k}\right) = -J\chi\left(1 \pm \sqrt{3+2\Lambda\left(\mathbf{k}\right)}\right) \\ E^0_{\text{flat}} = +2J\chi \end{cases}. \tag{2.89}$$

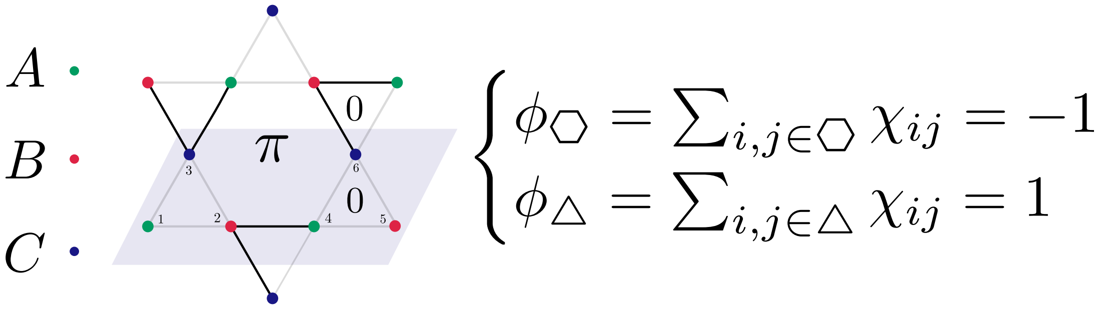
A
B
C
π
0
0
1
2
3
4
5
6
$\begin{cases}\phi_{\hexagon} = \sum_{i,j\in\hexagon}\chi_{ij} = -1\\ \phi_{\triangle} = \sum_{i,j\in\triangle}\chi_{ij} = 1\end{cases}$

Figure 13 – Six-site unit-cell configuration for the $\pi-$Flux ansatz for the Heisenberg model on the Kagome lattice. The π flux is imposed on the elementary hexagons and the 0 Flux on triangles. The solid black lines represent $\chi_{ij} = -1$ and the gray lines $\chi_{ij} = 1$. From the doubled unit cell (blue parallelogram) $\mathbf{a}_1 \rightarrow 2\mathbf{a}_1$.
Source: By the author.

- π – Flux ansatz

In the case of the π – Flux ansatz we have a more intricate situation. This flux is understood as being contained on the hexagons of a new doubled unit cell while being absent on the triangles (Figure 13). Therefore, all χ_{ij} at equation (2.32) have the same magnitude and the expression can be adapted as

$$\begin{aligned}\mathcal{H}_{MF} = -\frac{J\chi}{2}\sum_{\boldsymbol{r},\sigma}\Big[&f^\dagger_{\boldsymbol{r},\sigma}f_{\boldsymbol{r}\pm\mathbf{a_2},\sigma} + f^\dagger_{\boldsymbol{r}\pm\mathbf{a_2},\sigma}f_{\boldsymbol{r},\sigma} + f^\dagger_{\boldsymbol{r},\sigma}f_{\boldsymbol{r}\pm\mathbf{a_1},\sigma} + \\ &+f^\dagger_{\boldsymbol{r}\pm\mathbf{a_1},\sigma}f_{\boldsymbol{r},\sigma} + f^\dagger_{\boldsymbol{r},\sigma}f_{\boldsymbol{r}\pm\mathbf{a_3},\sigma} + f^\dagger_{\boldsymbol{r}\pm\mathbf{a_3},\sigma}f_{\boldsymbol{r},\sigma}\Big].\end{aligned} \tag{2.90}$$

This Hamiltonian, which is divided into contributions for each sub-lattice A,B and C, can be diagonalized by doubling the unit cell to accommodate the gauge flux patterns. For this, we consider the position of each atom in the six-site unit-cell (Figure 13) as being given by $\mathbf{R} = 2n_1\mathbf{a}_1 + n_2\mathbf{a}_2$ for n_1 and n_2 integers. The Hamiltonian can then be rewritten with this new notation as

$$\begin{aligned}\mathcal{H}_{MF} = -\frac{J\chi}{2}{\sum}'_{\boldsymbol{R},\sigma}\Big[&f^\dagger_{\boldsymbol{R},\sigma,1}\left(f_{\boldsymbol{R},\sigma,2} + f_{\boldsymbol{R},\sigma,3}\right) + f^\dagger_{\boldsymbol{R},\sigma,2}\left(f_{\boldsymbol{R},\sigma,3} - f_{\boldsymbol{R},\sigma,4}\right) + \\ &+f^\dagger_{\boldsymbol{R},\sigma,3}\left(-f_{\boldsymbol{R}+\mathbf{a}_2,\sigma,1} - f_{\boldsymbol{R}+\mathbf{a}_3,\sigma,5}\right) + f^\dagger_{\boldsymbol{R},\sigma,4}\left(f_{\boldsymbol{R},\sigma,5} + f_{\boldsymbol{R}+\mathbf{a_1},\sigma,6}\right) + \\ &+f^\dagger_{\boldsymbol{R},\sigma,5}\left(f_{\boldsymbol{R},\sigma,6} + f_{\boldsymbol{R}+\mathbf{a}_1,\sigma,1}\right) + f^\dagger_{\boldsymbol{R},\sigma,6}\left(f_{\boldsymbol{R}+\mathbf{a_2},\sigma,4} - f_{\boldsymbol{R}+\mathbf{a_2},\sigma,2}\right) + \text{h.c.}\Big],\end{aligned} \tag{2.91}$$

noticing that the Hermitian conjugated terms also change the sign of $\mathbf{r} \pm \mathbf{a}_i \rightarrow \mathbf{r} \mp \mathbf{a}_i$, with the prime symbol indicating that the unit cell is now doubled in the horizontal direction. In the momentum space this Hamiltonian can be understood as

$$\mathcal{H}_{MF} = -\frac{J\chi}{2}\sum \mathbb{F}^\dagger \mathbb{M}\mathbb{F}, \tag{2.92}$$

with

$$-\mathbb{M} = \begin{pmatrix} 0 & 1 & (1-K_2^*) & 0 & K_1^* & 0 \\ 1 & 0 & 1 & -1 & 0 & -K_2^* \\ (1-K_2) & 1 & 0 & 0 & -K_1^*K_2 & 0 \\ 0 & -1 & 0 & 0 & 1 & (1+K_2^*) \\ K_1 & 0 & -K_1K_2^* & 1 & 0 & 1 \\ 0 & -K_2 & 0 & (1+K_2) & 1 & 0 \end{pmatrix}, \mathbb{F} = \begin{pmatrix} f_{\boldsymbol{k},\sigma,1} \\ f_{\boldsymbol{k},\sigma,2} \\ f_{\boldsymbol{k},\sigma,3} \\ f_{\boldsymbol{k},\sigma,4} \\ f_{\boldsymbol{k},\sigma,5} \\ f_{\boldsymbol{k},\sigma,6} \end{pmatrix}, \quad (2.93)$$

$K_1 = \exp(2i\mathbf{k} \cdot \mathbf{a}_1)$ and $K_2 = \exp(i\mathbf{k} \cdot \mathbf{a}_2)$. Importantly, enlarging the mean-field unit-cell does not break the translation symmetry of the lattice after the Gutzwiller projection. This is because the fluxes are gauged out thus preserving all symmetries of the problem as it is necessary in a true spin liquid state [(2.41)-(2.44)].

The diagonalized numerical spectrum obtained has two degenerate flat bands $+2t$ reminiscent of the tight-binding solution (Figure 12), and the other branches meet at the Dirac points $\pm\mathbf{K}_D = \left(0, \frac{\pi}{\sqrt{3}a}\right)$. The Fermi energy in this case is given by $E_F = t\left(\sqrt{3} - 1\right)$ - see Figure 14. Additionally, the presence of particle-hole symmetry and Dirac cones in the spectrum are distinctive characteristics of this ansatz. The diagonalization problem was solved with the "hopping parameter" $J\chi > 0$, although it can be shown that there is no physical distinction for the $J\chi < 0$ case even in the effective theory for low-energy excitations near the Dirac points.[5]

- VMC results for U(1) Dirac spin liquids

The possibility of the Kagome Lattice geometry to host a spin liquid state is better exemplified in the context of the mineral herbertsmithite, $\mathrm{ZnCu_3(OH)_6Cl_2}$. Both experimental[16] and theoretical work[8, 114] have found evidence that supports the proposal of a gapless U(1) Dirac spin liquid state description for the ground state of this material. Specifically, a previous Variational Monte Carlo study[4] found the ground state energies of $E^0 \approx -0.4121$ and $E^\pi \approx -0.42863$ for the 0 and π flux states, respectively,[8] in a $N = 12 \times 12 \times 3$ lattice using the GPW. They have also found that the specific $\pi -$ Flux ansatz has the best variational energy and that it is also locally stable against small perturbations, such that a transition to valence bond solid ordering or other chiral spin-liquid states proposed before[115] are not energetically favorable. These results were remarkably close to previous estimates from other methods such as exact diagonalization, with $E/J = -0.43$, and further numerical results suggested that indeed the U(1)-Dirac spin liquid state is a good candidate for describing the low-energy physics of the mineral herbertsmithite.[8, 62, 116]

In this context, we have implemented a VMC study of the AFM Heisenberg model with first-neighbors on the Kagome Lattice, with a GPW representing the 0 and π flux states presented in the previous MFT discussion. From Table 3 it can be seen that the

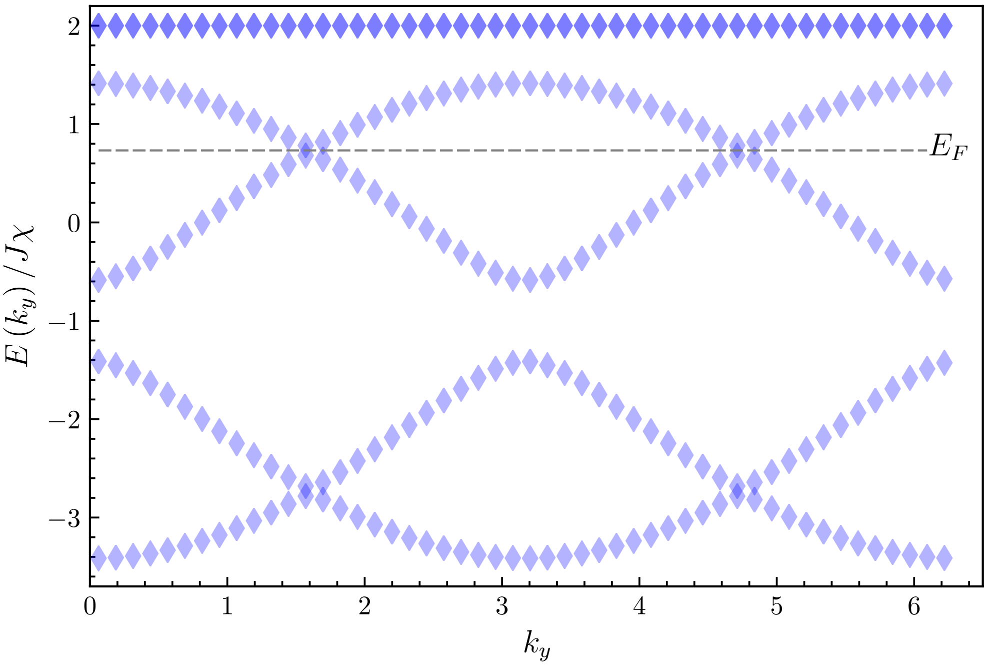

Figure 14 – Electronic band structure for the U(1)-Dirac state for $J\chi > 0$, $k_x = 0$ and $k_y \in [0, 6]$ in a $N = 50 \times 50 \times 3$ Kagome lattice. The intersection points with the Fermi energy $E_F/J\chi = \sqrt{3} - 1$ are given by $\mathbf{k}_1 = \left(0, \frac{\pi}{\sqrt{3}}\right)$ and $\mathbf{k}_2 = \left(0, \pi\sqrt{3}\right)$. The flat band is doubly degenerate while the remaining four are nondegenerate.

Source: By the author.

GSEs converge to the values of $E^{\pi} = -0.428$ and $E^{0} \approx -0.412$, which are in agreement with the previously mentioned works up to the numerical precision of our implementation of the VMC. The studies were performed with a lattice of size $L^2 = L \times L \times 3$ with 3 atoms per unit cell. For the $0-$Flux ansatz the algorithm can get stuck in local energy minima that do not correspond to the GSE expected values. This may occur due to the massive degeneracy that arises from filling the nodal states (the ones located at the Fermi Energy - see Figure 14) in the mean-field Hamiltonian if they are present in the initial trial wave function.[5] Different numerical experiments should be performed in this situation. There are four possibilities for the lattice boundary conditions: open (OBC), antiperiodic (APBC), periodic (PBC), and mixed (MBC), with the latter being an implementation of periodic boundary conditions on the x direction and anti-periodic on the y direction (or vice-versa). These are the only boundary conditions that do not introduce spurious fluxes. The MBC has been reported to lift the degeneracy of the mean-field ground state for different VMC studies[5] and, consequently, they offer a better convergence for the algorithm.[108,109] From a technical point of view, it should be noted that APBC introduce undesired global π fluxes which slow the convergence of the algorithm.[5] Therefore, we considered only MBC for the VMC studies of these Ansätze.

Table 3 – Ground state energy for the Heisenberg AFM model in a Kagome lattice using the GPW for the 0 (a) and π (b) flux Ansätze using PBC. The results for MBC were also consistent with the expected result. The data was obtained with $2,0 \times 10^5$ MC sweeps discarded for thermalization, and $1,0 \times 10^5$ MC sweeps for average, divided into 100 bins.

$N = 3 \times L^2$	$E/JL^2{}_{(NL)}$	$E/JL^2{}_{(L)}$
48	$-0.4108\,(1)$	$-0.4109\,(2)$
108	$-0.4128\,(2)$	$-0.4125\,(4)$
192	$-0.4120\,(2)$	$-0.4118\,(3)$

(a) 0 – Flux ansatz.

$N = 3 \times L^2$	$E/JL^2{}_{(NL)}$	$E/JL^2{}_{(L)}$
48	$-0.4215\,(3)$	$-0.4214\,(6)$
192	$-0.4274\,(2)$	$-0.4276\,(4)$
432	$-0.4283\,(1)$	$-0.4285\,(4)$

(b) π – Flux ansatz.

Source: By the author.

- VMC Results for chiral Ansätze

Two additional MFT chiral Ansätze were studied within our VMC implementation for the Heisenberg model on the Kagome Lattice. These consisted on a flux of $\theta = \pi/2$ on up triangles as well as its staggered version of $+(-)\pi/2$ on up (down) triangles (Figure 15). The results presented in Table 4 agree with the published values $E^{[\pm\pi/2,0]} \approx -0.3910\,(1)$ and $E^{[\pi/2,0]} \approx -0.4010\,(1)$.[4,5]

Table 4 – GSE for a GPW representing the chiral spin liquid candidates $SL - \left[\pm\frac{\pi}{2}, 0\right]$ (a) $SL - \left[\frac{\pi}{2}, 0\right]$ (b) using MBC. The data was obtained with $2,0 \times 10^5$ MC sweeps discarded for thermalization, and $2,0 \times 10^5$ MC sweeps for average, divided into 100 bins.

$N = 3 \times L^2$	$E/JL^2{}_{(NL)}$	$E/JL^2{}_{(L)}$
48	$-0.3921\,(2)$	$-0.3923\,(2)$
192	$-0.3910\,(4)$	$-0.3911\,(2)$
432	$-0.3912\,(3)$	$-0.3912\,(1)$

(a) QSL – $[\pm\pi/2, 0]$ ansatz.

$N = 3 \times L^2$	$E/JL^2{}_{(NL)}$	$E/JL^2{}_{(L)}$
48	$-0.4010\,(3)$	$-0.4007\,(3)$
192	$-0.4010\,(4)$	$-0.4009\,(2)$
432	$-0.4011\,(3)$	$-0.4012\,(2)$

(b) QSL – $[\pi/2, 0]$ ansatz.

Source: By the author.

- Chirality implementation

Inspired from the work of Kalmeyer and Laughlin in 1987,[26] a mechanism to introduce uniform chiral spin liquids in the absence of external magnetic fields was explored on the kagome lattice recently.[29,42] This state breaks both mirror and time-reversal symmetry explicitly while preserving the $SU\,(2)$ symmetry. It can be introduced by adding to the physical Hamiltonian the expectation value of the scalar spin chirality $J_\chi \hat{\chi}_{ijk} = J_\chi S_i \cdot (S_j \times S_k)$, with J_χ being responsible for establishing a uniform or staggered

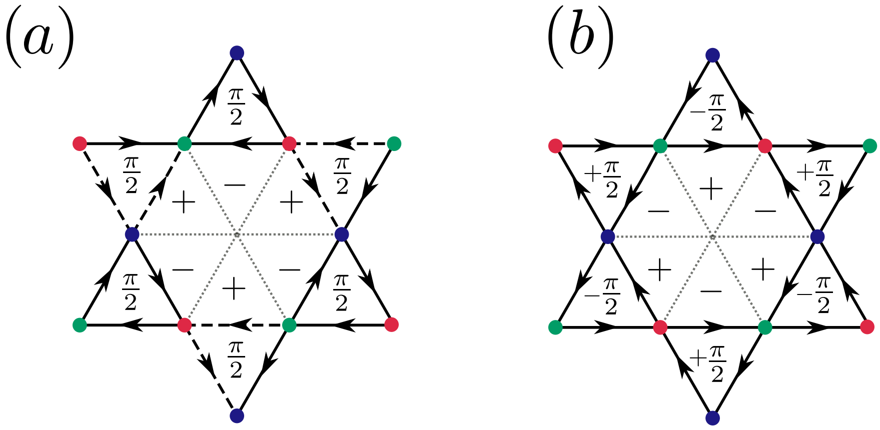

Figure 15 – Pictorial representation of gauge fluxes passing through the triangles to reproduce the Ansätze SL-$\left[\frac{\pi}{2},0\right]$ and SL-$\left[\pm\frac{\pi}{2},0\right]$, respectively.[4,5] (a) For the uniform chiral ansatz SL-$\left[\frac{\pi}{2},0\right]$, it is necessary to consider a doubled unit cell. This is done by imposing $\chi_{ij}=(+)-i$ for bonds on (anti)clockwise direction. The signals inside the hexagons illustrate that the overall flux is zero. One can interpret the dashed bonds as defect antiflux tubes passing through the triangles, maintaining the chiral phase invariant while canceling the background flux on the hexagons.[6] (b) The staggered chiral ansatz SL-$\left[\pm\frac{\pi}{2},0\right]$ can be implemented by imposing the same convention for χ_{ij}. The arrow directions provide the hopping orientation.

Source: By the author.

CSL. Therefore, a necessary condition for the appearance of a CSL is the absence of long-range magnetic order and an explicit nonzero expectation value of the chirality interaction $\langle\chi_{ijk}\rangle$.[117] As discussed in the Introduction, the numerical implementation of the chirality is a fundamental block for our comprehension of the CSL proposed recently.[12] Therefore, in this subsection, we discuss important aspects of how to implement chirality within our VMC.

The chiral interaction term is based on

$$E_{123}=\mathbf{S}_1\left(\mathbf{r}_i\right)\cdot\left[\mathbf{S}_2\left(\mathbf{r}_j\right)\times\mathbf{S}_3\left(\mathbf{r}_k\right)\right]=\frac{i}{4}\left[f_3^\dagger\left(\mathbf{r}_k\right)f_1\left(\mathbf{r}_i\right)f_1^\dagger\left(\mathbf{r}_i\right)f_2\left(\mathbf{r}_j\right)f_2^\dagger\left(\mathbf{r}_j\right)f_3\left(\mathbf{r}_k\right)-\text{h.c.}\right] \tag{2.94}$$

and can be rewritten in a convenient form for the VMC using number operators as

$$\begin{aligned}E_\chi^{NL}=\frac{i}{4}&\left[f_{2\uparrow}^\dagger f_{3\uparrow}f_{3\downarrow}^\dagger f_{2\downarrow}\left(n_{1\downarrow}-n_{1\uparrow}\right)+f_{3\uparrow}^\dagger f_{2\uparrow}f_{2\downarrow}^\dagger f_{3\downarrow}\left(n_{1\uparrow}-n_{1\downarrow}\right)\right]+\\&+\left[f_{3\uparrow}^\dagger f_{1\uparrow}f_{1\downarrow}^\dagger f_{3\downarrow}\left(n_{2\downarrow}-n_{2\uparrow}\right)+f_{1\uparrow}^\dagger f_{3\uparrow}f_{3\downarrow}^\dagger f_{1\downarrow}\left(n_{2\uparrow}-n_{2\downarrow}\right)\right]+\\&+\left[f_{1\uparrow}^\dagger f_{2\uparrow}f_{2\downarrow}^\dagger f_{1\downarrow}\left(n_{3\downarrow}-n_{3\uparrow}\right)+f_{2\uparrow}^\dagger f_{1\uparrow}f_{1\downarrow}^\dagger f_{2\downarrow}\left(n_{3\uparrow}-n_{3\downarrow}\right)\right].\end{aligned} \tag{2.95}$$

Additionally, this can also be cast in a more concise shape using the Levi-Civita symbol ε_{ijk}:

$$E_\chi^{NL}=\frac{i}{4}\sum_{i\neq j\neq k}^{3}\varepsilon_{ijk}f_{i\uparrow}^\dagger f_{j\uparrow}f_{j\downarrow}^\dagger f_{i\downarrow}\left(n_{k\downarrow}-n_{k\uparrow}\right). \tag{2.96}$$

Due to the permutation nature of the chirality relation (2.94), we can have a direct diagrammatic representation of each energy exchange for all possible non-trivial spin configurations (these are shown in Table 5 and further details can be found in the Appendix D).

The numerical subroutine to calculate the chiral energy (after the thermalization time) is based on selecting the current spin configuration in an elementary triangle, and then choosing the correspondent virtual exchanges.[118] This can be implemented with conditional cases labeled by the index of spins in the considered triangle (first column in Table 5). The process is then repeated for all triangles on the lattice.

Table 5 – Correspondence between the spin configuration and possible virtual exchanges for the chiral interaction (diagrams and analytical form). Labels are related with the spin in our VMC: 0 for ↓ and 1 for ↑.

Label	Initial Configuration	Final Configuration	Fermionic Representation
010	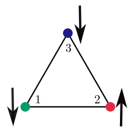	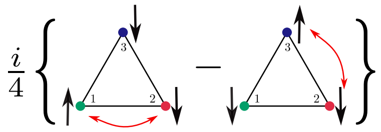	$\frac{i}{4}\left\{f^\dagger_{1\uparrow}f_{2\uparrow}f^\dagger_{2\downarrow}f_{1\downarrow}n_{3\downarrow}+\right.$ $\left.-f^\dagger_{3\uparrow}f_{2\uparrow}f^\dagger_{2\downarrow}f_{3\downarrow}n_{1\downarrow}\right\}$
001	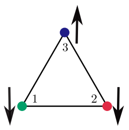	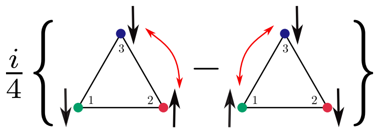	$\frac{i}{4}\left\{f^\dagger_{2\uparrow}f_{3\uparrow}f^\dagger_{3\downarrow}f_{2\downarrow}n_{1\downarrow}+\right.$ $\left.-f^\dagger_{1\uparrow}f_{3\uparrow}f^\dagger_{3\downarrow}f_{1\downarrow}n_{2\downarrow}\right\}$
100	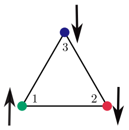	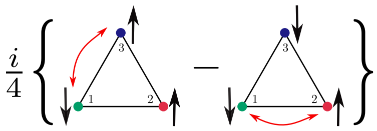	$\frac{i}{4}\left\{f^\dagger_{3\uparrow}f_{1\uparrow}f^\dagger_{1\downarrow}f_{3\downarrow}n_{2\downarrow}+\right.$ $\left.-f^\dagger_{2\uparrow}f_{1\uparrow}f^\dagger_{1\downarrow}f_{2\downarrow}n_{3\downarrow}\right\}$
101	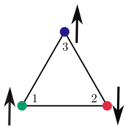	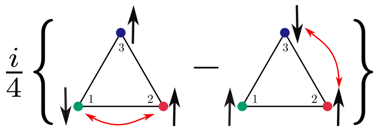	$\frac{i}{4}\left\{f^\dagger_{2\uparrow}f_{1\uparrow}f^\dagger_{1\downarrow}f_{2\downarrow}n_{3\uparrow}+\right.$ $\left.-f^\dagger_{2\uparrow}f_{3\uparrow}f^\dagger_{3\downarrow}f_{2\downarrow}n_{1\uparrow}\right\}$
110	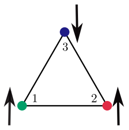	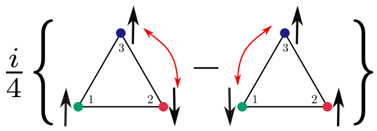	$\frac{i}{4}\left\{f^\dagger_{3\uparrow}f_{2\uparrow}f^\dagger_{2\downarrow}f_{3\downarrow}n_{1\uparrow}+\right.$ $\left.-f^\dagger_{3\uparrow}f_{1\uparrow}f^\dagger_{1\downarrow}f_{3\downarrow}n_{2\uparrow}\right\}$
011	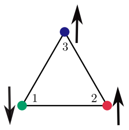	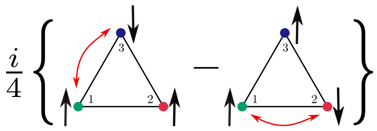	$\frac{i}{4}\left\{f^\dagger_{1\uparrow}f_{3\uparrow}f^\dagger_{3\downarrow}f_{1\downarrow}n_{2\uparrow}+\right.$ $\left.-f^\dagger_{1\uparrow}f_{2\uparrow}f^\dagger_{2\downarrow}f_{1\downarrow}n_{3\uparrow}\right\}$

Source: By the author.

To test our chirality implementation, we reconsider both the uniform and staggered chiral spin liquid Ansätze*. The expected value of the chirality per triangle is presented in Table 6. For both cases we considered MBC to have a proper degeneracy lifting. As the system size is increased, the imaginary part of the chirality tends to zero (up to the precision of our implementation of the algorithm) and its real part agrees with the previous result from Wietek *et al*, 2015[48] of $\langle \mathbf{S}_i \cdot (\mathbf{S}_j \times \mathbf{S}_k) \rangle_{i,j,k \in \triangle\triangledown} = \pm 0.0687\,(2)$ per spin.[48]

Table 6 – Chirality energy contribution for different lattice sizes, within the GPW representation for the spin liquid candidate $SL - \left[\frac{\pi}{2}, 0\right]$ with uniform $\pi/2$ flux through the triangles and zero background flux on the hexagons. The energy was obtained with $2,0 \times 10^5$ MC sweeps discarded for thermalization, and $2,0 \times 10^5$ MC sweeps for average, divided into 100 bins.

	$4 \times 4 \times 3$	$8 \times 8 \times 3$	$12 \times 12 \times 3$
$\mathrm{Re}\,(\langle \mathbf{S}_i \cdot (\mathbf{S}_j \times \mathbf{S}_k) \rangle)$	$0.0688\,(2)$	$0.0687\,(1)$	$0.0687\,(1)$
$\mathrm{Im}\,(\langle \mathbf{S}_i \cdot (\mathbf{S}_j \times \mathbf{S}_k) \rangle)$	$-0.0034\,(1)$	$-0.0008\,(1)$	$-0.0000\,(1)$

Source: By the author.

---

[*] It must be noted that the staggered chiral ansatz can be implement by using different hopping distributions. For example, one could alternatively consider the gauge where only the horizontal links are imaginary (all pointing to the left or right).[6] The important aspect is to maintain the appropriate chiral fluxes on the triangles while assuring that there are no background fluxes on the hexagons. This second task can be accomplished by directly imposing the background fluxes with next-nearest neighbor interactions on the Heisenberg model,[47] or by considering a pure chiral interaction[29] as the one in equation (2.94). Both these approaches were observed to reproduce the same chiral spin liquid phase.[48]

3 NONCOPLANAR MAGNETIC ORDERS IN THE KAGOME LATTICE

In this chapter, we investigate the classical phase diagram of the modified Heisenberg model $J_1 - J_d - J_\chi$ via the Gradient Descent method to find a possible region of classical disorder, as well as relevant ordered phases to the model. Furthermore, we present numerical evidence from the SSSF and GSE that uncatalogued noncoplanar phases - dubbed as FM-stripe, FMd, and AFMd - can be stabilized due to the interplay between the novel chiral J_χ interaction, the FM first-neighbors J_1 and AFM diagonal J_d interactions.

3.1 Classical Phase Diagram for the $J_1 - J_d - J_\chi$ Heisenberg model

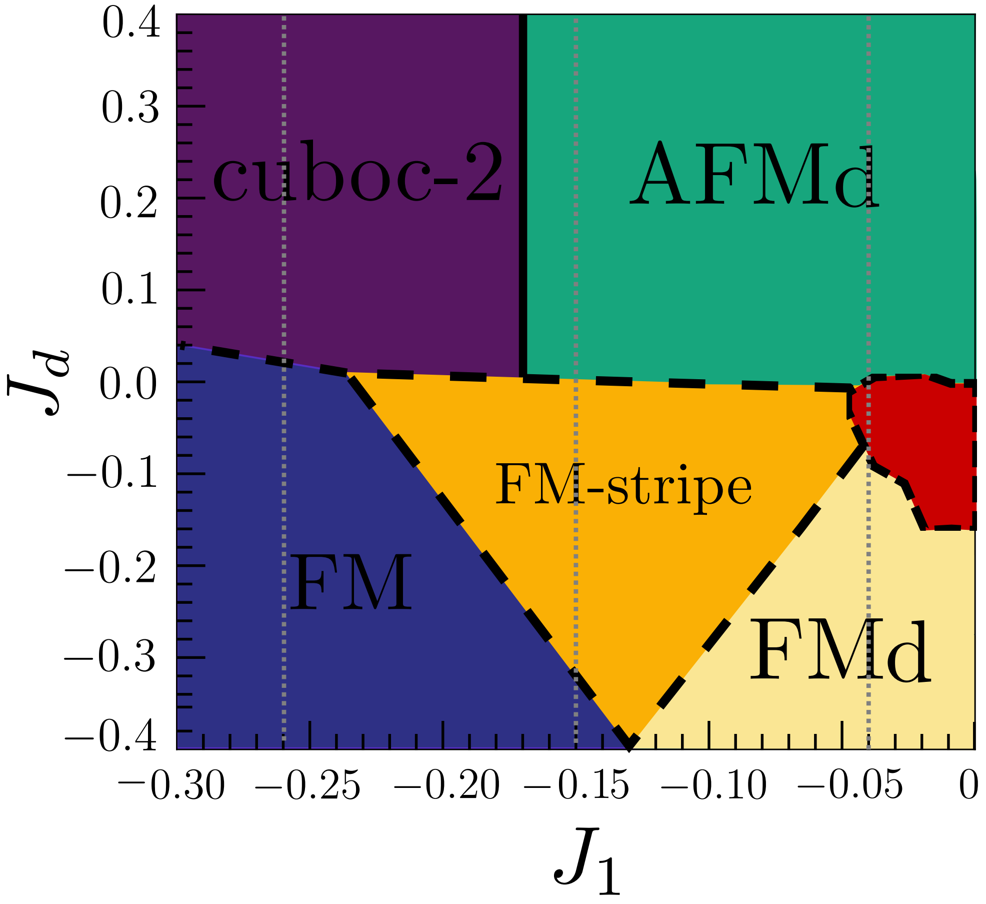

Figure 16 – Classical phase diagram for the $J_1 - J_d - J_\chi$ Heisenberg model on the Kagome lattice with $J_\chi = 1.0$ setting the energy scale. We have five classical ordered states: cuboc-2, AFMd, FM , FM-stripe, and FMd. Black dashed lines indicate first-order phase transitions. The solid line between the cuboc-2 and the AFMd phases indicates a continuous transition. A classically disordered region, in red, is present around the point $J_1 = J_d = 0$. Vertical gray lines are related to the minimization examples in Fig. 18.

Source: By the author.

Following the previously explained methodology in Section 2.1, we obtained the classical phase diagram for the extended chiral Heisenberg model (1.1). This was done by considering $N \in [100, 200]$ distinct random initial configurations which converged to a configuration correspondent to the minimum of the classical energy in a fixed set (J_1, J_d, J_χ). The energies of each random configuration are then compared variationally, a procedure that enables the algorithm to access more configurations from the classical phase space. This methodology was applied for lattices with $L \in [3, 20]$ to probe phases with different magnetic unit cell sizes. This process is illustrated in Figure 18, where we compare the GSE of each ordered phase with GD results. As an initial benchmark, we observe that the algorithms are able to describe the regime of weakly coupled AFM(FM) chains for $J_d \gg J_\chi > (<)\, 0$ with $J_1 = 0$[12,41,52] (Fig. 17). Notice that these are not ordered phases. The SSSF shows blurred peaks and weight distribution over the BZ.

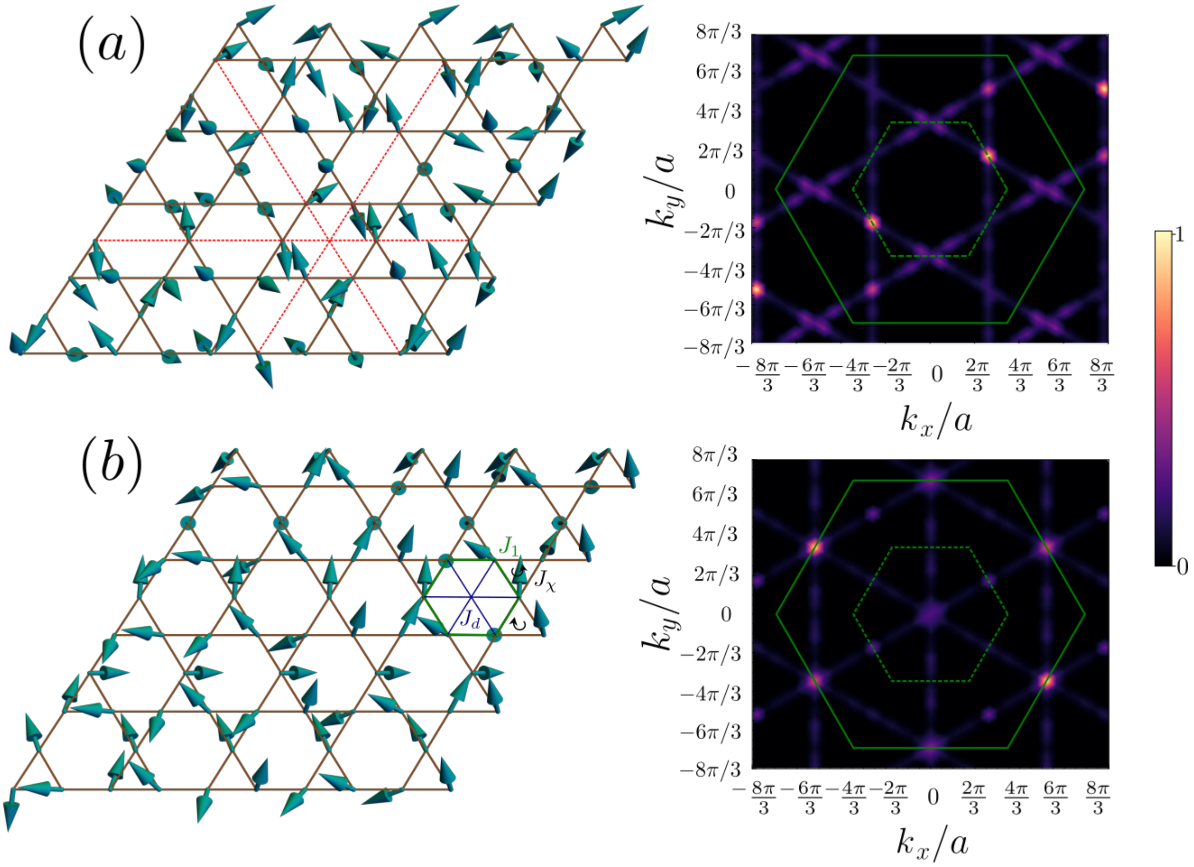

Figure 17 – Classical spin representation for the regime $J_d \gg J_\chi$ in the $J_1 - J_d - J_\chi$ Kagome Lattice model of weakly coupled chains, with the correspondent spin structure factors. In this scenario, AFM (FM) spin chains which are weakly coupled for $J_d > 0$ ($J_d < 0$), can be seen along the diagonal dashed red lines on the hexagons of the Kagome lattice (a) [(b)].

Source: By the author.

After defining the corresponding configuration to the GSE minimum, we calculate the SSSF for the configuration to confirm if there is an ordered or disordered structure on the BZ. New magnetic ordered phases are then determined if they correspond to the minimum GSE on a certain region of the phase diagram, with a well-defined SSSF that is not compatible with previously known ordered phases.

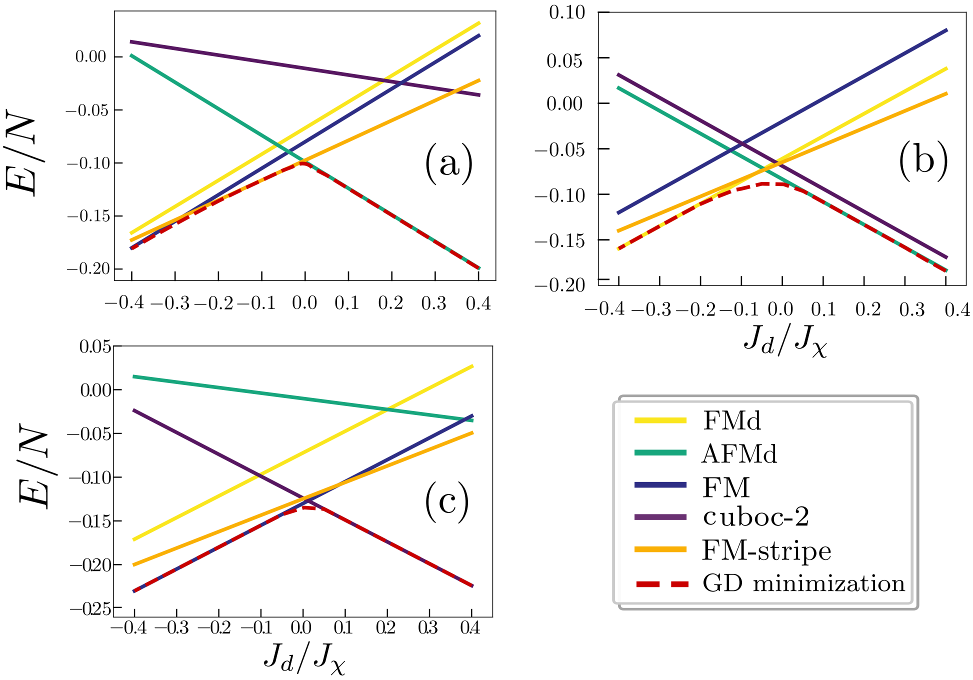

Figure 18 – Energy comparison between FMd, AFMd, FM-stripe, FM, cuboc-2 phases and the result of numerical minimization via the GD method along the values (a) $J_1 = -0.16$, (b) $J_1 = -0.04$ and $J_1 = -0.26$ (c). In the second case, the minimum energy near $J_d/J_\chi \approx 0$ is not equivalent to any ordered phase, and the correspondent SSSF is characterized by a blurred profile. Same color code as used in Fig. 16.

Source: By the author.

Setting the energy scale with $J_\chi = 1$ with no loss of generality, in addition to the cuboc-2 [Fig. 20(a)] and FM [Fig. 20(c)] phases, three new ordered phases occupying a considerable region of the phase diagram were encountered: FMd [Fig. 20(e)], AFMd [Fig. 20(b)] and FM-stripe [Fig. 20(d)]. The FM(AFM)d phases are named after the FM (AFM) chains along the diagonals on the hexagons coupled via the J_1 interaction, whereas the FM-stripe is an intermediate phase between the FM and FMd, with some twisting near the triangles responsible for a non-zero chirality*. The classically disordered region, a good indicator for the search of quantum spin liquids, was characterized by a blurred SSSF (Fig. 19). This region is marked on the classical phase diagram in Figure 16, and it is consistent with the usually expected presence of classical disorder in the boundary between ordered phases, due to competing interactions.

The FM-stripe phase can be stabilized in three possible configurations distinguished

---

* The stripe nomenclature is usually chosen for phases that break some rotational symmetries from the lattice, besides the usual spin rotational symmetry.[119]

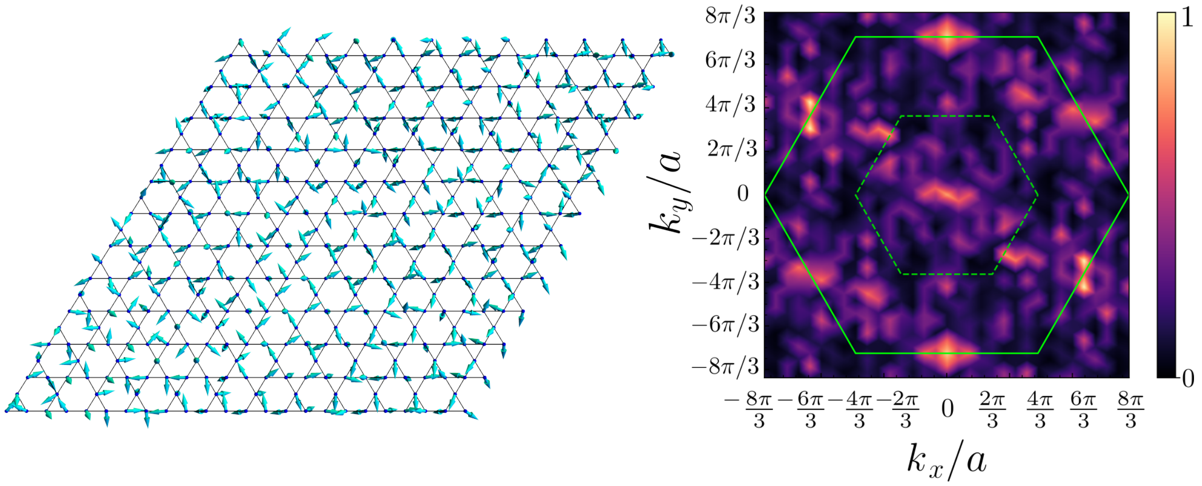

Figure 19 – Classically disordered region spin configuration in real space and correspondent SSSF. The state is only one of the many possible states inside the disordered region.

Source: By the author.

by a rotation of $2\pi/3$ in the reciprocal and real space. The FMd phase can be understood more intuitively by observing the FM chains along the diagonals of hexagons, with the fact that the chiral interaction induces a relative angle between the diagonal chains which minimizes the staggered chirality. Finally, the AFMd phase is an interesting phase that interpolates both the characteristic Bragg peaks for the cuboc-1 and cuboc-2 phases, with varying relative intensity depending on the value of the J_1 coupling. Therefore, the effect of first-neighbor interactions is based on adjusting the angle of the AFM chains while minimizing the chiral interaction. This introduces a non-trivial dependence of the angle between the spins in the magnetic unit cell by the J_1 coupling. This is similar to the transition between a canted AFM and the polarized phase with $J_1 \leftrightarrow h$. Instead of directly representing this dependence in an analytical form, we represented these new states with the numerical outputs from the GD minimization.

The continuous phase transition between the cuboc-2 state to the AFMd arises with the weakening of the cuboc-1 momentum points in the BZ and the strengthening of the cuboc-2 points as $|J_1|$ is increased negatively. For $J_1 > 0$, an opposite situation occurs, benefiting the cuboc-1 state (see Figure 21 and 22). Although the ordered phases icosahedron2, tetrahedral1, tetrahedral2, and traditional octahedral[18,61] have similar Bragg peaks in the BZ, they are not representative for the model with staggered chirality ($J_\chi < 0$ for up triangles and $J_\chi > 0$ for down triangles). In a uniform chiral model, this octahedral phase would contribute with maximum chirality to the ground state energy, for example.

The phase transition between the phases FM, FM-d, and FM-stripe is characterized by discontinuities near the phase boundaries from the classical phase diagram [Fig. 23]. Additionally, this is accompanied by a change in the magnetic unit cell size describing these phases (Fig. 20). Although some variation of the Bragg peaks is present inside the FM-

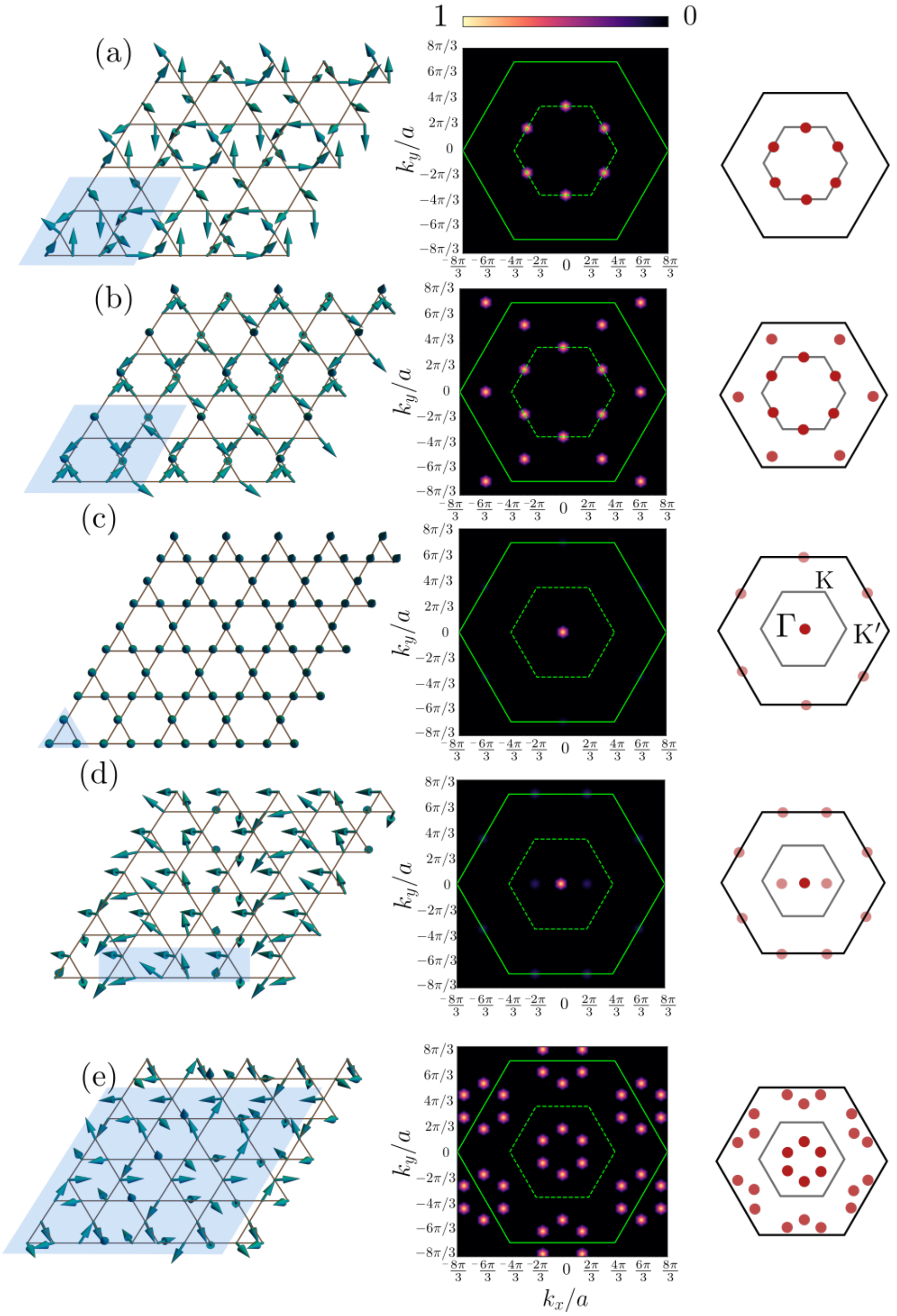

Figure 20 – Classical spin configurations (left column) and corresponding SSSF (right column) for the phases in Fig. 16 with $J_\chi = 1.0$. The magnetic unit cell is shown in blue. (a) cuboc-2; (b) AFMd ($J_1 = -0.05,\ J_d = 0.3$); (c) FM; (d) FM-stripe ($J_1 = -0.13,\ J_d = -0.16$); (e) FMd ($J_1 = 0,\ J_d = -0.3$). The color scale on the right is arbitrary. The FM-stripe phase is stabilized in one of three equivalent configurations distinguished by a $2\pi/3$ rotation.

Source: By the author.

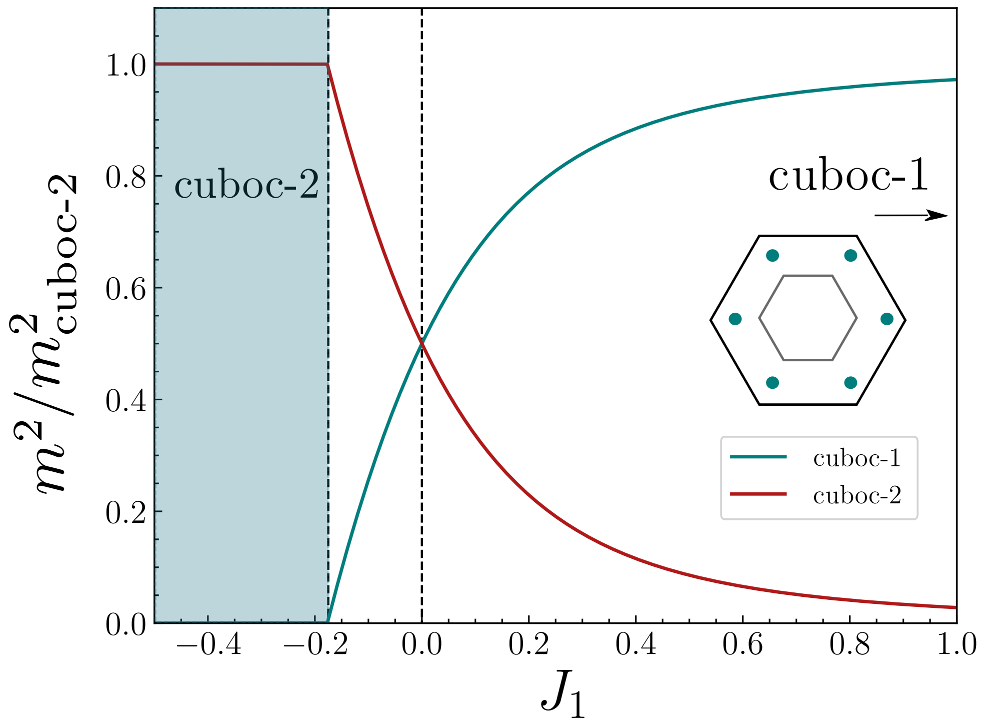

Figure 21 – Order parameter squared (normalized with respect to its value in the cuboc-2 state) as a function of J_1, indicating the continuous transition between the cuboc-2 and AFMd phases for $J_\chi = 1$. The red (light-blue) curve shows the normalized Bragg peak intensity at the cuboc-2(1) ordering wave vectors. At the point $J_1 = 0$ an octahedral phase maximizing the staggered chirality emerges. The phase transition to the cuboc-1 is slower and takes place in the vicinity of $J_1 = 1.0$ (not shown).

Source: By the author.

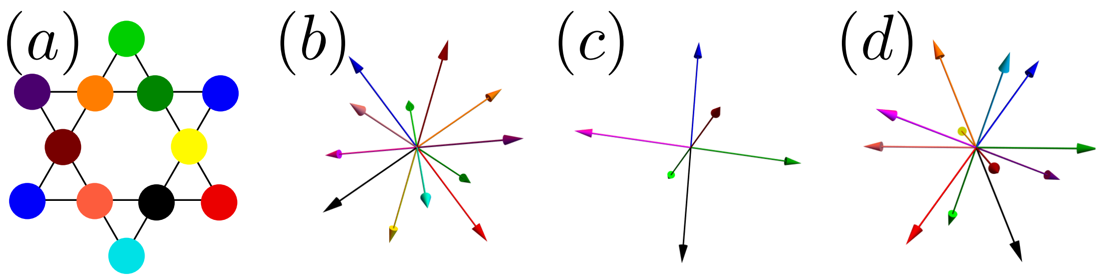

Figure 22 – The spin directions on the magnetic unit cell (a) for the cuboc-2 (b) ($J_1 = -0.4$), octahedral ($J_1 = 0$) (c) and cuboc-1 ($J_1 = 1.0$) (d). An animated gif of the continuous phase transition between cuboc-2 and cuboc-1 phases seen from the perspective of the spins in the magnetic unit cell can be seen in this link.

Source: By the author.

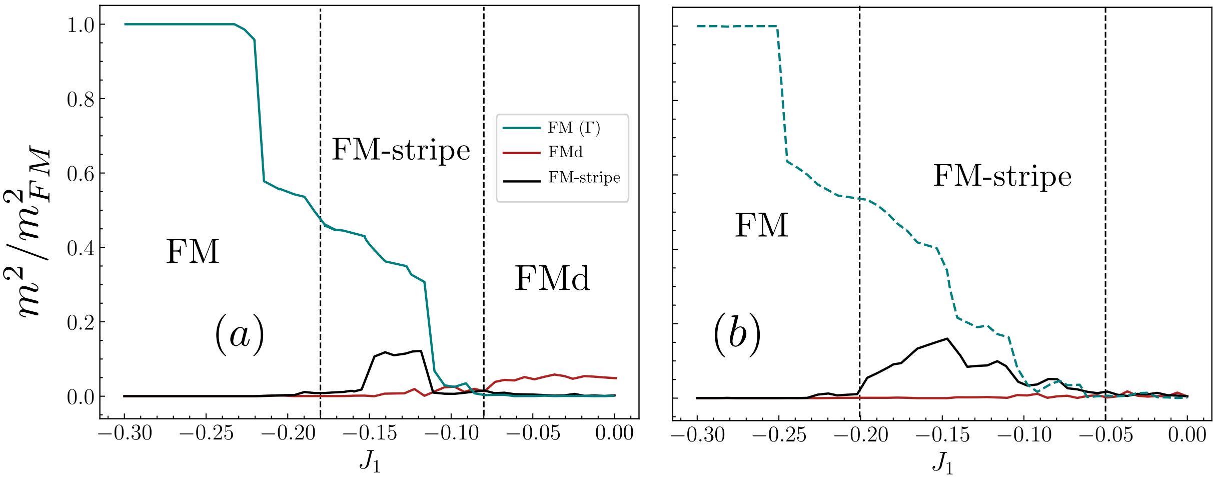

Figure 23 – Order parameter squared (normalized with respect to its value in the FM state) as a function of J_1, indicating the phase transition between the FM, FM-stripe and FMd phases for $J_\chi = 1$ and $J_d = -0.20$ (a), and $J_d = -0.15$ (b). The red (light-blue) [dark] curve shows the normalized Bragg peak intensity at the FMd(FM, $\mathbf{\Gamma}$ momentum point) [FM-stripe] ordering wave vectors. The dashed lines indicate the boundary of phases from Fig. 16. In the second case (b), the FMd phase is close to the disordered region and does not develop pronounced Bragg peaks.

Source: By the author.

stripe phase, the previous indications suggest a first-order phase transition. Specifically, the variation inside the FM-stripe phase may be influenced by the difficulty of the minimization algorithm on stabilizing to one of the possible phase variations related by a $2\pi/3$ rotation.

3.2 Discussions

The scenario of novel chiral classical ordered phases and a regime of disorder may be relevant for the description of the phase transition between cuboc-type phases to a QSL on Kapellasite-like materials. In Fåk *et al*, 2012,,[3] the authors argued that the only ordered phase close to the momentum vector $\boldsymbol{M} = (1/2, 0)$ known at the time was the cuboc-2, indicating therefore that the short-range correlations of Kapellasite would be of the cuboc-2 type for non-zero temperature. A study of high-temperature series expansion on the experimental data from Nuclear Magnetic Resonance (NMR) of magnetic susceptibilities and total specific heat also corroborated with this proposal.[3] Nevertheless, it would be interesting to see more experimental results in the context of these new findings for the $J_1 - J_d - J_\chi$ Heisenberg model.

As we have seen, the staggered chirality furnished the ideal conditions for an octahedral phase to appear in the symmetrical point $J_1 = 0$ with $J_d > 0$ in the phase diagram of the modified Heisenberg model. The main difference of this phase to the usual octahedral phase[18,61] is the exchange of some spins in the magnetic unit cell that minimizes the overall chirality. By the same token, although we have not investigated this with detail - since our main objective was to characterize a region of classical disorder in the classical phase diagram -, similar phases to the icosahedron[61] with exchanged spins that favor the staggered chirality might be feasible and relevant for materials described by a chiral modified Heisenberg model. From the methodological perspective, it would also be interesting in the future to implement improvements to the GD method by exploring the Stochastic gradient descent method, for example, which introduces stochastic noise in the minimization procedure.[63,120,121]

Some theoretical studies indicated that Mott insulators with noncoplanar magnetic ordered states can be seen as parent states to CSLs. Consequently, the CSL can be accessed by quantum melting the regular magnetic ordered phases.[32] This procedure is effectively done by introducing frustration and/or quantum fluctuations in classical regular magnetic ordered phases[18] theoretically, whereas experimentally this is achieved by tuning effective couplings via pressure, or chemical modifications that melt the ordered phases. In this context, exploring the robustness of these new phases against quantum or thermal fluctuations via numerical spin waves calculations, for example, could be relevant for a more detailed quantum phase diagram of the $J_1 - J_d - J_\chi$ Heisenberg model.[122]

Finally, we address the classically disordered region. In all its extent, the SSSF shows neither Bragg peaks nor sharp features, and its weight is distributed over the entire BZ, (Fig. 19). A classically disordered region is tied to the presence of massively degenerated states and usually occurs at isolated points in the phase diagram, for instance at the boundaries between two ordered phases. Its extended nature in the present problem may be traced back to the frustrating nature of the Kagome lattice. Consider a spin S_j. To maximize the chiral interaction, we place the nearest neighbors of S_j in a plane perpendicular to it. This causes an accidental degeneracy under relative rotations of these nearest-neighbor spin planes about the axis defined by S_j. Although quantum fluctuations may lift this degeneracy via the order-by-disorder mechanism[123–126] the presence of an extended classically disordered region is a promising sign that a CSL might be stable for $S = 1/2$, as we will see in the following Chapter.

4 GAPLESS CHIRAL SPIN LIQUID IN THE KAGOME LATTICE

After obtaining an indication of a disordered region in the classical phase diagram, now we focus on the trial wavefunctions proposed recently[12] to describe a possible CSL in the $J_1 - J_d - J_\chi$ Heisenberg model. After briefly considering the MFT for the Ansätze, we present numerical evidence that the CSL may be stable near the origin of the phase diagram. Furthermore, by implementing an SDW trial wavefunction for the AFMd, FMd, and FM-stripe phases, we investigate the instability from the CSL towards these ordered phases.

4.1 Parton Mean Field Theory

We begin by considering the MFT of the $J_1 - J_d - J_\chi$ Heisenberg model (1.1), which was developed recently.[12,13] By following the standard mean field decoupling using the Abrikosov representation (2.21), the contributions in the diagonal and first-neighbors can be written as

$$H_d = -\frac{J_d}{2} \sum_{\alpha, ij \in \hexagon} \left[f^\dagger_{i\alpha} f_{i\alpha} \chi_{ij} + \text{h.c.} - |\chi_{ij}|^2 \right], \tag{4.1}$$

and

$$H_1 = -\frac{J_1}{2} \sum_{\alpha, \langle ij \rangle} \left[f^\dagger_{i\alpha} f_{i\alpha} \chi_{ij} + \text{h.c.} - |\chi_{ij}|^2 \right]. \tag{4.2}$$

Similarly, the chiral interaction contribution for the up triangles ($\triangle$), for example, can be written as

$$H^{\triangle}_{\chi} = \frac{3iJ_\chi}{16} \sum_{ijk \in \triangle, \alpha} \left[-\chi_{ik}\chi_{kj}\chi_{ji} + \chi_{kj}\chi_{ji} f^\dagger_{i\alpha} f_{k\alpha} + \chi_{ik}\chi_{kj} f^\dagger_{j\alpha} f_{i\alpha} + \chi_{ji}\chi_{ik} f^\dagger_{k\alpha} f_{j\alpha} - \text{h.c.} \right], \tag{4.3}$$

with a similar expression for down triangles. The mean-field parameter is given by $\chi_{ij} = \langle f^\dagger_{i\uparrow} f_{j\uparrow} + f^\dagger_{i\downarrow} f_{j\downarrow} \rangle$. The possible Ansätze describing CSLs were recently studied in an extension of the Projective Symmetry Group by Bieri *et al*, 2016.[25] Consequently, the considered Ansätze in this work are correspondent to the No. 11 (imaginary diagonal hopping) and No. 9 (real diagonal hopping) in Table IX of this reference (see Figure 24). More specifically, we consider the former (Cases I and II) in the MFT analysis since they are more representative to the CSL, but the results for the latter (Case III) are also presented in the VMC study. From the Fourier transform of the spinon operators, the diagonal form of the MFT Hamiltonian is then determined as

$$H = \sum_{\boldsymbol{k}, \alpha} \Psi^\dagger \mathbb{M} \Psi \; + N J_1 \chi_1^2 + \frac{N J_d \chi_d^2}{2} + \frac{N J_\chi \chi_1^3}{2}, \tag{4.4}$$

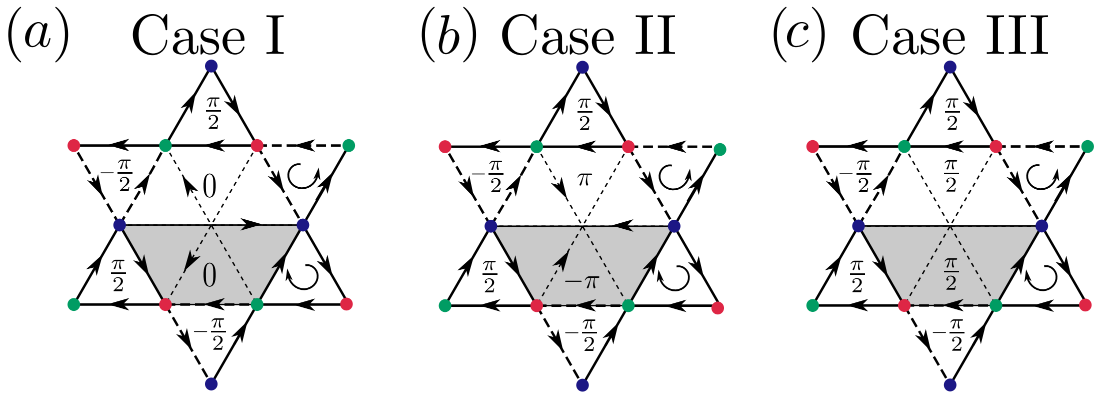

Figure 24 – Physical Ansätze describing the CSL with 0 gauge flux over the hexagons and staggered $\pm\pi/2$ flux on the elementary triangles. Cases I, II and III are indicated at subfigures (a) with oriented χ_d (b), and non-oriented $\chi_d \in \mathbb{R}$ (c). Interactions between different sublattices are always oriented with $\chi_1 \in \mathbb{C}$.
Source: By the author.

with the spinor $\Psi_{\boldsymbol{k},\alpha} = \begin{pmatrix} f_{A,\boldsymbol{k},\alpha} & f_{B,\boldsymbol{k},\alpha} & f_{C,\boldsymbol{k},\alpha} \end{pmatrix}^T$ and the matrix

$$\mathbb{M} = -\begin{pmatrix} \kappa_d \sin(k_A) & \kappa_1 \sin(k_C/2) & \kappa_1 \sin(k_B/2) \\ \kappa_1 \sin(k_C/2) & \kappa_d \sin(k_B) & \kappa_1 \sin(k_A/2) \\ \kappa_1 \sin(k_B/2) & \kappa_1 \sin(k_A/2) & \kappa_d \sin(k_C) \end{pmatrix}. \tag{4.5}$$

Here, $k_s = \boldsymbol{k} \cdot \boldsymbol{a}_i$ with $s = A, B, C$, $i = 1, 2, 3$, and the lattice vectors $\boldsymbol{a}_i$ represented in Figure 4. The new effective hopping parameters κ are given by

$$\kappa_1 = \frac{3}{8} J_\chi \chi_1^2 - J_1 \chi_1 \quad \text{and} \quad \kappa_d = \chi_d J_d, \tag{4.6}$$

and the energy spectrum is obtained by the numerical diagonalization of matrix (4.5).

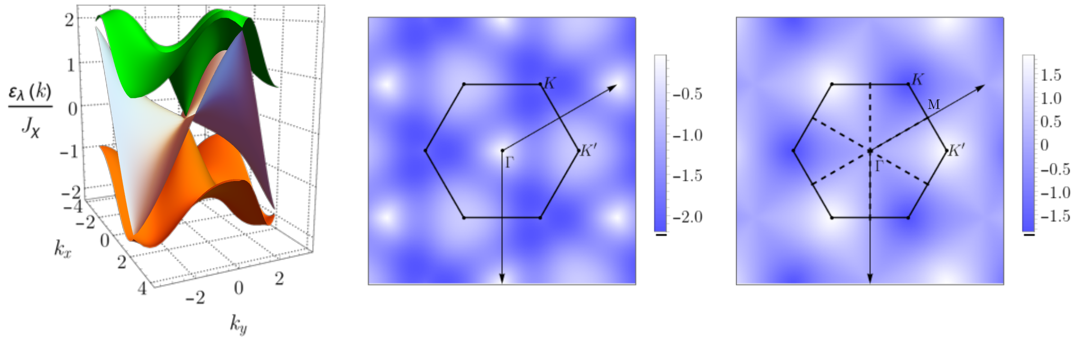

Figure 25 – Energy spectrum representation for $\kappa_d/\kappa_1 = 1.2$ (left). This form is representative for $0 < \kappa_d < 2\kappa_1$. The density plot of the dispersion for the lower (center) and upper bands (right) is also presented. In the latter, dashed lines indicate the spinon Fermi surface for the middle band (along the $\boldsymbol{\Gamma} - \boldsymbol{M}$ points in the BZ).
Source: OLIVIERO *et al.*[13]

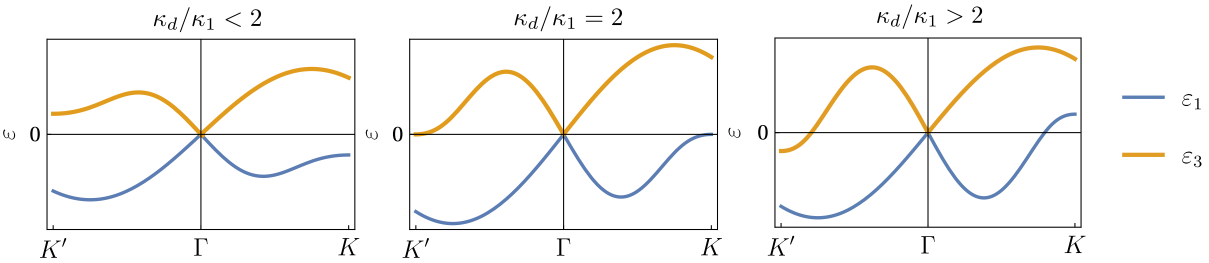

Figure 26 – Energy dispersion for the lower and upper bands, along the Γ-K direction, for different values of the ratio κ_d/κ_1.
Source: OLIVIERO *et al.*[13]

From Figure 25 the Dirac Cones at the $\mathbf{\Gamma}$ momentum point in the BZ can be seen. If the ratio κ_d/κ_1 is increased, the energy gap for the upper and lower bands at the points K and K' in the BZ is decreased, as they cross the Fermi level $\varepsilon_f = 0$ benefiting the formation of Fermi pockets with $\kappa_d/\kappa_1 > 2$. These elements indicate a nesting instability of the U(1) CSL towards ordered phases.[127] For $\kappa_d < 0$ the instability is indicated by the flattening of the middle band near $\kappa_d/\kappa_1 \approx -1$. Consequently, the VMC analysis of the CSL must be restricted by the interval $-1 < \kappa_d/\kappa_1 < 2$. Independently of the sign of κ_d, the instability of the CSL is consistent with the expected behavior of a transition towards ordered phases in the regime of dominant J_d[41] in the considered model (1.1).

4.2 VMC results

To observe the contribution of each coupling sector on the estimated GSE via the VMC, we varied the hopping ratio κ_d/κ_1 up to the regime when the diagonal J_d interaction is dominant, where the Hamiltonian describes a set of weakly coupled AFM $S = 1/2$ chains[41,54] rotated by $2\pi/3$ to each other. In this regime, the diagonal J_d energy contribution is well described by the exact solution via the Bethe's ansatz[82] expression,

$$E_{AFM-chain} = J_d\left(\frac{1}{4} - \ln 2\right), \tag{4.7}$$

which is indicated in Fig. 27 with a solid orange color. Additionally, the individual contributions for each coupling sector are presented, and for a set (J_1, J_d, J_χ) the corresponding GSE can be calculated with the expression

$$F\left(\kappa_d/\kappa_1\right) = J_d\langle E_{J_d}\rangle + J_\chi\langle E_{J_\chi}\rangle + J_1\langle E_{J_1}\rangle, \tag{4.8}$$

which must be minimized as a function of the variational parameter κ_d/κ_1. For Cases I and II this minimization was performed in the region of $\kappa_d/\kappa_1 \in [-1, 2]$ as discussed previously.[12]

A particular case of interest at $J_1 = 0$ is illustrative for the ground state energy difference between the different Ansätze and important remarks about our VMC. From Figure 28, the CSL is competitive in the region of $J_d/J_\chi \in [-0.3, 0.2]$. Cases I-III are

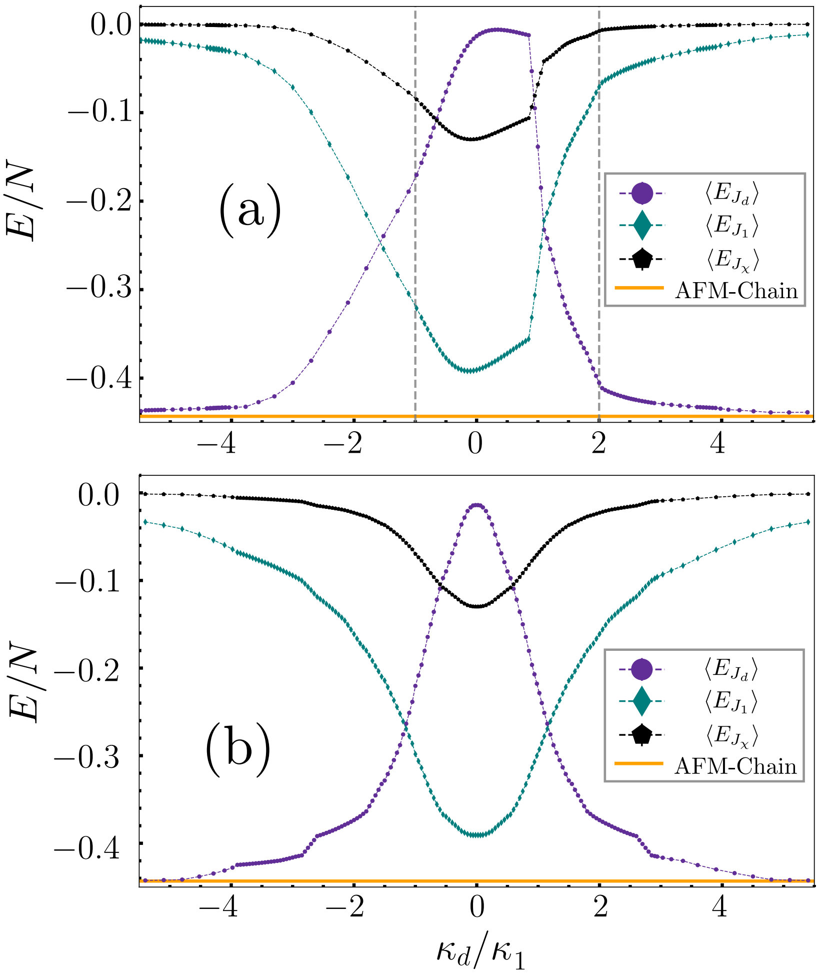

Figure 27 – VMC energy expectation value for the chiral (green), Heisenberg J_1 (black) and J_d (purple) contributions for (a) Case I ($\kappa_d/\kappa_1 < 0$) , II ($\kappa_d/\kappa_1 > 0$) and (b) III ($\kappa_d/\kappa_1 \in \mathbb{R}$). The orange line is the result for the AFM S=1/2 chain via Bethe's ansatz. These energies were obtained for $L = 12$; Error bars are smaller than the markers. Gray vertical dashed lines indicate the region of stability for Cases I and II established from the MFT analysis.
Source: By the author.

approximately degenerate for $J_d/J_\chi < 0$ from the perspective of our VMC and a more detailed analysis is needed to confirm which Case is favored*. The degeneracy is lifted for $J_d/J_\chi > 0$, and Case I is favored energetically. Therefore, Cases II and III are not representative to describe the CSL in this region. Similar behavior was found for $J_1 \neq 0$, and consequently, Case I was chosen to represent energetically the CSL in the following discussions. Finally, if the variational minimization of the parameter κ_d/κ_1 is performed unconstrained, our VMC captures the Bethe's ansatz solution for all cases in the limit where the CSL is no longer competitive. In this regime, the numerical results for the

---

* Recently an analytical dependence of the entanglement entropy spectrum on gauge fluxes for quantum spin liquids was proposed;[128] by calculating this observable with tensor network-based methods,[90] one could in principle observe which flux state best describes the entropy profile.

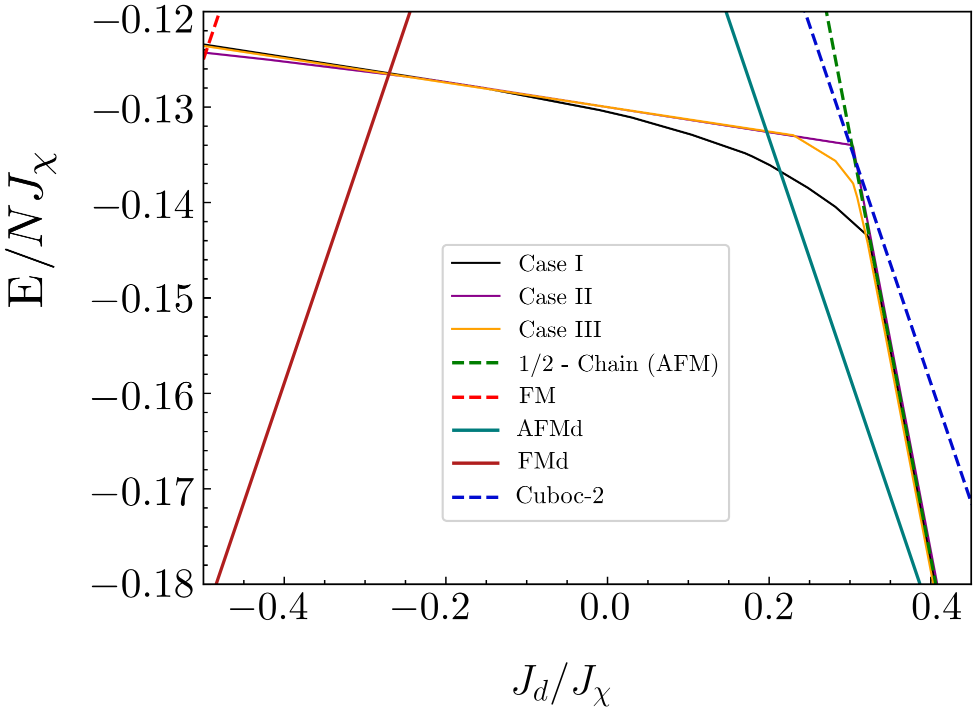

Figure 28 – Ground state energy obtained via VMC for Cases I-III as a function of J_d/J_χ with $J_1 = 0$. Classical energies for phases Cuboc-2, AFMd, FMd and FM are displayed for comparison.
Source: By the author.

Gutzwiller projected wave function ansatz in the AFM spin chain from Subsection 2.3.0.1 are recovered. This result is also in agreement with the expected instability to weakly coupled AFM(FM) chains along the the diagonal of hexagons in the Kagome lattice for $J_d/J_\chi \gg 0$[12,41] (Figure 17).

4.3 Quantum Phase Diagram for the $J_1 - J_d - J_\chi$ Heisenberg model

Our previous classical results established a considerable region on the phase diagram for the possible appearance of a gapless spin liquid arising from the classically disordered region. For $J_1 = 0$ we confirmed this expectation. Now we consider $J_1 \neq 0$. The consistent inclusion of quantum fluctuations is essential to determine the possible stability of the CSL towards ordered phases. In this context, we proceed with our investigations by adopting the SDW class of Ansätze described in Subsection 2.2.5.

Our VMC simulations consist of $N_{warm} \sim 10^4$ MC steps for thermalization and we calculate the ground state energy E_0 in the end of every sweep for $N_{meas} \sim 10^4$. The variational minimization is then calculated with respect to the variational parameters κ_d/κ_1 and h. The phase transition out of the CSL is determined by the development of a non-zero expectation value in the thermodynamic limit for the sublattice magnetization m defined as[111]

$$m^2 = \lim_{|i-j|\to\infty} \langle \boldsymbol{S}_i \cdot \boldsymbol{S}_j \rangle, \tag{4.9}$$

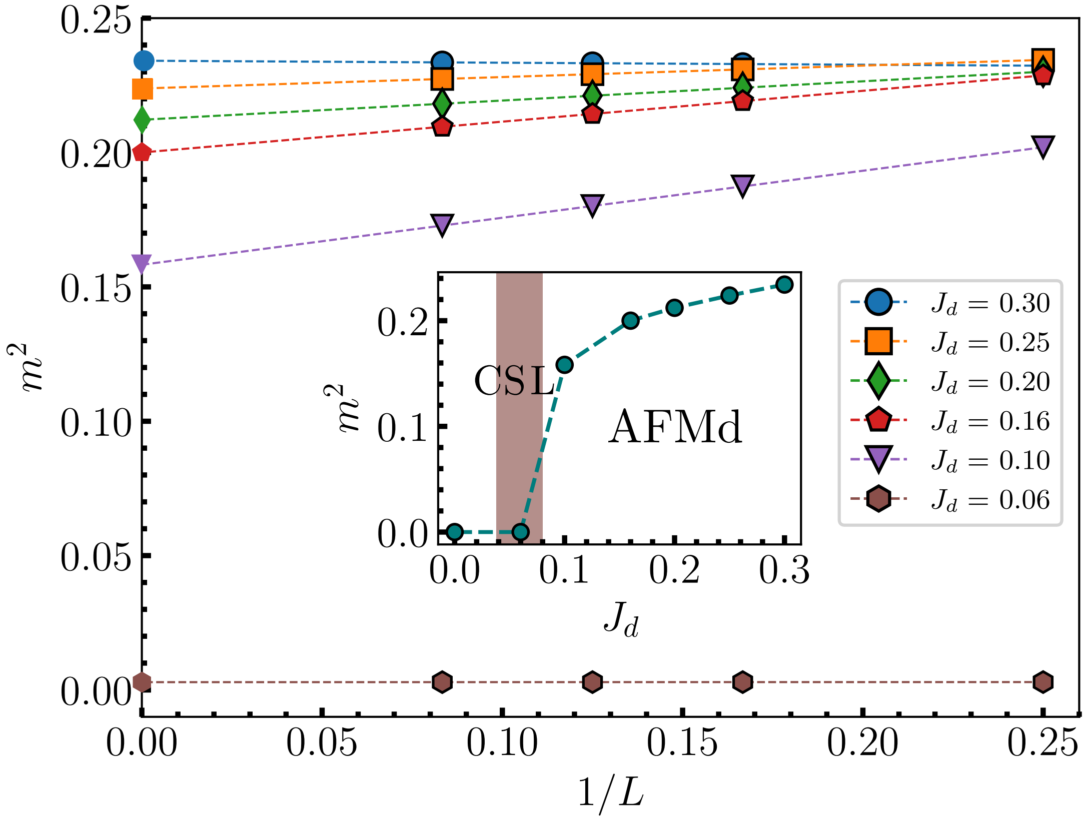

Figure 29 – Finite-size scaling for the magnetization with $J_1 = -0.01$ and $J_\chi = 1.0$ as a function of $1/L$. The inset graphic displays the phase transition between the AFMd and the CSL from the perspective of the magnetization in the thermodynamic limit as a function of J_d. The colored region indicates the numerical uncertainty in the phase transition.

Source: By the author.

alongside a direct comparison between the ground-state energies. This observable m is essentially the spin-spin correlation at a maximum distance for two spins correspondent positions inside the magnetic sublattice. From the ground state energy perspective, the phase transition occurs with a swap in the global minimum from the CSL near-zero h to the ordered phases with a finite value of h. Physically this is consistent because if $h \neq 0$ the mean-field dispersion becomes gapped. In 2D, this implies that the CSL is unstable and the spinons become confined.[7] The resulting phase is then adiabatically connected to the ordered state.

This new variational minimization concerning h is performed with fixed κ_d/κ_1 value obtained for the energy minimum on the pure CSL regime. At $h = 0$ we checked that this leads to consistent results. Figure 29 exemplifies these concepts by displaying the phase transition between the CSL and the AFMd phase along the vertical line $J_1 = -0.01$ on the quantum phase diagram. The results for the transition were obtained with $L = 2n(n = 2, 3, 4, 6)$ and the extrapolated value is represented in the markers without the black border at $1/L \to 0$.

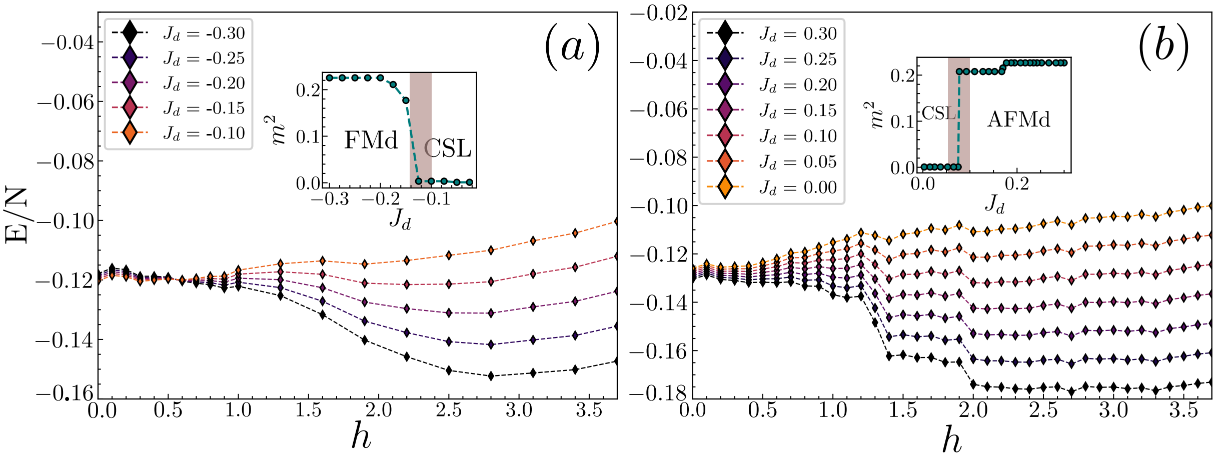

Figure 30 – Energy as a function of the Zeeman coupling h for different values of J_d. Both the transition from the CSL to the FMd (a), at $J_1 = -0.02$, and to the AFMd (b), at $J_1 = -0.01$, are presented. The magnetization plateaus in the second case are illustrative to the difficulty of selecting the phase transition boundary precisely. Error bars are smaller than the markers, and the shaded region in the inset indicates the numerical uncertainty in the phase transition.
Source: By the author.

Since the classical phases FM(AFM)d have a non trivial angle dependence with J_1, the classical states of reference $\boldsymbol{m}$ in equation (2.69) are chosen with a fixed value of J_1 and each VMC minimization is performed varying J_d. Some of these analyses can be seen in Figure 30. The ground state energy is represented for different values of the parameter h for two fixed values of J_1. As J_d is varied, both cases depict the transition between a minimum ground state energy near $h \approx 0$ to an ordered phase with $h \neq 0$. This transition can also be understood from the perspective of the magnetization observable (4.9) as can be seen in the inset Figures. These results indicate a first-order phase transition since a clear discontinuity separates the ordered phases AFM(FM)d and the CSL.[111] Magnetization plateaus in Heisenberg-like models usually reflect finite-size effects,[129] and in our case, they hinder the possibility of selecting the phase boundary precisely. Consequently, a region (brown) of uncertainty is estimated to accommodate this difficulty in our VMC.

The results of the quantum phase diagram obtained in the vicinity of the CSL are displayed in Figure 31. The phase transitions are consistent with the classical phase diagram in Figure 16, and the CSL domain expands from the classically disordered region up to small values of J_d and J_1. Specifically, phase transitions with the FM-stripe phase were obtained for systems with $L = 12$. With the inclusion of quantum fluctuations, the regime for the FM-stripe phase near the CSL is reduced as the FMd increases in comparison to the classical results. This can be understood intuitively since the FMd phase has three coupled FM chains along the diagonal of the hexagons (while the FM-stripe has only one), and FM chains are usually robust against fluctuations. Moreover, one may think

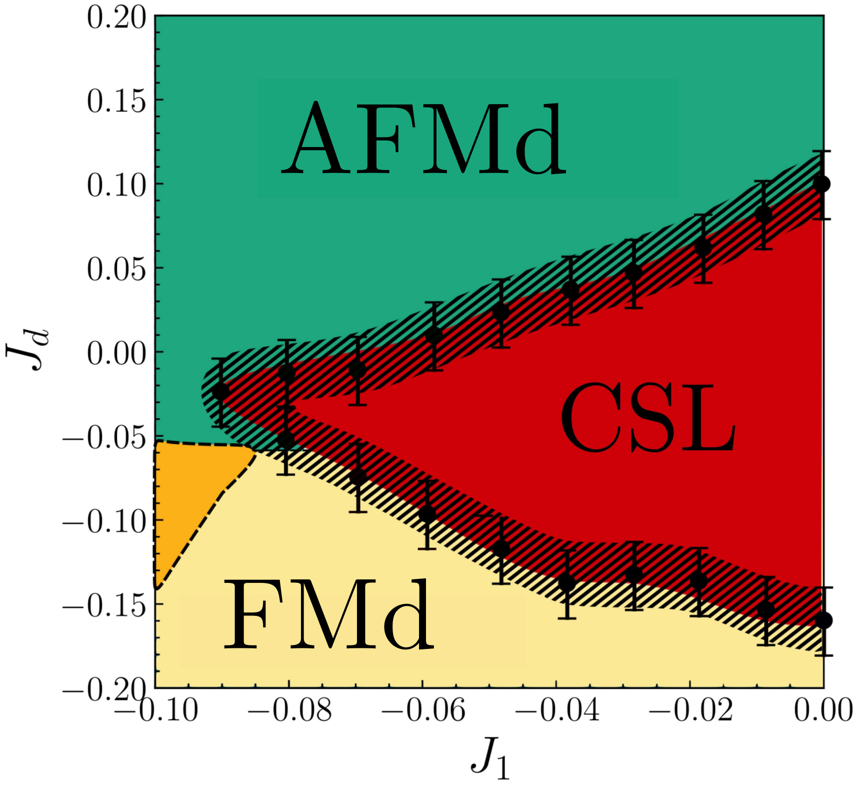

Figure 31 – Quantum phase diagram for the $J_1 - J_d - J_\chi$ Kagome Lattice model with S=1/2. The phase transitions were obtained from the VMC comparison with an SDW ansatz. The error bars indicate the numerical limitation of our VMC, which consists on a estimate of the plateaus of magnetization. Same color code used in Figure 16. The FM-stripe phase is indicated in orange.

Source: By the author.

that the superposition of the different domains favors the CSL close to stripe boundary analogously to an RVB state.

Finally, we remark that the inclusion of Jastrow spin-spin correlations[111] may lead to an improvement of the variational energy for the classical states and this may diminish the region of stability of the CSL in the thermodynamic limit. Additionally, due to numerical limitations of our VMC we have not obtained the finite-size scaling analysis for the FMd/CSL phase transition since it demands the scaling of systems with sizes multiples of $L = 8$. This situation could be improved by implementing the Stochastic Reconfiguration[105] for the optimization of the variational parameters, for example. In this context, the error bars on the marks of Figure 31 indicate the numerical limitation of our VMC which consists of an estimate of the plateaus of magnetization in the vicinity of the phase transition.

5 CONCLUSIONS AND OUTLOOK

In this dissertation, we have mainly investigated QSLs in the context of parton constructions and Gutzwiller projected wave functions, which were implemented via the VMC. In Chapter 2, by constructing a VMC capable of obtaining the ground state energy of different effective theoretical models that describe QSLs, we have investigated how these exotic phases of matter can be described via Abrikosov or Majorana fermionic representations. More specifically, we studied the AFM Heisenberg Hamiltonian in the context of spin chains, U(1) Dirac, and Chiral spin liquids on the Kagome Lattice. Our results were consistent with previous results in the literature regarding these investigations and were fundamental for constructing a reliable VMC for the investigation of the CSL in Chapter 4. Additionally, we also presented how magnetically ordered phases can be described with the conjunction of the Gradient Descent algorithm and the analysis of the static spin structure factor. In this context, we were able to implement an algorithm capable of characterizing features of both ordered and disordered states in strongly correlated systems.

Following this developed methodology, in Chapter 3 we investigated relevant ordered phases for the Kagome lattice in the context of the $J_1 - J_d - J_\chi$ model and related modified Heisenberg models. From this, we found numerical evidence for an extended region of disorder in the classical phase diagram from the static spin structure factor observable for small J_1 and J_d and significant J_χ. This was our first indication for the presence of the proposed CSL.[12,13] Additionally, we found non-trivial magnetic ordered phases dubbed as FM-stripe, AFMd, and FMd on the classical phase diagram which are stabilized primarily due to meaningful J_χ interactions, with the spins having a complex angle dependence on J_1. More surprisingly, we found a continuous phase transition between the cuboc-1 and cuboc-2 phases, which is interpolated by the AFMd on the regime of $J_1 < 0$. At the symmetrical point $J_1 = 0$, a variant of the octahedral phase that favors a staggered chirality was found. Our results may be relevant, for example, to the understanding of the physics of the Kapellasite material, upon which cuboc-type short-range spin-spin correlations persist up to $T = 20$ mK in experimental setups[3] and compete with a gapless quantum spin liquid[*].

In Chapter 4 we have found numerical evidence that a parton MFT is indeed representative to the disordered region in the $J_1 - J_d - J_\chi$ model. Specifically, our results indicate that the Case I ansatz is slightly favored for the representation of the CSL, which extended beyond the original classically disordered region on the phase diagram. This case is defined by staggered $\pm\pi/2$ gauge fluxes on the elementary triangles and 0 flux on the hexagons of the Kagome lattice. In addition, by considering the influence of quantum fluctuations to the ordered states found in Chapter 3, a frontier for the phase transition between the CSL and AFM(FM)d phases was established up to the numerical precision of our VMC. The implementation of the Stochastic Reconfiguration[105] in our scheme will increase the accuracy of our variational procedure and it is certainly one investigation that should be addressed in the future. This may furnish a feasible computational time to scale the results with larger system sizes in finite-size scaling analysis, such as the one briefly commented in Chapter 4 for the phase transition between the AFMd and the CSL, for example.

---

[*] The upper bound from a hypothetical gap was determined by experimental data as $10^{-3} J_1$ in a $J_1 - J_d$ Heisenberg model.

Finally, several other investigations can be tackled in future work. The implementation of the Jastrow spin-spin correlation factor, for example, has been shown to improve the energy of the ordered states on the SDW ansatz.[111] Additionally, an implementation of the VMC by using Pfaffian structures instead of the Slater determinant would be ideal to describe a greater variety of physical Ansätze, such as the p-wave superconductor ansatz on the Majorana representation of the Heisenberg model in Appendix C, and also to address cases that are not correctly described by Slater determinants.[94] This would allow the possibility of comparing Z2 QSLs with U(1) CSLs energetically, for example. Finally, our alternatives to describe physical Ansätze could be further augmented by adopting recent tensor network-based methods such as the Matrix Product States/Projected Entangled Pair States (MPS/PEPS) as they can be understood in the context of the Gutzwiller projected wave functions.[92, 93, 130]

REFERENCES

1 YILDIRIM, T.; HARRIS, A. B. Magnetic structure and spin waves in the kagomé jarosite compound $KFe_3 (SO_4)_2 (OH)_6$. **Physical Review B**, v. 73, n. 21, p. 214446, June 2006. DOI: 10.1103/PhysRevB.73.214446.

2 DOMENGE, J.-C. *et al.* Twelve sublattice ordered phase in the $J_1 - J_2$ model on the kagomé lattice. **Physical Review B**, v. 72, n. 2, p. 024433, July 2005. DOI: 10.1103/PhysRevB.72.024433.

3 FÅK, B. *et al.* Kapellasite: a kagome quantum spin liquid with competing interactions. **Physical Review Letters**, v. 109, n. 3, p. 037208, July 2012. DOI: 10.1103/PhysRevLett.109.037208.

4 RAN, Y. *et al.* Projected-wave-function study of the spin-1/2 heisenberg model on the kagomé lattice. **Physical Review Letters**, v. 98, n. 11, Mar. 2007. DOI: 10.1103/PhysRevLett.98.117205.

5 HERMELE, M. *et al.* Properties of an algebraic spin liquid on the kagome lattice. **Physical Review B**, v. 77, n. 22, June 2008. DOI: 10.1103/PhysRevB.77.224413.

6 MARSTON, J. B.; ZENG, C. Spin-peierls and spin-liquid phases of kagomé quantum antiferromagnets. **Journal of Applied Physics**, v. 69, n. 8, p. 5962–5964, 1991. DOI: 10.1063/1.347830.

7 SAVARY, L.; BALENTS, L. Quantum spin liquids: a review. **Reports on Progress in Physics**, v. 80, n. 1, p. 016502, Nov. 2016. DOI: 10.1088%2F0034-4885%2F80%2F1%2F016502.

8 ZHOU, Y.; KANODA, K.; NG, T.-K. Quantum spin liquid states. **Reviews of Modern Physics**, v. 89, n. 2, p. 025003, Apr. 2017. DOI: 10.1103/RevModPhys.89.025003.

9 ANDERSON, P. Resonating valence bonds: a new kind of insulator? **Materials Research Bulletin**, v. 8, n. 2, p. 153–160, 1973.

10 LANDAU, L. The theory of phase transitions. **Nature**, v. 138, n. 3498, p. 840–841, Nov. 1936. DOI: 10.1038/138840a0.

11 WEN, X. **Quantum field theory of many-body systems**: from the origin of sound to an origin of light and electrons. Oxford: Oxford University Press, 2004. (Oxford graduate texts).

12 OLIVIERO, F. G. **Gapless chiral spin liquid from a parton mean-field theory on the kagome lattice**. 2020. Dissertação (Mestrado) — Universidade Federal do Rio Grande do Norte, Natal, 2020. Available from: https://repositorio.ufrn.br/handle/123456789/29974. Accessible at: 23 Jan. 2022.

13 OLIVIERO, F. *et al.* **Noncoplanar magnetic orders and gapless chiral spin liquid in the $J_1 - J_d - J_\chi$ model on the kagome lattice**. 2021. Available from: https://arxiv.org/pdf/2112.03327.pdf. Accessible at: 23 Jan. 2022.

14 LACROIX, C.; MENDELS, P.; MILA, F. (ed.). **Introduction to frustrated magnetism**. Heidelberg: Springer, 2011. DOI: 10.1007/978-3-642-10589-0.

15 HAN, T.-H. *et al.* Fractionalized excitations in the spin-liquid state of a kagome-lattice antiferromagnet. **Nature**, v. 492, n. 7429, p.406–410, Dec. 2012. https://doi.org/10.1038/nature11659.

16 KHUNTIA, P. *et al.* Gapless ground state in the archetypal quantum kagome antiferromagnet $\mathrm{ZnCu_3\,(OH)_6\,Cl_2}$. **Nature Physics**, v. 16, n. 4, p. 469–474, Feb. 2020. DOI: 10.1038/s41567-020-0792-1.

17 KERMARREC, E. *et al.* Spin dynamics and disorder effects in the S = 1/2 kagome Heisenberg spin-liquid phase of kapellasite. **Physical Review B**, v. 90, n. 20, p. 205103, Nov. 2014. DOI:10.1103/PhysRevB.90.205103.

18 MESSIO, L.; LHUILLIER, C.; MISGUICH, G. Lattice symmetries and regular magnetic orders in classical frustrated antiferromagnets. **Physical Review B**, v. 83, n. 18, May 2011. DOI:10.1103/PhysRevB.83.184401.

19 IQBAL, Y. *et al.* Paramagnetism in the kagome compounds (Zn, Mg, Cd) $\mathrm{Cu_3\,(OH)_6}\,Cl_2$. **Physical Review B**, v. 92, n. 22, p. 220404, Dec. 2015. DOI: 10.1103/PhysRevB.92.220404.

20 SEMEGHINI, G. *et al.* Probing topological spin liquids on a programmable quantum simulator. **Science**, v. 374, n. 6572, p. 1242–1247, Dec. 2021. DOI: 10.1126/science.abi8794.

21 SATZINGER, K. J. *et al.* Realizing topologically ordered states on a quantum processor. **Science**, v. 374, n. 6572, p. 1237–1241, Dec. 2021. DOI:10.1126/science.abi8378.

22 AASEN, D. *et al.* Milestones toward majorana-based quantum computing. **Physical Review X**, v. 6, n. 3, Aug. 2016. DOI: 10.1103/PhysRevX.6.031016.

23 WEN, X. G.; WILCZEK, F.; ZEE, A. Chiral spin states and superconductivity. **Physical Review B**, v. 39, p. 11413–11423, June 1989. DOI: 10.1103/PhysRevB.39.11413.

24 BASKARAN, G. Novel local symmetries and chiral-symmetry-broken phases in s=1/2 triangular-lattice heisenberg model. **Physical Review Letters**, v. 63, p. 2524–2527, Nov. 1989. DOI: 10.1103/PhysRevLett.63.2524.

25 BIERI, S.; LHUILLIER, C.; MESSIO, L. Projective symmetry group classification of chiral spin liquids. **Physical Review B**, v. 93, n. 9, p. 094437, Mar. 2016. DOI: 10.1103/PhysRevB.93.094437.

26 KALMEYER, V.; LAUGHLIN, R. B. Equivalence of the resonating-valence-bond and fractional quantum hall states. **Physical Review Letters**, v. 59, p. 2095–2098, Nov. 1987. DOI: 10.1103/PhysRevLett.59.2095.

27 FRADKIN, E. **Field theories of condensed matter physics**. Cambridge: Cambridge University Press, 2013. (Field theories of condensed matter physics). ISBN 9780521764445.

28 KUMAR, K.; SUN, K.; FRADKIN, E. Chiral spin liquids on the kagome lattice. **Physical Review B**, v. 92, n. 9, p. 094433, Sept. 2015. DOI: 10.1103/PhysRevB.92.094433.

29 BAUER, B. *et al.* Chiral spin liquid and emergent anyons in a kagome lattice mott insulator. **Nature Communications**, v. 5, n. 1, Oct. 2014. DOI: 10.1038/ncomms6137.

30 HU, W.-J.; GONG, S.-S.; SHENG, D. N. Variational Monte Carlo study of chiral spin liquid in quantum antiferromagnet on the triangular lattice. **Physical Review B**, v. 94, p. 075131, Aug. 2016. DOI: 10.1103/PhysRevB.94.075131.

31 WIETEK, A.; LÄUCHLI, A. M. Chiral spin liquid and quantum criticality in extended S = 1/2 Heisenberg models on the triangular lattice. **Physical Review B**, v. 95, n. 3, p. 035141, Jan. 2017. DOI: 10.1103/PhysRevB.95.035141.

32 HICKEY, C. *et al.* Emergence of chiral spin liquids via quantum melting of noncoplanar magnetic orders. **Physical Review B**, v. 96, p. 115115, Sept. 2017. DOI: 10.1103/PhysRevB.96.115115.

33 SAADATMAND, S. N.; MCCULLOCH, I. P. Detection and characterization of symmetry-broken long-range orders in the spin-12 triangular Heisenberg model. **Physical Review B**, v. 96, p. 075117, Aug. 2017. DOI: 10.1103/PhysRevB.96.075117.

34 FERRAZ, G. *et al.* Spin chain network construction of chiral spin liquids. **Physical Review Letters**, v. 123, p. 137202, Sept. 2019. DOI: 10.1103/PhysRevLett.123.137202.

35 SEN, D.; CHITRA, R. Large-u limit of a Hubbard model in a magnetic field: chiral spin interactions and paramagnetism. **Physical Review B**, v. 51, p. 1922–1925, Jan. 1995. DOI: 10.1103/PhysRevB.51.1922.

36 KITAMURA, S.; OKA, T.; AOKI, H. Probing and controlling spin chirality in mott insulators by circularly polarized laser. **Physical Review B**, v. 96, p. 014406, July 2017. DOI: 10.1103/PhysRevB.96.014406.

37 CLAASSEN, M. *et al.* Dynamical time-reversal symmetry breaking and photo-induced chiral spin liquids in frustrated mott insulators. **Nature Communications**, v. 8, n. 1, Oct. 2017. DOI: 10.1038/s41467-017-00876-y.

38 QUITO, V. L.; FLINT, R. Floquet engineering correlated materials with unpolarized light. **Physical Review Letters**, v. 126, p. 177201, Apr. 2021.DOI: 10.1103/PhysRevLett.126.177201.

39 TSVELIK, A. M. Simulating exotic phases of matter with bond-directed interactions with arrays of majorana-cooper pair boxes. **Physical Review Letters**, v. 125, p. 197202, Nov. 2020. DOI: 10.1103/PhysRevLett.125.197202.

40 BAUER, B. *et al.* **Gapped and gapless spin liquid phases on the Kagome lattice from chiral three-spin interactions**. 2014. Available from: https://arxiv.org/pdf/1303.6963.pdf. Accessible at: 30 Jan. 2021.

41 PEREIRA, R. G.; BIERI, S. Gapless chiral spin liquid from coupled chains on the kagome lattice. **SciPost Physics**, v. 4, n. 1, p. 004, 2018. Available from: https://scipost.org/SciPostPhys.4.1.004/pdf. Accessible at: 30 Oct. 2020.

42 BAUER, B. *et al.* Symmetry-protected non-fermi liquids, kagome spin liquids, and the chiral kondo lattice model. **Physical Review B**, v. 99, p. 035155, Jan. 2019. DOI: 10.1103/PhysRevB.99.035155.

43 LEE, S.-S. Stability of the u(1) spin liquid with a spinon fermi surface in 2 + 1 dimensions. **Physical Review B**, v. 78, p. 085129, Aug. 2008. DOI: 10.1103/PhysRevB.78.085129.

44 CHUA, V.; YAO, H.; FIETE, G. A. Exact chiral spin liquid with stable spin fermi surface on the kagome lattice. **Physical Review B**, v. 83, p. 180412, May 2011. DOI: 10.1103/PhysRevB.83.180412.

45 LAI, H.-H.; MOTRUNICH, O. I. Su(2)-invariant majorana spin liquid with stable parton fermi surfaces in an exactly solvable model. **Physical Review B**, v. 84, p. 085141, Aug. 2011. DOI: 10.1103/PhysRevB.84.085141.

46 HE, Y.-C.; SHENG, D. N.; CHEN, Y. Chiral spin liquid in a frustrated anisotropic kagome Heisenberg model. **Physical Review Letters**, v. 112, p. 137202, Apr. 2014. DOI: 10.1103/PhysRevLett.112.137202.

47 GONG, S.-S.; ZHU, W.; SHENG, D. N. Emergent chiral spin liquid: fractional quantum hall effect in a kagome Heisenberg model. **Scientific Reports**, v. 4, n. 1, Sept. 2014. DOI: 10.1038/srep06317.

48 WIETEK, A.; STERDYNIAK, A.; LÄUCHLI, A. M. Nature of chiral spin liquids on the kagome lattice. **Physical Review B**, v. 92, p. 125122, Sept. 2015. DOI: 10.1103/PhysRevB.92.125122.

49 GONG, S.-S. *et al.* Global phase diagram of competing ordered and quantum spin-liquid phases on the kagome lattice. **Physical Review B**, v. 91, p. 075112, Feb. 2015. DOI: 10.1103/PhysRevB.91.075112.

50 GONG, S.-S. *et al.* Chiral spin liquid with spinon fermi surfaces in the spin-12 triangular Heisenberg model. **Physical Review B**, v. 100, p. 241111, Dec. 2019. DOI: 10.1103/PHYSREVB.100.241111.

51 SZASZ, A. *et al.* Chiral spin liquid phase of the triangular lattice hubbard model: a density matrix renormalization group study. **Physical Review X**, v. 10, p. 021042, May 2020. DOI: 10.1103/PhysRevX.10.021042.

52 BIERI, S. *et al.* Gapless chiral spin liquid in a kagome Heisenberg model. **Physical Review B**, v. 92, p. 060407, Aug. 2015. DOI: 10.1103/PhysRevB.92.060407.

53 BERNU, B. *et al.* Exchange energies of kapellasite from high-temperature series analysis of the kagome lattice $J_1 - J_2 - J_d$ Heisenberg model. **Physical Review B**, v. 87, p. 155107, Apr. 2013. DOI: 10.1103/PhysRevB.87.155107.

54 GONG, S.-S. *et al.* Emergent quasi-one-dimensionality in a kagome magnet: a simple route to complexity. **Physical Review B**, v. 94, p. 035154, July2016. DOI: 10.1103/PhysRevB.94.035154.

55 CHAIKIN, P.; LUBENSKY, T. **Principles of condensed matter physics**. Cambridge: Cambridge University Press, 2000. ISBN 9781139643054.

56 ZALIZNYAK, I.; LEE, S.-H. Magnetic neutron scattering. *In*: ZHU, Y. (ed.). **Modern techniques for characterizing magnetic materials**. Dordrecht: Kluwer Academic, 2005. p. 3–64. ISBN 1402080077.

57 ZALIZNYAK, I. A.; TRANQUADA, J. M. Neutron scattering and its application to strongly correlated systems. *In*: AVELLA A.; MANCINI F. (ed.). **Strongly correlated systems**. Berlin: Springer, 2014. p. 205-235. (Springer series in solid-state sciences, v. 180). DOI.10.1007/978-3-662-44133-6_7.

58 PRICE, D.; FERNANDEZ-ALONSO, F. **Neutron scattering** - magnetic and quantum phenomena. Berlin: Elsevier Science, 2015. ISBN 9780128020937.

59 LANDAU, L.; LIFSHITZ, E. **Statistical physics**. Berlin: Elsevier Science, 1980. ISBN 9780750633727.

60 KANTOROVICH, L. **Quantum theory of the solid state**: an introduction. Netherlands: Springer, 2004. DOI: 10.1007/978-1-4020-2154-1.

61 MONDAL, K.; KADOLKAR, C. Regular magnetic orders in triangular and kagome lattices. **Journal of Physics**: condensed matter, v. 33, n. 50, p. 505801, Oct. 2021. DOI: 10.1088/1361-648x/ac27d9.

62 IQBAL, Y. *et al.* Gapless spin-liquid phase in the kagome spin-1/2 Heisenberg antiferromagnet. **Physical Review B**, v. 87, p. 060405, Feb. 2013. DOI: 10.1103/PhysRevB.87.060405.

63 MEHTA, P. *et al.* A high-bias, low-variance introduction to machine learning for physicists. **Physics Reports**, v. 810, May 2019. DOI: 10.1016/j.physrep.2019.03.001.

64 LUTTINGER, J. M.; TISZA, L. Theory of dipole interaction in crystals. **Physical Review**, v. 70, p. 954–964, Dec. 1946. DOI: 10.1103/PhysRev.70.954.

65 LUTTINGER, J. M. A note on the ground state in antiferromagnetics. **Physical Review**, v. 81, p. 1015–1018, Mar. 1951. DOI: 10.1103/PhysRev.81.1015.

66 LYONS, D. H.; KAPLAN, T. A. Method for determining ground-state spin configurations. **Physical Review**, v. 120, p. 1580–1585, Dec. 1960. DOI: 10.1103/PhysRev.120.1580.

67 LITVIN, D. The luttinger-tisza method. **Physica**, v. 77, n. 2, p. 205–219, 1974. ISSN 0031-8914.

68 HARRIS, A. B.; KALLIN, C.; BERLINSKY, A. J. Possible néel orderings of the kagomé antiferromagnet. **Physical Review B**, v. 45, p. 2899–2919, Feb. 1992. DOI: 10.1103/PhysRevB.45.2899.

69 LI, W. *et al.* Scaling behavior of entanglement in two- and three-dimensional free-fermion systems. **Physical Review B**, v. 74, p. 073103, Aug. 2006. DOI: 10.1103/PhysRevB.74.073103.

70 ZHANG, Y.; GROVER, T.; VISHWANATH, A. Entanglement entropy of critical spin liquids. **Physical Review Letters**, v. 107, p. 067202, Aug. 2011. DOI: 10.1103/PhysRevLett.107.067202.

71 SWINGLE, B. Entanglement entropy and the fermi surface. **Physical Review Letters**, v. 105, p. 050502, July 2010. DOI: 10.1103/PhysRevLett.105.050502.

72 CÔNSOLI, P. M. *et al.* Heisenberg-kitaev model in a magnetic field: 1/S expansion. **Physical Review B**, v. 102, p. 155134, Oct. 2020. DOI: 10.1103/PhysRevB.102.155134.

73 CÔNSOLI, P. M. **Extended Kitaev magnetism in magnetic fields**. 2020. Dissertation (Master in Science) – Instituto de Física de São Carlos, Universidade de São Paulo, São Carlos, 2020. DOI: 10.11606/d.76.2020.tde-19112020-110752.

74 SANDVIK, A. W.; EVERTZ, H. G. Loop updates for variational and projector quantum Monte Carlo simulations in the valence-bond basis. **Physical Review B**, v. 82, p. 024407, July 2010. DOI: 10.1103/PhysRevB.82.024407.

75 ZETTILI, N. **Quantum mechanics**: concepts and applications. New York: Wiley, 2009. ISBN 9780470026786.

76 WANG, F. Schwinger boson mean field theories of spin liquid states on a honeycomb lattice: Projective symmetry group analysis and critical field theory. **Physical Review B**, v. 82, n. 2, July 2010. DOI: 10.1103/PhysRevB.82.024419.

77 SHE, J.-H.; LAWLER, M. J.; KIM, E.-A. Quantum spin liquid intertwining nematic and superconducting order in Fese. **Physical Review Letters**, v. 121, p. 237002, Dec. 2018. DOI: 10.1103/PhysRevLett.121.237002.

78 SOLYOM, J. **Fundamentals of the physics of solids**. Berlin: Springer, 2010. DOI: 10.1007/978-3-642-04518-9.

79 JOMPOL, Y. *et al.* Probing spin-charge separation in a tomonaga-luttinger liquid. **Science**, v. 325, n. 5940, p. 597–601, 2009.

80 SCHLAPPA, J. *et al.* Probing multi-spinon excitations outside of the twospinon continuum in the antiferromagnetic spin chain cuprate Sr_2CuO_3. **Nature Communications**, v. 9, n. 1, Dec. 2018. DOI: 10.1038/s41467-018-07838-y.

81 GANNON, W. J. *et al.* Spinon confinement and a sharp longitudinal mode in Yb_2Pt_2Pb in magnetic fields. **Nature Communications**, v. 10, n. 1, Mar. 2019. DOI: 10.1038/s41467-019-08715-y.

82 BETHE, H. Zur theorie der metalle. **Zeitschrift für Physik**, v. 71, n. 3, p. 205–226, Mar. 1931. DOI: 10.1007/BF01341708.

83 LIEB, E. H.; WU, F. Y. Absence of mott transition in an exact solution of the short-range, one-band model in one dimension. **Physical Review Letters**, v. 20, p. 1445–1448, June 1968. DOI: 10.1103/PhysRevLett.20.1445.

84 CLOIZEAUX, J.; PEARSON, J. J. Spin-wave spectrum of the antiferromagnetic linear chain. **Physical Review**, v. 128, p. 2131–2135, Dec. 1962. DOI: 10.1103/PhysRev.128.2131.

85 OGUCHI, A.; TSUCHIDA, Y. Spin waves in a one-dimensional Heisenberg antiferromagnet. **Progress of Theoretical Physics**, v. 49, n. 1, p. 76–82, Jan. 1973. DOI: 10.1143/ptp.49.76.

86 GETELINA, J. C. A. **On the critical behavior of the XX spin-1/2 chain under correlated quenched disorder**. 2016. Dissertation (Master in Science) – Instituto de Física de São Carlos, Universidade de São Paulo, São Carlos, 2016. DOI: 10.11606/d.76.2016.tde-14042016-140707.

87 BASKARAN, G.; ANDERSON, P. W. Gauge theory of high-temperature superconductors and strongly correlated fermi systems. **Physical Review B**, v. 37, p. 580–583, Jan. 1988. DOI: 10.1103/PhysRevB.37.580.

88 LEE, P. A.; NAGAOSA, N. Gauge theory of the normal state of high-T_c superconductors. **Physical Review B**, v. 46, p. 5621–5639, Sept.1992. DOI: 10.1103/PhysRevB.46.5621.

89 PEIERLS, R. Zur theorie des diamagnetismus von leitungselektronen. **Zeitschrift fur Physik**, v. 80, n. 11-12, p. 763–791, Nov. 1933. DOI: 10.1007/bf01342591.

90 ORÚS, R. A practical introduction to tensor networks: matrix product states and projected entangled pair states. **Annals of Physics**, v. 349, p. 117–158, Oct. 2014. DOI: 10.1016/j.aop.2014.06.013.

91 CARLEO, G. *et al.* Machine learning and the physical sciences. **Reviews of Modern Physics**, v. 91, p. 045002, Dec. 2019. DOI: 10.1103/RevModPhys.91.045002.

92 WU, Y.-H.; WANG, L.; TU, H.-H. Tensor network representations of parton wave functions. **Physical Review Letters**, v. 124, n. 24, June 2020. DOI: 10.1103/PhysRevLett.124.246401.

93 PETRICA, G. *et al.* Finite and infinite matrix product states for Gutzwiller projected mean-field wave functions. **Physical Review B**, v. 103, p. 125161, Mar. 2021. DOI: 10.1103/PhysRevB.103.125161.

94 MORENO, J. R. *et al.* **Fermionic wave functions from neural-network constrained hidden states**. 2021. Available from: https://arxiv.org/pdf/2111.10420.pdf. Accessible at: 10 Jan. 2022.

95 KITAEV, A. Anyons in an exactly solved model and beyond. **Annals of Physics**, v. 321, n. 1, p. 2–111, 2006.

96 KENT, P. R. C. **Techniques and applications of quantum Monte Carlo**. 1999. Ph.D. Thesis. (Doctor) - University of Cambridge, Cambridge, 1999.

97 CLARK, B. **Variational Monte Carlo notes for Boulder summer school 2010**. 2010. Available from: http://boulderschool.yale.edu/sites/default/files/files/VMC_Final_Notes.pdf. Accessible at: 30 Apr. 2020.

98 LI, T.; YANG, F. Variational study of the neutron resonance mode in the cuprate superconductors. **Physical Review B**, v. 81, p. 214509, June 2010. DOI: 10.1103/PhysRevB.81.214509.

99 FERRARI, F.; BECCA, F. Dynamical structure factor of the $J_1 - J_2$ Heisenberg model on the triangular lattice: magnons, spinons, and gauge fields. **Physical Review X**, v. 9, p. 031026, Aug. 2019. DOI: 10.1103/PhysRevX.9.031026.

100 GROS, C. Physics of projected wavefunctions. **Annals of Physics**, v. 189, n. 1, p. 53-88, 1989.

101 NEWMAN, M.; BARKEMA, G. **Monte Carlo methods in statistical physics**. Oxford: Clarendon Press, 1999. ISBN 9780198517979.

102 METROPOLIS, N. *et al.* Equation of state calculations by fast computing machines. **Journal of Chemical Physics**, v. 21, n. 6, p. 1087–1092, June 1953 DOI:10.1063/1.1699114.

103 HASTINGS, W. K. Monte Carlo sampling methods using markov chains and their applications. **Biometrika**, v. 57, n. 1, p. 97–109, Apr. 1970. DOI: 10.1093/biomet/57.1.97.

104 SORELLA, S. Generalized lanczos algorithm for variational quantum Monte Carlo. **Physical Review B**, v. 64, p. 024512, June 2001. DOI: 10.1103/PhysRevB.64.024512.

105 SORELLA, S. Wave function optimization in the variational Monte Carlo method. **Physical Review B**, v. 71, p. 241103, June 2005. DOI: 10.1103/PhysRevB.71.241103.

106 GUTZWILLER, M. C. Effect of correlation on the ferromagnetism of transition metals. **Physical Review Letters**, v. 10, p. 159–162, Mar. 1963. DOI: 10.1103/PhysRevLett.10.159.

107 WEN, X.-G. Quantum orders and symmetric spin liquids. **Physical Review B** v. 65, p. 165113, Apr. 2002. DOI: 10.1103/PhysRevB.65.165113.

108 YOKOYAMA, H.; SHIBA, H. Hubbard model in strong correlation regime: variational Monte-Carlo studies on singlet liquid and néel state. **Journal of the Physical Society of Japan**, v. 56, n. 10, p. 3570–3581, 1987. DOI: 10.1143/JPSJ.56.3570.

109 YOKOYAMA, H.; SHIBA, H. Variational Monte-Carlo studies of Hubbard model. I. **Journal of the Physical Society of Japan**, v. 56, n. 4, p. 1490–1506, 1987. DOI: 10.1143/JPSJ.56.1490.

110 PRESS, W. *et al.* **Numerical recipes**: the art of scientific computing. 3rd. ed. Cambridge: Cambridge University Press, 2007. ISBN 9780521880688.

111 IQBAL, Y. *et al.* Gutzwiller projected states for the $J_1 - J_2$ Heisenberg model on the kagome lattice: Achievements and pitfalls. **Physical Review B**, v. 104, p. 144406, Oct. 2021. DOI: 10.1103/PhysRevB.104.144406.

112 GEBHARD, F.; VOLLHARDT, D. Correlation functions for hubbard-type models: the exact results for the Gutzwiller wave function in one dimension. **Physical Review Letters**, v. 59, p. 1472–1475, Sept. 1987. DOI: 10.1103/PhysRevLett.59.1472.

113 BARRETEAU, C.; DUCASTELLE, F.; MALLAH, T. A bird's eye view on the flat and conic band world of the honeycomb and kagome lattices: towards an understanding of 2d metal-organic frameworks electronic structure. **Journal of Physics**: condensed matter, v. 29, n. 46, p. 465302, Oct. 2017. DOI: 10.1088%2F1361-648x%2Faa8fec.

114 JESCHKE, H. O.; SALVAT-PUJOL, F.; VALENTÍ, R. First-principles determination of Heisenberg Hamiltonian parameters for the spin-1/2 kagome antiferromagnet $\mathrm{ZnCu_3}\,(OH)_6\,\mathrm{Cl_2}$. **Physical Review B**, v. 88, p. 075106, Aug. 2013. DOI: 10.1103/PhysRevB.88.075106.

115 HASTINGS, M. B. Dirac structure, RVB, and goldstone modes in the kagomé antiferromagnet.**Physical Review B**, v. 63, p. 014413, Dec. 2000. DOI: 10.1103/PhysRevB.63.014413.

116 IQBAL, Y.; POILBLANC, D.; BECCA, F. Vanishing spin gap in a competing spin-liquid phase in the kagome Heisenberg antiferromagnet. **Physical Review B**, v. 89, p. 020407, Jan. 2014. DOI: 10.1103/PhysRevB.89.020407.

117 PEREIRA, R. G. From quantum spin chains to chiral spin liquids. *In*: FERRAZ, A. *et al.* (ed.). **Strongly coupled field theories for condensed matter and quantum information theory**. Cham: Springer International Publishing, 2020. p. 309–323. ISBN 978-3-030-35473-2.

118 NATAF, P. *et al.* Chiral spin liquids in triangular-lattice SU(n) fermionic mott insulators with artificial gauge fields. **Physical Review Letters**, v. 117, p. 167202, Oct. 2016. DOI: 10.1103/PhysRevLett.117.167202.

119 KANG, J. *et al.* **Interplay between tetragonal magnetic order, stripe magnetism, and superconductivity in iron-based materials**. 2014. Available from: https://arxiv.org/pdf/1412.7079.pdf. Accessible at: 23 Jan. 2021.

120 BOTTOU, L. Stochastic gradient descent tricks. *In*: MONTAVON, G.; ORR, G. B.; MÜLLER, K. R. (ed.). **Neural networks**: tricks of the trade. 2nd ed. Berlin: Springer, 2012. p. 421–436. DOI: 10.1007/978-3-642-35289-8_25.

121 RUMELHART, D. E.; HINTON, G. E.; WILLIAMS, R. J. Learning representations by back-propagating errors. **Nature**, v. 323, n. 6088, p. 533–536, Oct. 1986. DOI: 10.1038/323533a0.

122 PITTS, J. **Order by disorder in classical kagome antiferromagnets with chiral interactions**. 2020. Ph. D. Thesis. (Doctor in Phisics) - University of California, Riverside, 2020.

123 VILLAIN, J. *et al.* Order as an effect of disorder. **Journal de Physique (Paris)**, v. 41, n. 11, p. 1263-1272, 1980.

124 HENLEY, C. L. Ordering due to disorder in a frustrated vector antiferromagnet. **Physical Review Letters**, v. 62, n.17, p. 2056, Apr. 1989.

125 SHENDER, E. Antiferromagnetic garnets with fluctuationally interacting sublattices. **Sovietic Physics JETP**, v. 56, n. 1, p. 178, 1982.

126 MIRANDA, M. M. J. **Mecanismo de campo-aleatório induzido por diluição de acoplamentos em um modelo de Heisenberg frustrado**. 2020. 67 p. Dissertação (Mestrado em Ciências) – Instituto de Física de São Carlos, Universidade de São Paulo, São Carlos, 2020.

127 KRÜGER, W. G. F.; JANSSEN, L. Nesting instability of gapless U(1) spin liquids with spinon fermi pockets in two dimensions. **Physical Review B**, v. 104, p. 165133, Oct. 2021. DOI: 10.1103/PhysRevB.104.165133.

128 ZHU, W. *et al.* Entanglement signatures of emergent Dirac fermions: Kagome spin liquid and quantum criticality. **Science Advances**, v. 4, n. 11, p. eaat5535, 2018. DOI: 10.1126/sciadv.aat5535.

129 CÔNSOLI, P. M.; ANDRADE, E. C. **Stability of ordered and disordered phases in the Heisenberg-Kitaev model in a magnetic field**. 2021. Available from: https://arxiv.org/pdf/2111.11474.pdf. Accessible at: 23 Jan. 2022.

130 HASIK, J. *et al.* **Simulating chiral spin liquids with projected entangled-pair states**. 2022. Available from: https://arxiv.org/pdf/2201.07758.pdf. Accessible at: 30 jan. 2022.

131 SHERMAN, J.; MORRISON, W. J. Adjustment of an inverse matrix corresponding to a change in one element of a given matrix. **Annals of Mathematical Statistics**, v. 21, n. 1, p. 124-127, 1950. DOI: 10.1214/aoms/1177729893.

132 HALDANE, F. D. M. Exact Jastrow-Gutzwiller resonating-valence-bond ground state of the spin-1/2 antiferromagnetic Heisenberg chain with $1/r^2$ exchange. **Physical Review Letters**, v. 60, p. 635–638, Feb. 1988. DOI: 10.1103/PhysRevLett.60.635.

133 SHASTRY, B. S. Exact solution of an s=1/2 Heisenberg antiferromagnetic chain with long-ranged interactions. **Physical Review Letters**, v. 60, p. 639–642, Feb. 1988. DOI: 10.1103/PhysRevLett.60.639.

134 SHASTRY, B. S.; SEN, D. Majorana fermion representation for an antiferromagnetic spin- chain. **Physical Review B**, v. 55, p. 2988–2994, Feb. 1997. DOI: 10.1103/PhysRevB.55.2988.

135 SEIFERT, U. F. P.; MENG, T.; VOJTA, M. Fractionalized fermi liquids and exotic superconductivity in the kitaev-kondo lattice. **Physical Review B**, v. 97, p. 085118, Feb. 2018. DOI: 10.1103/PhysRevB.97.085118.

136 SEIFERT, U. **Novel phases and light-induced dynamics in quantum magnets**. 2019. Ph. D. Thesis (Doctor) — Institut für Theoretische Physik, Technische Universität Dresden, Dresden, 2019. Available from: https://tud.qucosa.de/api/qucosa%3A36749/attachment/ATT-0/. Accessible at: 23 Jan. 2020.

137 COLEMAN, P.; MIRANDA, E.; TSVELIK, A. Possible realization of odd-frequency pairing in heavy fermion compounds. **Physical Review Letters**, v. 70, p. 2960–2963, May 1993. DOI: 10.1103/PhysRevLett.70.2960.

138 RIPKA, S.; BLAIZOT, J.; RIPKA, G. **Quantum theory of finite systems**. Cambridge: MIT Press, 1986. ISBN 9780262022149.

139 KNOLLE, J. **Dynamics of a quantum spin liquid**. Cham: Springer, 2016. (Springer theses). ISBN 9783319239538.

140 MISAWA, T. *et al.* MVMC: open-source software for many-variable variational Monte Carlo method. **Computer Physics Communications**, v. 235, p. 447–462, Feb. 2019. DOI: 10.1016/j.cpc.2018.08.014.

141 MOTRUNICH, O. I. Orbital magnetic field effects in spin liquid with spinon fermi sea: possible application to $\kappa-(\mathrm{ET})_2\,\mathrm{Cu}_2(\mathrm{CN})_3$. **Physical Review B**, v. 73, p. 155115, Apr. 2006. DOI:10.1103/PhysRevB.73.155115.

Appendix

APPENDIX A – VMC APPENDIX

A.1 Matrix Determinant Lemma

Lemma 1. *Consider an invertible square matrix* $\mathbb{A} \in \mathbb{R}^{n\times n}$*, and the column vectors* $\boldsymbol{u}, \boldsymbol{v} \in \mathbb{R}^n$*. The matrix determinant lemma*[110] *states that*

$$\det\left(\mathbb{A} + \boldsymbol{u}\boldsymbol{v}^T\right) = \left(1 + \boldsymbol{v}^T\mathbb{A}^{-1}\boldsymbol{u}\right). \tag{A.1}$$

Proof.

$$\begin{aligned} \det\left(\mathbb{A} + \boldsymbol{u}\boldsymbol{v}^T\right) &= \det\left(\mathbb{A}\left(\mathbb{I} + \left(\mathbb{A}^{-1}\boldsymbol{u}\right)\boldsymbol{v}^T\right)\right) = \det(\mathbb{A})\det\left(\mathbb{I} + \left(\mathbb{A}^{-1}\boldsymbol{u}\right)\boldsymbol{v}^T\right) \\ &= \det(\mathbb{A})\left(1 + \boldsymbol{v}^T\left(\mathbb{A}^{-1}\boldsymbol{u}\right)\right). \end{aligned} \tag{A.2}$$

For the second equality we used Sylvester's determinant theorem with $\det(\mathbb{I} + \mathbb{A}\mathbb{B}) = \det(\mathbb{I} + \mathbb{B}\mathbb{A})$. ■

A.2 Shermann-Morrison Formula

Formula 1. *Consider an invertible square matrix* $\mathbb{A} \in \mathbb{R}^{n\times n}$*, and the column vectors* $\boldsymbol{u}, \boldsymbol{v} \in \mathbb{R}^n$*. Then* $\mathbb{A} + \boldsymbol{u}\boldsymbol{v}^T$ *is invertible if* $\left(1 + \boldsymbol{v}^T\mathbb{A}^{-1}\boldsymbol{u}\right) \neq 0$*. The Sherman-Morrison*[110, 131] *formula states that*

$$\left(\mathbb{A} + \boldsymbol{u}\boldsymbol{v}^T\right)^{-1} = \mathbb{A}^{-1} - \frac{\mathbb{A}^{-1}\boldsymbol{u}\boldsymbol{v}^T\mathbb{A}^{-1}}{1 + \boldsymbol{v}^T\mathbb{A}^{-1}\boldsymbol{u}}. \tag{A.3}$$

Proof.

$$\begin{aligned} \left(\mathbb{A} + \boldsymbol{u}\boldsymbol{v}^T\right)^{-1} &= \mathbb{A}^{-1}\left(\mathbb{I} + \mathbb{A}^{-1}\boldsymbol{u}\boldsymbol{v}^T\right) \\ &= \mathbb{A}^{-1}\left(1 - \mathbb{A}^{-1}\boldsymbol{u}\boldsymbol{v}^T + \mathbb{A}^{-1}\boldsymbol{u}\boldsymbol{v}^T\mathbb{A}^{-1}\boldsymbol{u}\boldsymbol{v}^T - \dots\right) \\ &= \mathbb{A}^{-1} - \mathbb{A}^{-1}\boldsymbol{u}\boldsymbol{v}^T\mathbb{A}^{-1}\left(1 - \lambda + \lambda^2 - \lambda^3 + \dots\right) \\ &= \mathbb{A}^{-1} - \frac{\mathbb{A}^{-1}\boldsymbol{u}\boldsymbol{v}^T\mathbb{A}^{-1}}{1 + \lambda}. \end{aligned} \tag{A.4}$$

with

$$\lambda = \boldsymbol{v}^T\mathbb{A}^{-1}\boldsymbol{u}. \tag{A.5}$$

The second and fourth lines are obtained by considering the geometric series. In the third line, the associativity of the products is used to factor out the scalar λ.[110] ■

APPENDIX B – HALDANE-SHASTRY MODEL

Is there any physical model for which the GPW is an exact eigenstate? This would be another good benchmark test and interesting physical example for the developed Variational Monte Carlo. In this Subsection our interest will reside on a numerical exploration of the GSE of the Haldane-Shastry Model,[132,133] which has the GPW as an exact eigenstate. The interactions have a particular long-range interaction in the Hamiltonian[92]

$$\mathcal{H}_{HS} = \sum_{p<q} \frac{J\pi^2 \boldsymbol{S}_p \cdot \boldsymbol{S}_q}{N^2 \sin^2 \frac{\pi}{N}(p-q)} = \frac{1}{2}\sum_{p=1}^{N}\sum_{q=1}^{N-1} \frac{J\pi^2 \boldsymbol{S}_p \cdot \boldsymbol{S}_q}{N^2 \sin^2 \frac{\pi}{N}(p-q)}, \tag{B.1}$$

with the ground-state energy and spin-spin correlation function given by[92]

$$E^0_{HS} = -J\frac{\pi^2}{24}\left(N + \frac{5}{N}\right) \tag{B.2}$$

and

$$\langle \boldsymbol{S}_p \cdot \boldsymbol{S}_q \rangle = \frac{\sum_{a=1}^{N/2} \frac{3(-1)^q}{2a-1} \sin\left(\frac{\pi}{N}(2a-1)\,q\right)}{2N \sin \frac{\pi}{N} q}. \tag{B.3}$$

In the limit of $N \gg 1$ the expressions can be implemented numerically identically as in the Heisenberg model, with the correction of a factor $|p-q|^{-2}$ at the denominator of the energy expression

$$\mathcal{H}_{HS} = \frac{1}{2}\sum_{p=1}^{N}\sum_{q=1}^{N-1} \frac{J \boldsymbol{S}_p \cdot \boldsymbol{S}_q}{|p-q|^2}, \tag{B.4}$$

and $\langle \boldsymbol{S}_p \cdot \boldsymbol{S}_q \rangle = \frac{3}{4}(-1)^q$, which is numerically the same as (2.67) apart from a factor of 3 from the contribution for the 3 components of the expected value $S^x_p S^x_q$, $S^y_p S^y_q$ and $S^z_p S^z_q$. Consequently, Figure 10 is also representative for the Haldane-Shastry model in this limit.

Table 7 – Ground state energy for the Haldane-Shastry model using the GPW for different numbers of spins N. The second column represents the exact values from equation (B.2), whereas the third column contains the results obtained within the VMC.

N	E^0_{HS}/JN	E_0/JN
32	−0.413 241 492	−0.413 241 492 (3)
64	−0.411 735 510	−0.411 735 510 (2)
96	−0.411 456 625	−0.411 456 625 (2)
128	−0.411 359 015	−0.411 359 015 (2)
256	−0.411 264 891	−0.411 264 891 (2)
512	−0.411 241 360	−0.411 241 358 (2)

Source: By the author.

The results for the VMC can be seen in Table 7, and compared with the respective expected value as assigned by equation (B.2). Each program execution takes 5.0×10^3 MC sweeps to thermalize and 100 energy values are stored. This was repeated for 10 different random seeds and an average was performed in the end. The third column indicates the results obtained with the GPW within the VMC, evidencing that indeed the GSE for the Haldane-Shastry model can be well described up to the numerical precision of our VMC implementation.

APPENDIX C – FERMIONIC MAJORANA REPRESENTATION

Another possibility of representing the fractionalized degrees of freedom of a QSL is to adopt the so-called Majorana fermion formalism.[42,134,135] The Majorana fermions are the same particles proposed as real solutions to the Dirac equation and have gained recent attention after the proposal of their manipulation for potential topological quantum computing.[22] Although they have different representations explored in the literature obeying the SU(2) spin algebra (2.20), recently Seifert, Meng and Vojta[135,136] introduced an interesting representation of the Majoranas, which relates earlier different representations by an adjustable parameter η such that the spin operator is given by

$$S_{\eta}^{\alpha} = (1+\eta)\,\frac{i}{2}\chi^{0}\chi^{\alpha} - (1-\eta)\,\frac{i}{4}\epsilon^{\alpha\beta\gamma}\chi^{\beta}\chi^{\gamma}, \tag{C.1}$$

with the four Majorana fermions χ_i^{α} (i being a site index) obeying the anticommutation relations

$$\left\{\chi_i^{\mu},\chi_j^{\nu}\right\} = \delta^{\mu\nu}\delta_{ij}, \quad \chi_i^{\mu} = \chi_i^{\mu\dagger} \quad \text{with} \quad (\mu,\nu = 0,1,2,3)\,. \tag{C.2}$$

For this Subsection we shall focus on the representation with $\eta = 1$,[135] which is equivalent to the Majorana formalism implemented for Kitaev's spin liquid.[95] In this representation we have a direct relation with the Dirac fermions given by the Abrikosov representation via the equations

$$f_{i\uparrow} = \frac{(\chi_i^0 + i\chi_i^3)}{\sqrt{2}} \quad , \quad f_{i\downarrow} = \frac{(i\chi_i^1 - \chi_i^2)}{\sqrt{2}} \tag{C.3}$$

and

$$f_{i\uparrow}^{\dagger} = \frac{(\chi_i^0 - i\chi_i^3)}{\sqrt{2}} \quad , \quad f_{i\downarrow}^{\dagger} = \frac{(-i\chi_i^1 - \chi_i^2)}{\sqrt{2}}. \tag{C.4}$$

These can be inverted, giving the Majorana fermions a representation in terms of the Abrikosov ones

$$\begin{cases} \chi_i^0 = \frac{f_{i\uparrow}+f_{i\uparrow}^{\dagger}}{\sqrt{2}} \\ \chi_i^1 = \frac{f_{i\downarrow}-f_{i\downarrow}^{\dagger}}{\sqrt{2}i} \\ \chi_i^2 = \frac{-f_{i\downarrow}-f_{i\downarrow}^{\dagger}}{\sqrt{2}} \\ \chi_i^3 = \frac{f_{i\uparrow}-f_{i\uparrow}^{\dagger}}{\sqrt{2}i} \end{cases} . \tag{C.5}$$

From these relations it is clear to understand that Majorana fermions are Hermitian operators (C.2). This representation needs a physical constraint in order to recover the physical Hilbert space of localized spins which is given by

$$D = 4\chi_i^0\chi_i^1\chi_i^2\chi_i^3 = 1. \tag{C.6}$$

Additionally, it can be shown that this constraint is generated by the single-occupancy constraint (2.21) used in the Abrikosov representation[135]

$$0 = n_{i\uparrow} + n_{i\downarrow} - 1 = i\chi_i^0\chi_i^3 + i\chi_i^1\chi_i^2. \tag{C.7}$$

Therefore, if the constraint is obeyed on each site, the four-flavor Majorana representation for the spin operator is valid and given by

$$S_i^\alpha = i\chi_i^0\chi_i^\alpha \tag{C.8}$$

for $\alpha = 1, 2, 3$.

We can proceed our treatment to the mean-field theory of the Heisenberg Hamiltonian by using the Majorana spin representation (C.8) by casting it into the form

$$\mathcal{H} = -J\sum_{\langle i,j\rangle}\left[\left(i\chi_i^0\chi_j^0\right)\left(i\chi_i^1\chi_j^1\right) + \left(i\chi_i^0\chi_j^0\right)\left(i\chi_i^2\chi_j^2\right) + \left(i\chi_i^0\chi_j^0\right)\left(i\chi_i^3\chi_j^3\right)\right]. \tag{C.9}$$

The mean-field decomposition is obtained by neglecting quadratic fluctuations in the link variables $u^0 = \left\langle i\chi_i^0\chi_j^0\right\rangle$ and $u^\alpha = \left\langle i\chi_i^\alpha\chi_j^\alpha\right\rangle$ for $\alpha = 1, 2, 3$, in

$$\begin{aligned} i\chi_i^0\chi_j^0 i\chi_i^\alpha\chi_j^\alpha &= \left\langle i\chi_i^0\chi_j^0\right\rangle i\chi_i^\alpha\chi_j^\alpha + i\chi_i^0\chi_j^0\left\langle i\chi_i^\alpha\chi_j^\alpha\right\rangle - \left\langle i\chi_i^0\chi_j^0\right\rangle\left\langle i\chi_i^\alpha\chi_j^\alpha\right\rangle = \\ &= u^0 i\chi_i^\alpha\chi_j^\alpha + i\chi_i^0\chi_j^0 u^\alpha - u^0u^\alpha. \end{aligned}$$

We note that for any two Majorana operators, the expectation value $\left\langle i\chi^\beta\chi^\nu\right\rangle^* = \left\langle -i\chi^\nu\chi^\beta\right\rangle = \left\langle i\chi^\beta\chi^\nu\right\rangle$ is always real[136] since the Majoranas are Hermitian. The mean-field Heisenberg Hamiltonian becomes then

$$\mathcal{H} = -J\sum_{\alpha\langle i,j\rangle}\left[u^0 i\chi_i^\alpha\chi_j^\alpha + i\chi_i^0\chi_j^0 u^\alpha - u^0u^\alpha\right]. \tag{C.10}$$

Example: AFM Heisenberg model in 1D

We consider once again the S=1/2 AFM Heisenberg model in one dimension. The translational invariance can be cautiously explored by noting that we must sum half the Brillouin zone momentum values in order to count the degrees of freedom correctly.[137] Therefore, the Fourier decomposition from

$$\chi_k^\alpha = \frac{1}{\sqrt{N}}\sum_j \chi_j^\alpha e^{-ikx_j} \tag{C.11}$$

and the condition (which can be understood from the previous equation) $\chi_{k,i}^\alpha = \chi_{-k,i}^{\dagger\alpha}$ generate

$$\chi_j^\alpha = \frac{1}{\sqrt{N}}\sum_{k>0}\left\{\chi_k^\alpha e^{ikx_j} + \chi_k^{\dagger\alpha} e^{-ikx_j}\right\}. \tag{C.12}$$

Naturally, these expressions are essential to build the anticommutation rules in the momentum space for Majorana operators given by

$$\left\{\chi_k^\alpha, \chi_{k'}^{\dagger\alpha}\right\} = \frac{1}{N}\sum_{i,j} e^{-ikx_i + ik'x_j}\left\{\chi_i^\alpha, \chi_j^{\dagger\alpha}\right\} = \frac{1}{N}\sum_i e^{ix_i(k'-k)} = \delta_{k,k'}. \tag{C.13}$$

From these considerations, the Hamiltonian can finally be cast into a quadratic form

$$\mathcal{H} = -J \textstyle\sum_{\alpha,k>0} \Big\{ u^0 i \Big[\chi_k^{\alpha} \chi_{-k}^{\alpha} e^{-ik} + \chi_k^{\alpha} \chi_k^{\dagger\alpha} e^{-ik} + \chi_k^{\dagger\alpha} \chi_k^{\alpha} e^{ik} + \chi_k^{\dagger\alpha} \chi_{-k}^{\dagger\alpha} e^{ik} \Big] +$$

$$+ i \Big[\chi_k^{0} \chi_{-k}^{0} e^{-ik} + \chi_k^{0} \chi_k^{\dagger 0} e^{-ik} + \chi_k^{\dagger 0} \chi_k^{0} e^{ik} + \chi_k^{\dagger 0} \chi_{-k}^{\dagger 0} e^{ik} \Big] u^{\alpha} - u^0 u^{\alpha} \Big\} .$$

The Fourier transform generates complex fermions. This can be further rearranged as

$$\mathcal{H} = J \sum_{\alpha,k>0} \Big\{ 4 \sin k \left(u^0 \chi_k^{\dagger\alpha} \chi_k^{\alpha} + \chi_k^{\dagger 0} \chi_k^{0} u^{\alpha} \right) - 2 i e^{-ik} \left(u^0 + u^{\alpha} \right) \Big\} + J z N u^0 u^{\alpha}. \tag{C.14}$$

The ground state energy is then given by integrating the dispersion relation in half the BZ [*]

$$\begin{aligned} \frac{E_0}{JN} &= \frac{4}{N} \frac{N}{2\pi} \sum_{\alpha} \left(u^0 + u^{\alpha} \right) \int_0^{\pi} \left[\sin k - \frac{i e^{-ik}}{2} \right] dk + \sum_{\alpha} 2 u^0 u^{\alpha} = \\ &= \sum_{\alpha} 2 \left[\frac{(u^0 + u^{\alpha})}{\pi} + u^0 u^{\alpha} \right] . \end{aligned} \tag{C.15}$$

By minimizing this equation with respect to u^{α} and u^0 and assuming that u^{α} is the same for $\alpha = 1, 2, 3$ in the isotropic coupling case, the minimum mean field parameters $u^0 = -2/\pi$ and $u^{\alpha} = -2/3\pi$ are found and furnish the ground state energy of

$$\frac{E_0}{JN} = 2 \left[\frac{(u^0 + 3u^{\alpha})}{\pi} + 3 u^0 u^{\alpha} \right] = -\frac{4}{3\pi^2} \approx -0.13509. \tag{C.16}$$

This is a smaller result in comparison with the one obtained via the Abrikosov representation, $(E_0/JN)_A \approx 0.19934$, although it is still far from the exact value given by Bethe's ansatz $(E_0/JN)_B \approx -0.44315$. These results exemplify that independent of the specific spin representation used in decoupling the degrees of freedom of the QSL, imposing a single-occupancy constraint exactly by the Gutzwiller projection remains an important aspect for representing a QSL.

The difference from the ground state energy for each case can be understood intuitively as a consequence of the band structure and the fermionic statistics for both representations. The Majorana representation usually shows linear dispersion near the zero energy point. Therefore, we consider a linear density of states in a first approximation. We also remember that the MFT obtained directly after decoupling the Heisenberg Hamiltonian with the Abrikosov fermions was a free fermion's theory, and we consider a constant density of states. Consequently, considering the normalization condition for the density of states for the Metal and Dirac-Cone dispersion type material cases, respectively,

---

[*] Different from the direct Abrikosov decoupling approach for the Heisenberg Hamiltonian that we explored in Subsection 2.2.1, here we integrate for $k : 0 \to \pi$ instead of $k : -\frac{\pi}{2} \to \frac{\pi}{2}$. It is a convention to work only with positive majoranas, taking correctly only half of the BZ.[134, 136, 137]

$$1 = \int_{-W}^{W} \rho\left(E\right) dE \Rightarrow \begin{cases} \rho_{\mathrm{ABR}}\left(E\right) = \frac{1}{2W} \\ \rho_{\mathrm{MAJ}}\left(E\right) = \frac{1}{W^2}\left|E\right| \end{cases} . \tag{C.17}$$

For the mean ground state energy, we integrate it from $-W$ (where W is the bandwidth) to 0 due to the half-filling condition,

$$\left\langle E\right\rangle = \int_{-W}^{0} E\rho\left(E\right) dE \Rightarrow \begin{cases} \left\langle E\right\rangle_{\mathrm{ABR}} = -\frac{W^2}{4W} = -\frac{W}{4} \\ \left\langle E\right\rangle_{\mathrm{MAJ}} = -\frac{W^3}{3W^2} = -\frac{W}{3} \end{cases} , \tag{C.18}$$

and we confirm that Majoranas usually have a better estimate for the ground state energy in the mean field treatment.

After the decoupling procedure is there any difference in the mean-field Hamiltonian if we express the Majorana fermions in terms of complex fermions? To answer this question, we consider the decoupled Majorana Hamiltonian (C.10) with the Abrikosov correspondence given by equations (C.5). This gives the expression

$$\begin{aligned} \mathcal{H} = -J \sum_{\langle i,j\rangle} &\left[u^0 i\left(f_{i\downarrow} f^\dagger_{j\downarrow} + f^\dagger_{i\downarrow} f_{j\downarrow}\right) + i\left(\frac{3u}{2} - \frac{u_0}{2}\right)\left[f_{i\uparrow} f^\dagger_{j\uparrow} + f^\dagger_{i\uparrow} f_{j\uparrow}\right]\right] + \\ &+ \sum_{\langle i,j\rangle}\left[i\left(\frac{3u}{2} - \frac{u_0}{2}\right)\left[f_{i\uparrow} f_{j\uparrow} - \mathrm{h.c.}\right] - 3u^0 u\right]. \end{aligned} \tag{C.19}$$

Using the momentum space representation of the fermionic operators (2.34) and the anticommutation relations (2.24) the Hamiltonian can be further simplified as

$$\mathcal{H} = J\sum_k \left[\epsilon_\downarrow\left(k\right) f^\dagger_{k\downarrow} f_{k\downarrow} + \epsilon_\uparrow\left(k\right) f^\dagger_{k\uparrow} f_{k\uparrow}\right] + \frac{J}{2}\sum \left[\Delta^*_k f_{k\uparrow} f_{-k\uparrow} + \Delta_k f^\dagger_{-k\uparrow} f^\dagger_{k\uparrow}\right] + \mathcal{H}_0 \tag{C.20}$$

with

$$\Delta_k = i\left(3u - u_0\right) e^{ik}, \quad \epsilon_\downarrow\left(k\right) = 2u_0 \sin k, \qquad \epsilon_\uparrow\left(k\right) = \left(3u - u_0\right)\sin k \tag{C.21}$$

and

$$\mathcal{H}_0 = J\sum_k \left[3u^0 u - ie^{-ik}\frac{3}{2}\left(u_0 + u\right)\right]. \tag{C.22}$$

This functional form resembles a p-wave superconductor with $\Delta_k = -\Delta^*_{-k}$, i.e., a superconductor with triplet excitations and a explicit dependence of the k-vector on the gap function. We cast the Hamiltonian into a matrix form

$$\mathcal{H} = \frac{1}{2} J\sum_k \Psi^\dagger_k H_p \Psi_k + \frac{1}{2} J\sum_k \varepsilon_\uparrow\left(k\right) + \mathcal{H}_\downarrow + \mathcal{H}_0 \tag{C.23}$$

with the spinor

$$\Psi^\dagger = \begin{pmatrix} f^\dagger_{k\uparrow} & f_{-k\uparrow} \end{pmatrix} \tag{C.24}$$

and the matrix

$$H_p = \begin{pmatrix} \epsilon_\uparrow\left(k\right) & -\Delta_k \\ -\Delta^*_k & \epsilon_\uparrow\left(-k\right) \end{pmatrix}. \tag{C.25}$$

The eigenvalues are then given by[138, 139]

$$E\left(k\right)=\left\{\begin{array}{c}\epsilon_{\uparrow}\left(k\right)=-\left(3u-u_{0}\right)+\left(3u+u_{0}\right)\sin k\\ \epsilon_{\downarrow}\left(k\right)=\left(3u-u_{0}\right)+\left(3u+u_{0}\right)\sin k\end{array}\right. . \tag{C.26}$$

Finally, the diagonal Hamiltonian can represented in the quasiparticle basis and separated in terms of each spin flavor as

$$\begin{aligned}\mathcal{H}_{\uparrow}&=\frac{1}{2}J\sum_{k}E\left(k\right)\Psi_{k}^{\dagger}\Psi_{k}+\frac{1}{2}J\sum_{k}\varepsilon_{\uparrow}\left(-k\right)+J\sum_{k}\left[3u^{0}u-ie^{-ik}\frac{3}{2}\left(u_{0}+u\right)\right],\\ \mathcal{H}_{\downarrow}&=J\sum_{k}\epsilon_{\downarrow}\left(k\right)f_{k\downarrow}^{\dagger}f_{k\downarrow}.\end{aligned} \tag{C.27}$$

The ground state energy is then given by

$$\begin{aligned}\left(\frac{E_{0}}{JN}\right)=\frac{2}{N}\frac{N}{2\pi}2\left(3u+u_{0}\right)\int_{0}^{\pi}\left(\sin k\right)dk+\frac{1}{N}\frac{N}{2\pi}\left[\frac{1}{2}\left(3u-u_{0}\right)+\right.\\ \left.+2u_{0}\right]\int_{0}^{\pi}\sin kdk+3zu^{0}u^{\alpha}-\frac{1}{N}\frac{N}{2\pi}\int_{0}^{\pi}ie^{-ik}\frac{3}{2}\left(u_{0}+u\right)\end{aligned} \tag{C.28}$$

or

$$\left(\frac{E_{0}}{JN}\right)=\left(\frac{E_{0}}{JN}\right)=6u^{0}u+\frac{2}{\pi}\left(u+u^{0}\right) \tag{C.29}$$

which is exactly the same result as in equation (C.15). Therefore, after the mean-field decoupling, the Majorana and its correspondent Abrikosov representations are equivalent when considering the ground state energy observable. A similar comparison between both representations was done for the Kitaev Model, and after the physical decoupling, a mean-field analysis was shown to be equivalent for both cases.[136] In this reference, it is also discussed that different MFTs may introduce distinct phase diagrams. Therefore, the particular spin representation in the Parton construction for a physical problem needs to be chosen cautiously after comparison with distinct methodologies, such as exactly solvable models or numerical results, based on a universal physics which must be captured in the fractionalized representation.

In the context of a Majorana decoupling of the Heisenberg Hamiltonian we have seen that a p-wave superconductor MFT appears. From a numerical perspective, this implicates major modifications on the main part of the VMC developed in this dissertation since the wave function that describes p-wave superconductor phases is based on a Pfaffian construction instead of Slater determinants.[140] Indeed, Pfaffian wave functions can be shown to be more general in the sense that they can still encompass the Slater determinant Ansätze as well as special cases that represent superconducting phases Ansätze, for example.

APPENDIX D – CHIRAL INTERACTION

In this Appendix, we derive equation (2.95) with more detail and present one example on how to obtain the diagrams in Table 5. We reconsider the spin ladder operators

$$\begin{cases} S_i^+ = f_{i\uparrow}^\dagger f_{i\downarrow} = S_i^x + iS_i^y \\ S_i^+ = f_{i\downarrow}^\dagger f_{i\uparrow} = S_i^x - iS_i^y \end{cases} \tag{D.1}$$

and

$$\begin{cases} S_i^x = \frac{S_i^+ + S_i^-}{2} = \frac{f_{i\uparrow}^\dagger f_{i\downarrow} + f_{i\downarrow}^\dagger f_{i\uparrow}}{2} \\ S_i^y = \frac{S_i^+ - S_i^-}{2i} = \frac{f_{i\uparrow}^\dagger f_{i\downarrow} - f_{i\downarrow}^\dagger f_{i\uparrow}}{2i} \\ S_i^z = \frac{\left(n_{i\uparrow} - n_{i\downarrow}\right)}{2} \end{cases} . \tag{D.2}$$

Using these operators, the chiral interaction in one up triangle (△),[23,27]

$$E_{123} = \mathbf{S}_1 \cdot (\mathbf{S}_2 \times \mathbf{S}_3) = S_1^x S_2^y S_3^z - S_1^x S_2^z S_3^y - S_1^y S_2^x S_3^z + S_1^y S_2^z S_3^x + S_1^z S_2^x S_3^y - S_1^z S_2^y S_3^x \tag{D.3}$$

can be rewritten as

$$\begin{aligned} E_{123} = \frac{1}{8i} \Big\{ &\left[\left(S_1^+ - S_1^-\right)\left(S_3^+ + S_3^-\right) - \left(S_1^+ + S_1^-\right)\left(S_3^+ - S_3^-\right) \right] (n_{2\uparrow} - n_{2\downarrow}) + \\ &+ \left[\left(S_1^+ + S_1^-\right)\left(S_2^+ - S_2^-\right) - \left(S_1^+ - S_1^-\right)\left(S_2^+ + S_2^-\right) \right] (n_{3\uparrow} - n_{3\downarrow}) + \\ &+ \left[\left(S_2^+ + S_2^-\right)\left(S_3^+ - S_3^-\right) - \left(S_2^+ - S_2^-\right)\left(S_3^+ + S_3^-\right) \right] (n_{1\uparrow} - n_{1\downarrow}) \Big\} . \end{aligned} \tag{D.4}$$

Before proceeding further, we quickly observe that using the anti-commutation relations relations (2.24), the following properties can be derived

$$\left\{ n_{i\tau}, S_j^+ \right\} = 0 \quad \text{and} \quad \left\{ n_{i\tau}, S_j^- \right\} = 0. \tag{D.5}$$

Proof.

$$\begin{gathered} \left\{ n_{i\tau}, S_j^+ \right\} = \left\{ f_{i\tau}^\dagger f_{i\tau}, f_{j\uparrow}^\dagger f_{j\downarrow} \right\} = \left\{ f_{i\tau}^\dagger, f_{j\uparrow}^\dagger f_{j\downarrow} \right\} f_{i\tau} + f_{i\tau}^\dagger \left\{ f_{i\tau}, f_{j\uparrow}^\dagger f_{j\downarrow} \right\} = \\ = \left[\left\{ f_{i\tau}^\dagger, f_{j\uparrow}^\dagger \right\} f_{j\downarrow} f_{i\tau} + f_{j\uparrow}^\dagger \left\{ f_{i\tau}^\dagger, f_{j\downarrow} \right\} f_{i\tau} \right] + \left[f_{i\tau}^\dagger \left\{ f_{i\tau}, f_{j\uparrow}^\dagger \right\} f_{j\downarrow} + f_{i\tau}^\dagger f_{j\uparrow}^\dagger \left\{ f_{i\tau}, f_{j\downarrow} \right\} \right] = \\ = -f_{j\uparrow}^\dagger f_{i\tau} \delta_{ij} \delta_{\tau\downarrow} + f_{i\tau}^\dagger f_{j\downarrow} \delta_{ij} \delta_{\tau\uparrow} = 0 \\ \Rightarrow \left\{ n_{i\tau}, S_j^- \right\} = \left(\left\{ n_{i\tau}, S_j^+ \right\} \right)^\dagger = 0. \end{gathered}$$

■

When reordering each square bracket contribution in equation (D.4), one can note that terms such as

$$\left(S_1^+ S_2^+ - S_1^- S_2^- \right) (n_{3\uparrow} - n_{3\downarrow}) = \left(f_{1\uparrow}^\dagger f_{1\downarrow} f_{2\uparrow}^\dagger f_{2\downarrow} - f_{1\downarrow}^\dagger f_{1\uparrow} f_{2\downarrow}^\dagger f_{2\uparrow} \right),$$

corresponding to exchanges between sites with equal spin, are identically canceled for all possible permutations. Therefore, the operator E_{123} can finally be understood as

$$E_{123} = \frac{i}{4}\left\{\left[S_1^- S_3^+ - S_1^+ S_3^-\right](n_{2\uparrow} - n_{2\downarrow}) + \left[S_1^+ S_2^- - S_1^- S_2^+\right](n_{3\uparrow} - n_{3\downarrow}) + \right. \\ \left. + \left[S_2^+ S_3^- - S_2^- S_3^+\right](n_{1\uparrow} - n_{1\downarrow})\right\}. \tag{D.6}$$

Finally, considering the Abrikosov representation and the order $f^\dagger_{i\uparrow} f_{i\downarrow} f^\dagger_{j\downarrow} f_{j\uparrow} = -f^\dagger_{i\uparrow} f_{j\uparrow} f^\dagger_{j\downarrow} f_{i\downarrow}$ where all spin up operators are on the left side of the spin down operators, we can identify the chiral contribution of one triangle plaquette in the fermionic spinon language as

$$E_\chi^{NL} = \tfrac{i}{4}\left[f^\dagger_{2\uparrow} f_{3\uparrow} f^\dagger_{3\downarrow} f_{2\downarrow}(n_{1\downarrow} - n_{1\uparrow}) + f^\dagger_{3\uparrow} f_{2\uparrow} f^\dagger_{2\downarrow} f_{3\downarrow}(n_{1\uparrow} - n_{1\downarrow})\right] + \\ + \left[f^\dagger_{3\uparrow} f_{1\uparrow} f^\dagger_{1\downarrow} f_{3\downarrow}(n_{2\downarrow} - n_{2\uparrow}) + f^\dagger_{1\uparrow} f_{3\uparrow} f^\dagger_{3\downarrow} f_{1\downarrow}(n_{2\uparrow} - n_{2\downarrow})\right] + \\ + \left[f^\dagger_{1\uparrow} f_{2\uparrow} f^\dagger_{2\downarrow} f_{1\downarrow}(n_{3\downarrow} - n_{3\uparrow}) + f^\dagger_{2\uparrow} f_{1\uparrow} f^\dagger_{1\downarrow} f_{2\downarrow}(n_{3\uparrow} - n_{3\downarrow})\right]. \tag{D.7}$$

This equation states that the cyclical permutation in the chiral interaction is equivalent to taking two effective exchanges from the six possibilities in an elementary triangle. There are different and equivalent ways in the literature to express this interaction:

- From Motrunich *et al*, 2006,[141] the chiral interaction is understood as

  $$E_{123} = -\sin\left(\Phi_{123}^{\text{ext}}\right)\frac{i}{4}\left(P_{123} - \text{h.c.}\right), \tag{D.8}$$

  where Φ_{123}^{ext} is the gauge phase related to the cyclic permutation $P_{123} = t_{12}t_{23}t_{31}$ in each elementary up-pointing triangle. An analogous expression appears in Wen *et al*, 1989,[23] as [*]

  $$E_{123} = 2i\left(P_{123} - P_{132}\right). \tag{D.9}$$

  Using the property,[141]

  $$P_{123} = P_{12} + P_{23} + P_{31} - 1 - \text{h.c.}, \tag{D.10}$$

  and the Abrikosov representation, we arrive at

  $$E_{123} = \frac{i}{4}\left(P_{123} - P_{132}\right) = \frac{i}{4}\left[\left(P_{23} - P_{32}\right) + \left(P_{31} - P_{13}\right) + \left(P_{12} - P_{21}\right) - \text{h.c.}\right] \tag{D.11}$$

  which is equivalent to equation (D.7).

- Finally, one additional representation was recently introduced as[12, 27]

  $$E_{123} = \frac{i}{4}\left[\xi(1,2)\,\xi(2,3)\,\xi(3,1) - \xi(1,3)\,\xi(3,2)\,\xi(2,1)\right], \tag{D.12}$$

  with the notation difference of the link operators given by $\xi(l,m) = \sum_\tau f^\dagger_\tau(l)\, f_\tau(m)$ with $l, m = 1, 2, 3$ site indices.

---

[*] Here we must be careful with the extra factor of 2 since they define the Abrikosov representation as $\mathbf{S}_i = f^\dagger_{i\alpha}\boldsymbol{\sigma}_{\alpha\beta} f_{i\beta}$ instead of $\mathbf{S}_i = \frac{1}{2} f^\dagger_{i\alpha}\boldsymbol{\sigma}_{\alpha\beta} f_{i\beta}$.

In Figure 32 we consider the contributions for both clockwise (a) and counterclockwise permutations (b) - first and second terms in equation D.12, respectively for the configuration 001 from Table 5. After taking all possible virtual interactions, we arrive at two effective exchanges for any possible spin configuration in the triangle. These are represented in Table 5, alongside their connection with these cyclic permutations and our analytical derivation for the chiral energy in the spinon language from equation D.7.

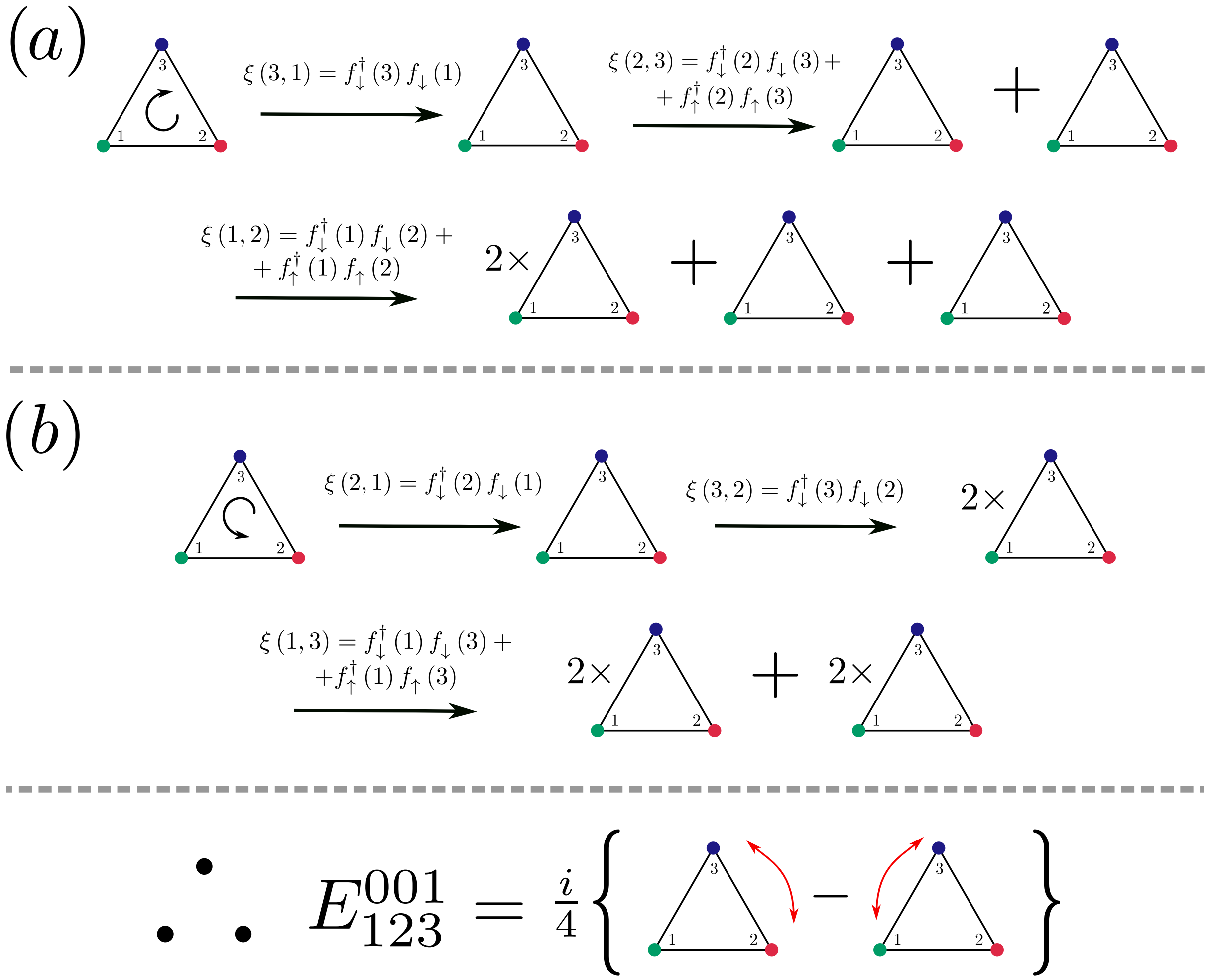
(a)
$\xi(3,1) = f^\dagger_\downarrow(3) f_\downarrow(1)$
$\xi(2,3) = f^\dagger_\downarrow(2) f_\downarrow(3) + f^\dagger_\uparrow(2) f_\uparrow(3)$
+
$\xi(1,2) = f^\dagger_\downarrow(1) f_\downarrow(2) + f^\dagger_\uparrow(1) f_\uparrow(2)$
2×
+
+
(b)
$\xi(2,1) = f^\dagger_\downarrow(2) f_\downarrow(1)$
$\xi(3,2) = f^\dagger_\downarrow(3) f_\downarrow(2)$
2×
$\xi(1,3) = f^\dagger_\downarrow(1) f_\downarrow(3) + f^\dagger_\uparrow(1) f_\uparrow(3)$
2×
+
2×
1
2
3
$\therefore E^{001}_{123} = \frac{i}{4}\{ \; - \; \}$

Figure 32 – Virtual exchanges for the clockwise (a) and counterclockwise permutations (b) in the specific spin configuration 001. The final contribution, given by the sum of each term in equation (D.12), can be seen in Table 5. The colors of the spins are arbitrary and serve only to guide the eye.
Source: By the author.